

UNIVERSITY OF MIAMI

OUTFLOW REPRESENTATION IN HYCOM

By

Xiaobiao Xu

A DISSERTATION

Submitted to the Faculty
of the University of Miami
in partial fulfillment of the requirements for
the degree of Doctor of Philosophy

Coral Gables, Florida

December 2006

UNIVERSITY OF MIAMI

A dissertation submitted in partial fulfillment of
the requirements for the degree of
Doctor of Philosophy

OUTFLOW REPRESENTATION IN HYCOM

Xiaobiao Xu

Approved:

.....
Dr. Eric P. Chassignet
Committee Chair and Professor of
Meteorology and Physical Oceanography

.....
Dr. William E. Johns
Professor of
Meteorology and Physical Oceanography

.....
Dr. Hartmut Peters
Research Associate Professor of
Meteorology and Physical Oceanography

.....
Dr. Steven G. Ullmann
Dean of the Graduate School

.....
Dr. Tamay M. Özgökmen
Associate Professor of
Meteorology and Physical Oceanography

.....
Dr. James F. Price
Senior Scientist
Woods Hole Oceanographic Institute

Abstract of a dissertation at the University of Miami.

Dissertation supervised by Professor Eric P. Chassignet.
No. of pages in text. (135)

In this dissertation work, the representation of dense water outflow in an oceanic general circulation model (OGCM) is investigated. The focus has been on the parameterization of the entrainment process, which is a key factor determining both the water properties and volume transports of the deep water mass formed by outflows. The study is carried out within the framework of numerical simulations with a HYbrid Coordinate Ocean Model (HYCOM).

First, building on the work of Turner (1986) and Hallberg (2000), an algebraic parameterization of the entrainment process in gravity currents has been derived for HYCOM. It casts the entrainment into layers as a function of the layer Richardson number Ri times the velocity difference across layers. In order to determine the Ri -dependant function, simulations of generic gravity currents over various bottom slope angle are conducted with HYCOM and compared to similar experiments with the high-resolution, three-dimensional, nonhydrostatic model Nek5000. A simple linear function is found to reproduce quantitatively the characteristic of the gravity current in Nek5000. The parameterization is also consistent with the fundamental theoretical and laboratory results from stably-stratified shear flows, in that the shear-induced turbulence grows (decays) in the regime of Ri less (larger) than $1/4$, respectively.

Second, in order to evaluate how well the entrainment parameterization can simulate realistic outflows, a high-resolution simulation of the Mediterranean outflow water (MOW)

is conducted and the results are compared to the observational data obtained from the 1988 Gulf of Cádiz Expedition. The comparison shows the simulation reproduces the observed Mediterranean outflow water in the Gulf quite well, including the evolution of temperature, salinity, and velocity profiles, the steering and spreading of the outflow plume as it descends along the continental slope, the transition of plume behavior from a bottom-trapped density current to a wall-bounced undercurrent, and most importantly, the localized entrainment immediately west of the strait where the outflow water experiences a significant modification in both volume transport and water properties.

The sensitivity of the performance of the entrainment parameterization to horizontal and vertical resolution is also investigated. The topography representation associated with a change in horizontal resolution plays an important role in outflow simulation. The entrainment becomes weaker as the horizontal resolution decreases. However, the simulated MOW equilibrates at intermediate depth with horizontal resolution of 0.08° to 0.32° and is consistent with observations. The vertical resolution has a more serious impact, and the parameterization does not work well with coarse vertical resolution.

Finally, a number of experiments aimed at climate variation scenarios are carried out and the results are used to evaluate the ‘marginal sea boundary condition’ (MSBC, Price and Yang, 1998), which is an alternative approach used to represent outflows for coarse resolution climate models at NCAR and GFDL. The study shows that, although MSBC does not resolve details of the outflow plume as do the regional HYCOM simulations, it reproduces comparable results in terms of the variation in product water of the Mediterranean outflow associated with changes in the source and ambient water properties.

Acknowledgements

I am thankful to my advisor, Eric P. Chassignet, for having given me the opportunity to work on this interesting project, for his very solid advices not only on the dissertation but also on the general scientific research, and for all the supports. This work is profited much from the members of my dissertation committee. I am grateful to Bill Johns for his wonderful class of “Large-scale ocean circulation: models and observations”, which inspired me to study the deep ocean at very beginning. Thanks to Jim Price for his always prompt response when I have questions and always very insight points of view about outflows. And special thanks to Tamay Özgökmen and Hartmut Peters, for their great effort in keeping me on the right track of the dissertation.

Through all phases of this work I was helped immensely by the HYCOM groups at RSMAS and at NRL, in particular, Drs. Zulema Garraffo, Mohamed Iskandarani, Ge Peng, George Halliwell, and Alan Wallcraft. The work is also greatly benefited by discussions with the CPT-GCE group (Climate process team on gravity current entrainment, <http://www.cpt-gce.org>). I thank Dr. Y. Chang for lots of cooperative work on comparison of HYCOM to the nonhydrostatic model and lots of help in MATLAB.

Many thanks to Linda Smith, who has helped me since my very early stage of learning HYCOM, who also is the first reader of my dissertation and gives me great help in correcting the grammar and improving the style of writing therein.

I extend my gratitude to all MPO staffs, professors, and students, and to all my friends at RSMAS, who provided a great environment both in personal and professional respects. This work would be impossible without the computer supports provided by Ashwanth Srinivasan and Daniel Voss. Thank you so much, Ashwanth and Dan. I would also like to thank my four wonderful officemates, John E. Brown, Tânia G. D. Casal, Benjamine Jaimes, and Marcello G. Magaldi. We had great time together.

Finally, I thank my wife Rong Liu, to whom this work is dedicated, and my parents Shenan Xu and Shenghua Li. Without them, I cannot be even close to this point.

Contents

List of Tables	viii
List of Figures	x
1 Introduction	1
2 Comparison of the K-profile and Turner’s parameterization	8
2.1 Vertical coordinates and diapycnal mixing in HYCOM	9
2.1.1 K-profile parameterization (KPP)	10
2.1.2 Turner parameterization (TP)	12
2.2 Numerical performance of diapycnal mixing in HYCOM	15
2.2.1 Constant layer diffusion experiment	16
2.2.2 Massless layer inflation experiment	17
2.3 Two-dimensional ‘dam-break’ experiments	19
2.4 Summary and discussion	27
3 Development of an entrainment parameterization using a high- order non- hydrostatic model	34
3.1 The nonhydrostatic model Nek5000	35

3.2	Experimental configuration	36
3.3	Results from the nonhydrostatic 3D model	37
3.4	HYCOM with linear parameterization functions	42
3.5	Detailed comparison between HYCOM with optimal $f(Ri)$ and Nek5000	52
3.6	Summary and discussion	62
4	Simulation of the Mediterranean outflow in the Gulf of Cádiz	64
4.1	Introduction	65
4.2	Observational data	66
4.3	Model configuration	68
4.4	Results	68
4.4.1	Exchange through the Strait of Gibraltar	68
4.4.2	Comparison of T/S profiles	71
4.4.3	Comparison of horizontal velocity profiles	73
4.4.4	Steering and spreading of the outflow plume	77
4.4.5	Descent and entrainment	83
4.5	Summary and discussion	89
5	The sensitivity to horizontal and vertical resolution	92
5.1	Experiments with decreasing horizontal resolution	93
5.2	Experiments with increasing horizontal resolution and step topography	97
5.3	Experiments with increasing horizontal resolution and interpolated topography	101
5.4	Sensitivity to vertical resolution	102
5.5	Summary and discussion	105

6	An evaluation of the marginal sea boundary condition	108
6.1	Experiment configurations	109
6.2	Results	113
6.2.1	Outflow source water change	113
6.2.2	Ambient ocean water change	116
6.3	Summary and discussion	120
7	Conclusions	122
	Bibliography	127

List of Tables

2.1	The reference isopycnals and initial layer set up of the ‘dam-break’ configuration.	21
2.2	The modified mixing parameterization in converging experiments.	26
3.1	Parameters of the Nek5000 nonhydrostatic model simulations.	36
3.2	Values of E_0 in experiment sets A, B, C, and D.	44
4.1	The reference densities $\hat{\sigma}_2$ (kg/m ³) used in the Mediterranean outflow experiment.	68
5.1	The geometry of the Strait of Gibraltar, the simulated volume and salinity transports (time mean \pm standard deviation) across the strait in 3 different configurations.	93
5.2	The same as Table 5.1 for experiments with increasing resolution and step topography	99
5.3	The same as Table 5.1 for experiments with increasing resolution and interpolated topography.	102

6.1	Some external parameters of the MSBC for the Mediterranean outflow: ϕ , W , and d_s are the latitude (in $^\circ$), width (in km), and sill depth (in m) of the Strait of Gibraltar. A , Q , and E-P are the area (in 10^6 km^2) of the Mediterranean Sea, heat flux (in W m^{-2} , negative indicates heat loss from the marginal sea), and evaporation minus precipitation (in m yr^{-1} , positive indicates excess evaporation). α is the slope of the continental slope. d_e is the depth (in m) on which entrainment takes place. “-” means the value is the same as in Price and Yang (1998).	112
6.2	The ratio of normalized variations of the outflow product water to that of the density contrast. Q_p , \bar{S}_p , \bar{T}_p , and \bar{D}_p are the volume transport, salinity, temperature, and equilibrium depth of the outflow product water.	120

List of Figures

2.1	The initial (Left) and the analytical time evolution (Right) of the temperature profile for constant layer diffusion experiment.	16
2.2	Results of constant layer diffusion experiment. Time evolution of (a) the vertically averaged pot. temperature; (b) the analytical results and simulated layer interface; (c) the evolutions of layer interface (lines) and $\theta(z)$ (color) in isopycnic coordinate; and (d) the evolutions of layer interface (lines) and $\theta(z)$ (color) in hybrid coordinate.	18
2.3	The same as Fig. 2.1 but for massless layer inflation experiment.	19
2.4	The same as Fig. 2.2 but for massless layer inflation experiment.	20
2.5	The same as Fig. 2.4d but with baroclinic time step of 360 sec (Left) and 36 sec (Right), respectively.	21
2.6	The vertical distribution of the pot. temperature before the dam break. Two water masses (θ of 5 and -1°C) are divided by a vertical front on top of the Gaussian topography.	22
2.7	The vertical distribution of pot. temperature 4 days after the ‘dam-break’ along zonal section in HYCOM using KPP (upper panel) and TP (lower panel).	23
2.8	The time evolution of volume percentage of the outflow water (layer 3 ~ 7) in the west half of domain. KPP (left panel) and TP (right panel).	24

2.9	The time evolution of Ri and κ at station near the slope in HYCOM using KPP (left panels) and TP (right panels).	25
2.10	Result of EXPT A. The vertical distribution of pot. temperature in HYCOM using constrained TP (left panels) and KPP (right panels). From top to bottom, κ_{max} used are 0.01, 0.05 and $0.25 \text{ m}^2 \text{ s}^{-1}$ respectively.	28
2.11	Result of EXPT A. The percentage of outflow water in the west half of the domain as function of time in HYCOM simulations using constrained TP (left panels) and KPP (right panels). From top to bottom, κ_{max} used are 0.01, 0.05 and $0.25 \text{ m}^2 \text{ s}^{-1}$ respectively.	29
2.12	Result of EXPT B. The vertical distribution of pot. temperature in HYCOM using TP (left panels) and modified KPP (right panels). From top to bottom, factor C used are 0.1, 0.2 and 0.5 respectively.	30
2.13	Result of EXPT B. The percentage of outflow water in the west half of the domain as function of time in HYCOM simulations using TP (left panels) and modified KPP (right panels). From top to bottom, factor C used are 0.1, 0.2 and 0.5, respectively.	31
3.1	The initial distribution of the salinity anomaly and velocity profile in the relaxation zone ($x = -1$ to $x = 0$ km) in the HYCOM configuration. $X_0 = 1.2$ km is marked as a ‘ Δ ’.	37
3.2	Snapshots of the salinity anomaly distribution in Nek5000 experiments with 4 different slope angles when the gravity current reaches the end of the domain.	38
3.3	(a) Propagation distance ℓ in m and (b) propagation speed U_F in m s^{-1} of the gravity currents as a function of time in Nek5000 experiments with four slope angles.	40

3.4	(a) Entrainment parameter \mathcal{E} and (b) salt flux F_S in $\text{kg m}^{-2} \text{s}^{-1}$ as a function of the gravity current length ℓ in Nek5000 experiments with four different bottom slopes. The dotted lines in (a) mark the values of \mathcal{E} corresponding to $\theta = 1^\circ$ and $\theta = 4^\circ$ in the formula $\mathcal{E} = 10^{-3} \times (5 + \theta)$ of Turner (1986).	43
3.5	Results from Exp. A, $Ri_c = 0.75$. (a) Entrainment rate E as linear functions of Ri in experiments A1 to A6. The dash line is Turner's (1986) formula (2.9). The time-averaged Ri of layer 3 is marked as "o". (b) Entrainment parameter $\mathcal{E}(\ell)$ from Nek5000 and HYCOM. The shaded area represents a $\pm 20\%$ variance around Nek5000 results. (c) Salt flux $F_S(\ell)$ in $\text{kg m}^{-2} \text{s}^{-1}$ from HYCOM in comparison to Nek5000. (d) Richardson number $Ri(t)$ of layer 3 at $x = X_0$ from HYCOM experiments, with the dash line marks Ri_c	47
3.6	The same as in Figure 3.5 but for Exp. B, $Ri_c = 0.50$	48
3.7	The same as in Figure 3.5 but for Exp. C, $Ri_c = 0.35$	49
3.8	The same as in Figure 3.5 but for Exp. D, $Ri_c = 0.25$	51
3.9	Entrainment rate $E \equiv w_E/\Delta U$ as function of Richardson number Ri . The solid blue, green and red lines are linear function Eq. (3.11) with parameters $E_0 = 0.20$ and $Ri_c = 0.20, 0.25$ and 0.30 ; the dash and dot black lines are the original TP and parameterization function of Chang et al. (2005) with $C_A = 0.15$, respectively.	52
3.10	Salinity snapshots when the gravity currents plume approaches the lower end of domain; HYCOM using P2 (left) and Nek5000 (right) with different bottom slopes ($1 \sim 4^\circ$).	54

3.11	Entrainment parameter $\mathcal{E}(\ell)$ from Nek5000 and HYCOM experiments with different bottom slopes. The Nek5000 results appears with shaded $\pm 20\%$ variance; five entrainment schemes in HYCOM are Turner (1986), Chang et al. (2005), P1, P2, and P3, respectively.	55
3.12	Salt flux $F_S(\ell)$ from Nek5000 and HYCOM experiments with different bottom slopes.	56
3.13	Richardson numbers $Ri(t)$ of layer 3 at $x = X_0$ from HYCOM experiments with different bottom slopes. The dash line marks $Ri = 0.25$	58
3.14	Richardson numbers $Ri(t)$ at different depths at $x = X_0$ from Nek5000 experiment with $\theta = 1^\circ$. The dash line marks $Ri = 0.25$	59
3.15	Zonal velocity profiles at station $x = 3$ km (left panels) and $x = 5$ km (right panels) from Nek5000 and HYCOM with linear entrainment scheme P2. The black line is the mean profile from Nek5000 with shading area representing the time variation; five different C_D s are tested in HYCOM, with center of each layer marked as “o”. The upper and lower panels are 1° and 4° slope configuration, respectively.	60
3.16	The plume propagation distance ℓ vs. time from Nek5000 and HYCOM experiments with different bottom slopes. HYCOM is run with the linear entrainment scheme P2 and five bottom drag coefficients C_D	61
4.1	The locations of CTD (upper) and XCP (below) stations during the 1988 Gulf of Cádiz Expedition.	69

4.2	The simulated vertical profiles of salinity (left panel) and horizontal velocity (right panel) in the Strait of Gibraltar near the Carminal Sill (5.72°W, 39.1°N). The thick dash lines are the initial profiles; the thin gray lines are simulated profiles in every 3 days; and the thick solid lines represent the time-averaged profile. The observed velocity profiles are reproduced from Fig. 5.7.5 of Candela (2001)	70
4.3	The simulated volume transport (in Sv) and salinity transport (in $10^3 \text{ m}^3 \text{ s}^{-1}$) of the Mediterranean outflow through the Strait of Gibraltar.	71
4.4	Comparison of T/S profiles of CTD sections between observation (left panels) and model (right panels). From top to bottom are sections I, A, B, and C. .	74
4.5	Comparison of T/S diagrams for all CTD sections between observation (left panel) and model (right panel).	77
4.6	Comparison of U/V profiles of XCP stations between observation (left panels) and model (right panels). From top to bottom are sections I, A, B, and C. .	78
4.7	The horizontal structure of the simulated (upper panel) and observed (lower panel) MOW plume in the Gulf of Cádiz. The contour lines are 10 m, 50 m, 100 m, 200 m and 400 m time mean thickness; the arrows are the time and vertically averaged plume velocity.	81
4.8	The mean horizontal velocity of the upper and lower half of the MOW plume, represented by thin and thick arrows, respectively. The contours show the isobaths increasing from 100 to 1000 m with interval of 100 m.	83
4.9	The evolution of salinities as a function of longitude. The solid lines are from simulation while the dash dot lines are from the observations. The color red, green, blue, and magenta represent S_{max} , S_{mean} , \bar{S} , and S_{NA} respectively. .	85

4.10	The evolution of volume transports as a function of longitude. The black line is the 3-month mean total transport, with the gray dots present the transport in every 3 days. The black dots are the volume transport through sections A to F, from the Table 1 of Baringer and Price (1997a). The red and blue lines are Q_{Med} and Q_{NA} , from Eq. 4.5.	87
4.11	The entrainment velocity w_E (in mm s^{-1}) as a function of longitude estimated from simulation (lines) and observations (dot lines). The observations estimates are taken from Baringer and Price (1997b). The color red and blue represent the velocity diagnosed from volume and salt flux, respectively. . .	88
4.12	Volume transport of MOW (in Sv) in classes of depth (in bins of 20 m) and of potential density (in bins of 0.01kg m^{-3}) through sections A to F. The upper two panels are observations from Fig. 14 of Baringer and Price (1997a) and the lower two panels are from the simulation.	90
5.1	Time evolution of the simulated volume transport (lines, in Sv) and salinity transport (circles, in $10^3 \text{m}^3 \text{s}^{-1}$) through the Strait of Gibraltar. Values are negative because the transport are westward. The red, green, and blue color represent horizontal resolution of 0.32° , 0.16° and 0.08° , respectively. . . .	94
5.2	Snapshots of the salinity distribution at 9°W and 8°W . From top to bottom are simulations with horizontal resolutions of 0.08° , 0.16° , and 0.32° , respectively.	95
5.3	The same as Fig. 4.7 but for configurations with horizontal resolutions of 0.16° (upper panel) and 0.32° (lower panel), respectively.	96

5.4	The width W , thickness \bar{h} , depth \bar{D} , velocity \bar{u} , volume transport Q_{out} , and salinity \bar{S} of the simulated Mediterranean outflow plume as a function of longitude. The color red, green and blue represent the configuration with horizontal resolution of 0.32° , 0.16° , and 0.08° , respectively.	98
5.5	The same as Fig. 5.1 but for experiments with increasing horizontal resolution and step topography.	99
5.6	Snapshots of the salinity distribution at 9°W and 8.6°W . From top to bottom are simulations with horizontal resolution of 0.08° , 0.16° , and 0.32° , respectively.	100
5.7	The same as Fig. 5.1 but for experiments with increasing horizontal resolution and interpolated topography.	101
5.8	The same as Fig. 5.6 but for experiments with increasing horizontal resolutions and interpolated topography.	103
5.9	The same as Fig. 5.4 But for experiments with increasing horizontal resolutions and interpolated topography.	104
5.10	Number and distribution of the target densities ($\hat{\sigma}_2$) between 36.62 and 37.48 kg m^{-3} in 4 configurations. 13-layer is the reference experiment. . . .	105
5.11	Snapshots of the salinity distribution at sections 9° (left panels) and 8°W (right panels) with different vertical resolutions. From top to bottom are experiments with 15, 13, 7, and 4 layers between the outflow source and product water.	106
6.1	Typical temperature, salinity, and density profiles in the Mediterranean Sea (solid lines) and in the Gulf of Cádiz (dash lines). The $\Delta\rho = 2.0 \text{ kg m}^{-3}$ at 250 m marks the reference density contrast between two basins.	110

6.2	(a) the temperature, salinity, and density profiles in the Mediterranean Sea in the experiments with outflow source water change; (b) the temperature, salinity, and density profiles in the Gulf of Cádiz in the experiments with ambient ocean water change.	111
6.3	A schematic of the two components of the marginal sea boundary condition. One (a model of marginal sea-deep ocean exchange) converts the surface inflow water into an outflow source water, and the other (a model of a rotating, entraining gravity current) transforms the outflow source water into final outflow water which feeds back into deep ocean.	112
6.4	Snapshots of salinity distribution at 8.6°W. Panels (a) to (e) are the experiments in which the density of outflow source water is shifted by -20%, -10%, 0%, +10%, and +20% of the $\Delta\rho$, respectively.	113
6.5	Results of HYCOM experiments with outflow source water change. The evolution of mean volume transport, salinity, temperature, and depth of the Mediterranean outflow in the Gulf of Cádiz.	115
6.6	MSBC versus HYCOM with outflow source water change. Lines are from MSBC and circles are the HYCOM results. Error bars represent the standard deviation for transport, salinity and temperature, and the upper and lower interface of outflow plume for depth. The red color represents the outflow source water and blue the product water.	116
6.7	The same as Fig. 6.4 but for experiments with ambient ocean water change.	117
6.8	The Same as Fig. 6.5 but for experiments with ambient ocean water change.	118

6.9 MSBC versus HYCOM with ambient ocean water change. Lines are from MSBC and circles are the HYCOM results; Error bars represent the standard deviation for transport, salinity and temperature, and the thickness of outflow plume for depth. The red and blue color represent the outflow source water and product water. 119

Chapter 1

Introduction

The ocean stores a huge amount of heat and greenhouse gases, and moves them horizontally over large distances at rates comparable to the atmosphere. In order to improve our understanding of the ocean's role in climate and climate change, it is crucial to know how climate signals are transmitted from the sea surface, where the ocean is in contact with the atmosphere, into the deep ocean, and how these signals are redistributed through global circulation.

One effective mechanism for exchanging fluid and fluid properties between the sea surface and the deep ocean is convection. Open-ocean deep convection (Marshall and Schott, 1999), however, is largely inhibited by the strong vertical density gradients of the thermocline over most of the ocean, except for a few localized regions where stratification is relatively weak and is subject to intense buoyancy loss to the atmosphere on a time scale of months. These convectively formed water masses finally feed into the thermohaline circulation, transmitting climate signals from the sea surface into the global deep ocean. One example of this path of transmission is the evolution of the Labrador Sea Water (LSW; Lazier, 1973; Talley and McCartney, 1982; The Lab Sea Group, 1998), which has received much attention in the last

several decades. The LSW is formed in the Labrador Sea and probably also in the Irminger Sea (Pickart et al., 2003a,b) and spreads into the rest of North Atlantic Ocean in several directions (Talley and McCartney, 1982; Sy et al., 1997; Rhein et al., 2002). Temporal changes in the production rate and properties of LSW have been detected, years later, in water property changes at depth in the subtropical region (e.g., Curry et al., 1998; Molinari et al., 1998).

Most deep and intermediate water masses of the world ocean, however, are released into the large-scale circulation from high-latitude and marginal seas in the form of outflows. Examples of outflows include the Mediterranean (Baringer and Price, 1997a,b), the Denmark Strait (Girton et al., 2001; Girton and Sanford, 2003), the Faroe Bank Channel (Price, 2004), the Red Sea (Peters et al., 2005; Peters and Johns, 2005), and the Antarctic slope plumes on the margin of the Antarctic Ocean (Gordon et al., 2004). These outflows carry the dense water masses resulting from strong air-sea interaction into the deep ocean and gradually help to set up the water properties and circulation there. The outflow water through the Denmark Strait and Faroe Bank Channel, for example, directly feeds the major part of the North Atlantic Deep Water (NADW), which is the lower branch of the meridional overturning circulation (MOC) in the North Atlantic Ocean. The Mediterranean outflow water (MOW), on the other hand, transports heat and salt into the mid-depths of the North Atlantic subtropics. Furthermore, the downward outflow mass fluxes and the spreading of outflow water in the deep ocean require compensating upwelling elsewhere and a return flow in the upper ocean, thus completing an overturning cell.

While each outflow case is unique in its details, all have three physical components in common: the air-sea exchange, the marginal sea-open ocean exchange, and the descent and entrainment. As summarized by Price and Baringer (1994), the air-sea exchange and

the marginal sea-open ocean exchange combine to determine the heat and salt budget of the marginal sea and thus the T/S properties of the source waters of the outflows. Because of its high density, the outflow water must descend the continental shelf and slope before reaching the open ocean. As the outflow descends into the open ocean, it entrains a substantial volume of the overlying ambient water (Lee and Ellett, 1965; Smith, 1975), typically doubling the outflow volume transport. Consequently, the water properties of the ‘product water’ mass that finally settles into the open ocean may have quite different characteristics from those of the source waters that first flowed out from the marginal seas. Therefore, the outflow entrainment ultimately determines the net volume transports, water properties, and final depth of the new product water entering the deep circulation. An interesting fact highlighting the importance of entrainment is that the density ordering of the source water of the four major outflows (the Antarctic slope plume and the outflows through Denmark Strait, Faroe Bank Channel, and the Strait of Gibraltar) is the reverse of the density ordering of the corresponding product water found in the open ocean (Price and Baringer, 1994).

The numerical study of outflows was initiated by the stream-tube model of Smith (1975). This model, as well as refined versions (e.g., Killworth, 1977; Price and Baringer, 1994), simplified the bottom flow as a single layer of dense water underlying a stagnant ambient environment. Temperature, salinity, and momentum equations are averaged over the layer cross section. These one-dimensional models captured the most fundamental dynamics, i.e., the density contrast between outflow and ambient water, the bottom topography, the earth rotation parameter f , the bottom stress, and entrainment, and thus were able to reproduce quite successfully the changes of bulk properties along the outflow path. But, clearly, they omit several important aspects of real outflows (i.e., horizontal/vertical structure,

moving ambient water, and non-steady properties). Using a two-dimensional transient reduced gravity plume model, which resolves the horizontal structure and is able to simulate the plume splitting and merging, Jungclaus and Backhaus (1994) demonstrated that the presence of topography can cause complicated cross-stream variations in the Denmark Strait outflow. Since approximately a decade ago, outflow simulations using three-dimensional primitive equation models have been published (i.e., Gawarkiewicz and Chapman, 1995; Hallberg, 2000; Jiang and Garwood, 1995; Jungclaus and Mellor, 2000; Käse and Oschlies, 2000; Käse et al., 2003; Krauss and Käse, 1998; Papadakis et al., 2003; Spall and Price, 1998). Most of these studies use idealized configurations and focus on the explanation of the mesoscale variability associated with outflow plumes.

A proper representation of outflows from marginal seas in oceanic general circulation models (OGCMs) is a prerequisite to understanding their large-scale impact. This representation, however, continues to be a challenge. One difficulty is the high grid resolution necessary to resolve the small topographic features associated with outflows. Horizontally, a grid spacing of $1/10^\circ$ or less is required to resolve the Strait of Gibraltar. Though most regional and some basin scale simulations are now able to achieve this resolution, long-term simulations, especially climate-related studies, typically use grid sizes of an order of the magnitude larger. In the vertical, the down-slope currents of an outflow present another challenge to the model formulation. Except with a very high number of levels, z -coordinate models cannot provide sufficient vertical resolution as outflow plumes descend. Terrain-following models, by applying some logarithmic σ levels within the bottom layer, can concentrate resolution near the bottom boundaries and hence resolve outflow processes. However, these models have difficulty to accurately represent the horizontal pressure gradient (e.g., Janjić, 1977; Mesinger, 1982; Haney, 1991; Beckmann and Haidvogel, 1993; Mellor

et al., 1994, 1998; Chu and Fan, 1997; Song and Wright, 1998a,b,c). In isopycnic coordinate or hybrid (primarily isopycnic) models, the vertical resolution naturally migrates with the density front atop the gravity current.

Another challenge in modeling outflow is to accurately describe the strong diapycnal mixing ('entrainment') that takes place between the dense outflow plume and the light ambient water above. Turbulent mixing is a sub-grid-scale (SGS) process in OGCMs that must be parameterized. The most common method of parameterization in vertical is via eddy diffusion in the form of spatial Laplacian, with eddy diffusivity as the free parameter. Depending on how the eddy diffusivity is determined, various parameterizations have been proposed and implemented in different models. Z-coordinate models, for example, usually use first order closure schemes like Pacanowski and Philander (1981), or more recently the K-profile parameterization (KPP; Large et al., 1994, 1997; Large, 1998). In these schemes, the eddy diffusivity in the interior is prescribed as a function of the gradient Richardson number, which is calculated using model's prognostic variables. Terrain-following models, on the other hand, have tended to use second order closure schemes (e.g., Mellor and Yamada, 1982). However, a difficulty with fixed-coordinated models is that they are prone to have excessive numerical diapycnal mixing (DYNAMO Group, 1997; Willebrand et al., 2001). It is therefore not straightforward to distinguish between the impact of the explicit mixing prescribed by an entrainment parameterization and the effect of the spurious mixing induced by numerics (Griffies et al., 2000).

By design, there is no numerically-induced diapycnal mixing in isopycnic models. In the absence of an explicit mixing parameterization due to entrainment, the isopycnic model presents the opposite scenario to that of z-coordinate models, i.e., no mixing so that the outflow water mass is not changed. Hallberg (2000) developed an implicit scheme that can

explicitly prescribe an empirical entrainment in an isopycnic model. The entrainment is based on the laboratory experiments of Ellison and Turner (1959) and subsequent analysis by Turner (1986), and thus the parameterization will be hereafter referred to the Turner Parameterization (TP). Papadakis et al. (2003) have shown that the isopycnic model with this scheme can simulate the basic features of the Mediterranean water plume flowing out of the Strait of Gibraltar. However, the same scheme implemented in a basin-scale North Atlantic simulation led to a Mediterranean outflow water that settled at a shallower depth than found in observations, indicating overly strong entrainment. Similar simulations with KPP instead of TP presented a very different result: the outflow water in simulation with KPP descends substantially deeper than in the observations, suggesting that the interior mixing prescribed by KPP is too weak.

The aim of this present work is to investigate the representation of outflows in the HYbrid Coordinate Ocean Model (HYCOM). Focus is on the parameterization of the entrainment process, which is crucial in determining the volume transport and water properties of the outflow product water. Various diapycnal mixing parameterizations have been implemented in HYCOM, including KPP. In Chapter 2, we compare the performance of TP and KPP in representing the outflow entrainment, in order to document the differences observed in the above mentioned basin-scale North Atlantic simulations, and to provide some guidelines for further parameterization development. An algebraic parameterization of entrainment is then developed in Chapter 3. This is achieved by comparing high-resolution HYCOM simulations to similarly configured high resolution, nonhydrostatic experiments. These simulations, as shown by Özgökmen and Chassignet (2002) and Özgökmen et al. (2004b,a), are able to resolve the turbulent mixing associated with gravity current, and to reproduce the major plume features as observed in laboratory experiments. Ultimately, the usefulness of a

parameterization can only be evaluated by comparing the modeled outflow to observations. The parameterization developed in Chapter 3 is evaluated in Chapter 4, by comparing the simulated Mediterranean outflow from a regional configuration to the field data obtained from the 1988 Gulf of Cádiz Expedition. However, the model's ability in simulating an outflow depends not only on the entrainment parameterization but also on the horizontal and vertical grid spacing used to resolve the outflow plume. The model will resolve the density gradient, the velocity shear, and thus the Richardson number differently, depending on the chosen horizontal and vertical resolutions. The sensitivity of the entrainment parameterization to resolution is therefore investigated in Chapter 5. Finally, for climate models, the lack of horizontal resolution is the biggest challenge in outflow representation. An alternative approach in representing outflow to that of an explicit representation is the marginal sea boundary condition (Price and Yang, 1998), which compresses the entire outflow process of water mass transformation into a sidewall boundary condition. The regional simulations of the Mediterranean outflow provide an ideal setting for evaluating how well this approach works, and such an assessment is presented in Chapter 6. The principal conclusions of this work are summarized and discussed in Chapter 7.

Chapter 2

Comparison of the K-profile and Turner's parameterization

The aim of this chapter is to compare the physics and implementation of two existing diapycnal mixing parameterizations in HYCOM, and to compare their performance in representing the entrainment process in outflows. These two parameterizations, the K-profile parameterization (hereafter KPP; Large et al., 1994, 1997; Large, 1998) and the Turner parameterization (hereafter TP; Turner, 1986; Hallberg, 2000), prescribe the diapycnal mixing in the $1/12^\circ$ North Atlantic HYCOM and MICOM simulations, respectively. Therefore, the comparison should help to understand the different solutions of the Mediterranean outflow in these two simulations, and to provide some guidelines for developing a new parameterization. KPP is derived from a wide range of oceanic observations and from a series of large eddy simulations (LES) of the equatorial upper ocean, while TP is based primarily on small-scale laboratory measurements of entraining gravity currents. Both schemes describe the mixing due to shear instability as a function of the Richardson number.

2.1 Vertical coordinates and diapycnal mixing in HYCOM

Motivated by the results of model comparison exercises performed in Europe and in the United States showing that no single vertical coordinate (i.e., z , isopycnic, or the terrain-following σ) can by itself be optimal everywhere in the ocean (DYNAMO Group, 1997; Willebrand et al., 2001; Chassignet et al., 2000), the HYbrid Coordinate Ocean Model (HYCOM, Bleck, 2002; Chassignet et al., 2003; Halliwell, 2004, detailed documentation available online at <http://www.hycom.org>) has been developed in University of Miami and at the Naval Research Laboratory (NRL). The implementation of a generalized coordinate in HYCOM follows the theoretical foundation set forth in Bleck and Boudra (1981) and Bleck and Benjamin (1993), that is, the model assigns to each grid point a reference or ‘target’ isopycnal, and continually tries to move individual grid points that have differed from their reference level back toward that level, until one of the following three states is reached: 1) a specified z/σ -layer thickness in the upper ocean layer or shallow area, 2) a specified minimum thickness in the ocean interior, or 3) zero thickness at the bottom. By this method, the vertical grid point is geometrically constrained to remain at fixed depth while being allowed to join and follow the reference isopycnal in the adjacent area.

The default vertical coordinate in HYCOM is isopycnic in the open stratified ocean, smoothly reverting to σ in shallow coastal regions and to z in the surface mixed layer and unstratified seas. It therefore combines the advantages of different types of coordinates in optimally simulating coastal and open-ocean circulation features. HYCOM is a generalized-coordinate mass-conserving ocean numerical model, and can therefore be configured for and integrated with only one type of coordinates. In ‘pure’ isopycnic coordinates, for example, each layer has the same potential density as the reference, and is allowed to fuse or become massless. This is essentially identical to the Miami Isopycnic Coordinate

Ocean Model (MICOM, Bleck, 1978; Bleck and Smith, 1990; Bleck et al., 1992).

The choice of vertical coordinate affects the complexity and the approach to implementing diapycnal mixing, which is a key component of any oceanic general circulation model (OGCM). Physically, diapycnal mixing redistributes the water properties such as the velocity \mathbf{u} , temperature T , salinity S , and passive tracers in a water column. Numerically the mixing is achieved by solving a set of vertical diffusion equations. This approach modifies the density profile $\sigma(z)$ via T/S changes and the equation of state, following which a ‘regridding’ process is necessary for HYCOM to restore the isopycnic condition. However, the approach of changing density does not work when HYCOM is configured with isopycnic coordinates only, in which the redistribution of $\sigma(z)$ is equivalent to a change of the layer thickness h of a specific isopycnal. Therefore, an alternative approach to change T and S is to change the layer thickness, while other properties are updated according to the thickness change. In other words, the diapycnal mixing in HYCOM can be implemented either by changing density or by changing thickness. Because these changes are implemented in hybrid and isopycnic coordinates, the approaches are termed ‘hybrid mode’ and ‘isopycnic mode’, respectively.

2.1.1 K-profile parameterization (KPP)

The implementation of KPP mixing follows the approach of changing density at a specific depth. It solves the vertical diffusion equations of momentum, temperature, and salinity:

$$\frac{\partial[\theta, S, \mathbf{u}]}{\partial t} = -\frac{\partial}{\partial z} \left(-K_{[\theta, S, m]} \frac{\partial[\theta, S, \mathbf{u}]}{\partial z} \right), \quad (2.1)$$

in which $K_{[\theta, S, m]}$ are the vertical temperature, salinity diffusivity, and viscosity. KPP prescribes the mixing coefficients (or K) from surface to bottom, smoothly matching large

values in the surface boundary layer to small values in the interior of the ocean. It has been widely used in OGCMs because of its various advantages. It works on a relatively coarse and unevenly spaced vertical grid; it parameterizes a fairly wide range of physical processes. In the ocean interior, the contributions of the background internal wave breaking, resolved shear instability, and double diffusion are parameterized. In the surface boundary layer, the influence of wind-driven mixing, surface buoyancy fluxes, and convective instability are parameterized. It also emphasizes the unique physics of the boundary layer by parameterizing the influence of nonlocal mixing of T and S, which permits the development of counter-gradient fluxes.

Relevant to the outflow entrainment process, the contribution of shear instability in KPP is parameterized by

$$K = K_{max} \left[1 - \min(1, Ri/Ri_c)^2 \right]^3 . \quad (2.2)$$

The shear Richardson number Ri in Eq. 2.2 is defined as

$$Ri = N^2 \left[\left(\frac{\partial u}{\partial z} \right)^2 + \left(\frac{\partial v}{\partial z} \right)^2 \right]^{-1} , \quad (2.3)$$

where the numerator and the denominator are the square of buoyancy frequency and vertical shear, respectively. K increases with decreasing Ri to account for the mixing induced by high vertical shear and/or weaker stratification. At the limit of $Ri = 0$, mixing takes place as in a homogeneous (unstratified) fluid. This concept is taken from Pacanowski and Philander (1981), but the shape of the mixing curve in KPP was adjusted to show better agreement with observational data from equatorial mixing by Gregg et al. (1985) and Peters et al. (1988) for the regime of $0.3 < Ri < 0.7$. There are two constants in Eq. 2.2, the maximum

diffusivity $K_{max} = 5.0 \times 10^{-3} \text{ m}^2 \text{ s}^{-1}$, and the cut-off Richardson number $Ri_c = 0.7$. The values are derived from large eddy simulations (LES) of the upper tropical ocean (Wang et al., 1996, 1998; Large and Gent, 1999). KPP is not valid universally since it does not conform to Buckingham’s Pi-theorem (e.g., Kundu, 1990), which states that constants in a physical law should be dimensionless. Diffusivity values significantly larger than the above K_{max} have indeed been observed in the equatorial Pacific Ocean (e.g., Peters et al., 1988).

After solving Eq. 2.1, the model calls the grid generator (subroutine ‘hybgen’), which moves the layer interface vertically to restore the isopycnic condition. For more details of the theory and implementation of this ‘re-grid’ algorithm, the reader is referred to Appendix C of Bleck (2002).

2.1.2 Turner parameterization (TP)

The implementation of TP follows the approach of changing the thickness of specific isopycnic layer. Combining the continuity equation and density equation:

$$\frac{1}{\rho} \frac{d\rho}{dt} + \nabla_3 \cdot \mathbf{u}_3 = 0; \quad \dot{\rho} = \nabla \cdot (\kappa \nabla \rho), \quad (2.4)$$

we get:

$$\frac{\partial}{\partial t} \left(\frac{\partial p}{\partial \rho} \right) + \nabla_\rho \cdot \left(\frac{\partial p}{\partial \rho} \mathbf{u} \right) = - \frac{\partial}{\partial \rho} \left(\frac{\partial p}{\partial \rho} \dot{\rho} \right) \approx - \frac{\partial}{\partial \rho} \left[\frac{\partial p}{\partial \rho} \frac{\partial}{\partial z} \left(\kappa \frac{\partial \rho}{\partial z} \right) \right]. \quad (2.5)$$

The approximations are that only diapycnal diffusion alters the density of a fluid parcel and that the slope of isopycnals is sufficiently small so that the total density gradient is well approximated by the vertical gradient alone. Integrating Eq. 2.5 over layer k , we obtain:

$$\frac{\partial h_k}{\partial t} = \frac{\partial}{\partial \rho} \left(\kappa \frac{\partial \rho}{\partial z} \right) \Big|_{k+1/2} - \frac{\partial}{\partial \rho} \left(\kappa \frac{\partial \rho}{\partial z} \right) \Big|_{k-1/2}, \quad (2.6)$$

in which h_k is the layer thickness. Defining a layer buoyancy flux F_k and thickness loss due to fluxes from the neighboring layers G_k :

$$F_k = \frac{\kappa_k \Delta \rho_k}{h_k}, \quad G_k = \frac{F_{k-1/2}}{\Delta \rho_{k-1/2}} + \frac{F_{k+1/2}}{\Delta \rho_{k+1/2}}, \quad (2.7)$$

Eq. 2.6 can be rewritten as:

$$\frac{\partial h_k}{\partial t} = \frac{2\gamma_k}{\Delta \rho_k} F_k - G_k; \quad \gamma_k = \frac{1}{2} \left(\frac{\Delta \rho_k}{\Delta \rho_{k-1/2}} + \frac{\Delta \rho_k}{\Delta \rho_{k+1/2}} \right). \quad (2.8)$$

γ_k equals one when the isopycnals are evenly discretized. The challenge of solving Eq. 2.8 lies in its nonlinearity and in the possibility of zero thickness and high diapycnal diffusivity. An iterative implicit scheme was introduced by Hallberg (2000) to solve this problem.

Diapycnal mixing transfers momentum, energy (i.e., heat), and tracers (i.e., salt, oxygen, etc.) across the layer interface. This transfer in the ocean interior physically is caused by buoyancy fluxes due to turbulent mixing processes. Similar to KPP, the mixing due to background internal wave breaking is prescribed by a constant diffusivity coefficient $\kappa = 0.1 \times 10^{-4} \text{ m}^2 \text{ s}^{-1}$ in Eq. 2.7. Describing the mixing contributed by shear instability is different from KPP (Eq. 2.2). A concept of net entrainment w_E is introduced to replace the left hand side of Eq. 2.8. The parameterization of w_E is based on laboratory measurements of gravity current by Ellison and Turner (1959) and on consequent analysis by Turner (1986), in which w_E is parameterized as:

$$w_E = \begin{cases} \Delta U \frac{0.08 - 0.1 Ri_B}{1.0 + 5 Ri_B} & \text{if } 0 < Ri_B < 0.8 \\ 0 & \text{if } Ri_B \geq 0.8. \end{cases} \quad (2.9)$$

The bulk Richardson number Ri_B in Eq. 2.9 is defined as:

$$Ri_B = \frac{\Delta\rho g h}{\rho\Delta U^2} \quad (2.10)$$

where h is the thickness of the gravity current plume, ΔU , and $\Delta\rho$ are the velocity and density difference between the gravity current and environment water. One may question how well these small scale laboratory results can represent the real ocean. Price and Baringer (1994) were, however, able to successfully predict the water property change in four observed outflow cases, using Eq. (2.9) in a one-dimensional stream tube model: the Mediterranean outflow, the Denmark Strait and Faroe Bank Channel outflow from the Nordic Seas, and the Filchner ice shelf outflow into the Weddell Sea.

The entrainment modifies the water properties throughout the descending outflow plume. In 3-D isopycnic coordinate models, multiple layers are needed to properly represent the gravity current. Hallberg (2000) therefore defined a layer Richardson number Ri_k (his Eq. 5.3):

$$Ri_k = \frac{\Delta\rho_k g h_k}{\rho_k\Delta U_k^2}, \quad (2.11)$$

in which

$$\frac{\Delta\rho_k}{\Delta U_k^2} = 2 \left(\frac{|\mathbf{u}_k - \mathbf{u}_{k-1}|^2}{\rho_k - \rho_{k-1}} + \frac{|\mathbf{u}_k - \mathbf{u}_{k+1}|^2}{\rho_k - \rho_{k+1}} \right)^{-1}. \quad (2.12)$$

Here, h , ρ and \mathbf{u} represent the layer thickness, density, and horizontal velocity, and the subscripts are layer indexes. Hallberg (2000) then implemented Eq. (2.9) in each layer using the layer Richardson number. This raises an issue as to whether the local layer Ris are able to represent the bulk Ri_B .

2.2 Numerical performance of diapycnal mixing in HYCOM

Since KPP is implemented via changing the density in hybrid coordinate while TP is implemented via changing the thickness in pure isopycnic coordinate, it is important to examine the numerical performance of these two approaches to diapycnal mixing. That is, how does the mixing compare given the same parameterization?

Two one-dimensional (1D) diffusion experiments are designed to investigate this. The advantage of using a 1D diffusion configuration is that it has an analytical solution. Assume an isolated water column with initial vertical profile of potential temperature $\theta(z)$

$$\frac{d\theta}{dt} = \kappa \frac{\partial^2 \theta}{\partial z^2}; \quad \frac{\partial \theta}{\partial z} = 0; \quad \theta(z, 0) = \theta(z). \quad (2.13)$$

$\theta(z, t)$ has solution in the form of Fourier series:

$$\begin{aligned} \theta(z, t) &= \frac{1}{2}a_0 + \sum_{n=1}^{\infty} a_n \cos(n\frac{\pi}{H}z) \times e^{-(n\pi/H)^2 \kappa t}; \\ a_i &= \frac{2}{H} \int_0^H \theta(z') \cos(i\frac{\pi}{H}z') dz', \quad i = 0, 1, 2, \dots \end{aligned} \quad (2.14)$$

where $H = 600$ m is the depth of the water column. To simplify the problem as much as possible, the salinity is set as constant (35.0 psu), and a linear equation of state

$$\sigma_\theta = 28.00 - 0.08 \times \theta \quad (2.15)$$

is used. Eq. 2.15 approximately describes the potential density of cold water masses near the Denmark Strait (Käse et al., 2003). In order to unify the mixing parameterization, a constant diffusivity $\kappa = 0.1 \text{ m}^2 \text{ s}^{-1}$ is applied in both KPP and TP, and the shear induced mixing is turned off. The model is run with baroclinic and barotropic time steps of 3600

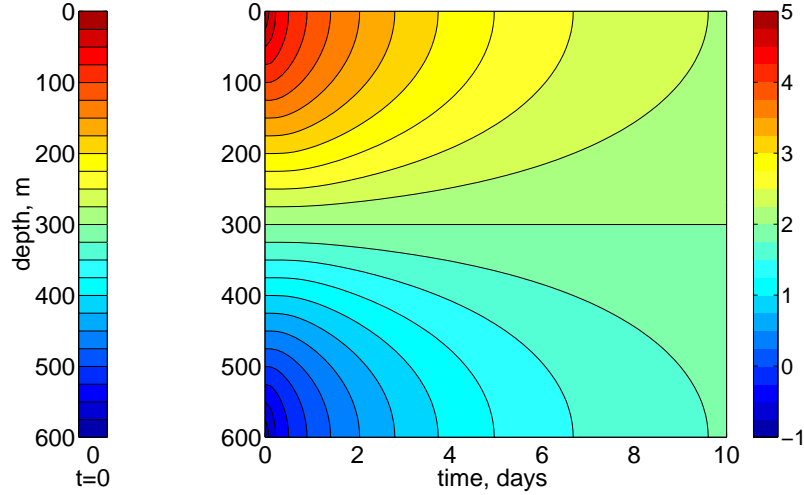


Figure 2.1: The initial (Left) and the analytical time evolution (Right) of the temperature profile for constant layer diffusion experiment.

and 360 sec, respectively.

2.2.1 Constant layer diffusion experiment

In the constant layer diffusion configuration, the water column is evenly divided into 12 isopycnal layers (50 m). The initial potential temperature θ decreases linearly along depth z as $\theta(z) = 5.00 - 0.01 \times z$. This initial profile and its analytical time evolution (Eq. 2.14) are plotted in Fig. 2.1.

The results of the HYCOM simulation are summarized in Fig. 2.2. Both approaches conserve precisely a vertical average θ of 2°C (Fig. 2.2a). In isopycnal coordinate, the time evolution of the isopycnal interface is symmetric in the vertical and compares well with the analytical solution, which was re-mapped onto the isopycnal coordinates of HYCOM. The differences become more significant where the layer outcrops at the surface or bottom, indicating that this is probably due to lack of resolution. The hybrid coordinate, however, shows a vertically asymmetric evolution of the interface (Fig. 2.2b). This can be explained by comparing the evolution of the temperature profile $\theta(z)$ (Fig. 2.2c and d). The isopycnal

condition is guaranteed in isopycnic coordinate, whereas it is up to the ‘regridding’ process in hybrid coordinate. The layers in the lower half of water column, for instance, are restored back to isopycnic conditions and the evolution of the interface is similar to that shown in Fig. 2.2c. The layer in the upper half, however, is not isopycnic because a minimum z -thickness is reached, which generates the z -coordinate. The interface evolution is similar to the analytical solution before re-mapped to isopycnic coordinate (i.e., Fig. 2.1). It is also worth mentioning that the mixing stops in isopycnic coordinate after a 2-layer system is reached, while it continues in hybrid coordinate even without moving the interface.

2.2.2 Massless layer inflation experiment

In the massless layer inflation configuration, the water column consists of two thick layers (300 m) with θ of 3.5 and 0.5°C and ten massless layers in between. The hybrid coordinate does not allow zero thickness in the interior and thus a minimum thickness (of 1 m) is applied. The initial temperature profile and analytical time evolution are plotted in Fig. 2.3.

The results of the HYCOM simulation are plotted in Fig. 2.4 in the same way as Fig. 2.2. Both approaches again have a vertical average θ of 2°C (Fig. 2.4a). Similar to Fig. 2.2, the evolution of layer interfaces in isopycnic coordinate is symmetric and consistent with that of analytical solution. The hybrid coordinate shows the same asymmetric feature for the same reason as in the constant layer diffusion experiment. However, the hybrid coordinate also shows a very different evolution during the first 2 days. It appears that the thin layers in the middle of the water column fail to inflate as smoothly and efficiently as in isopycnic coordinate. The reason is not only that those 10 layers have density that initially greatly differed from their reference, but also that the high diffusivity ($0.1 \text{ m}^2 \text{ s}^{-1}$)

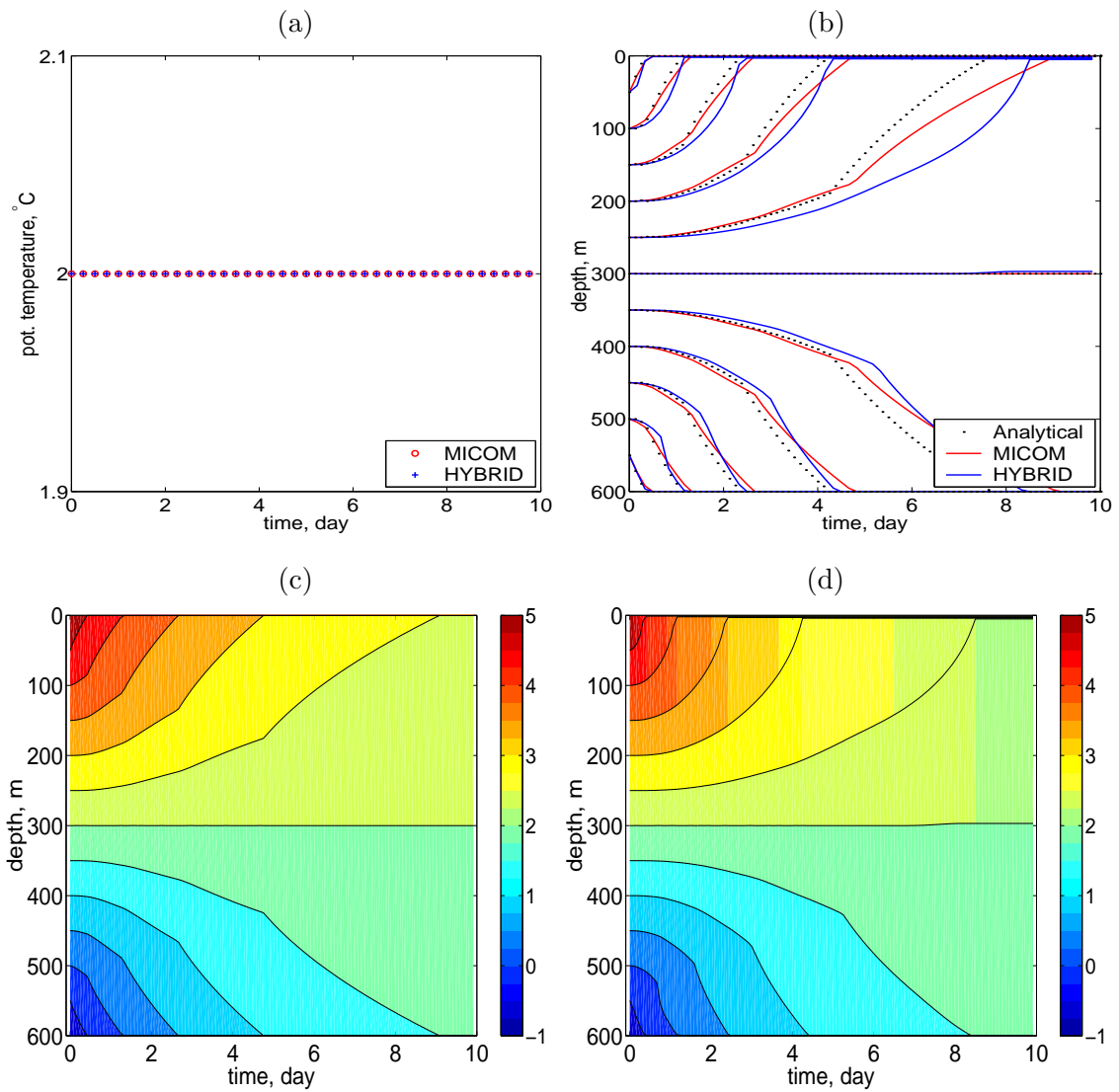


Figure 2.2: Results of constant layer diffusion experiment. Time evolution of (a) the vertically averaged pot. temperature; (b) the analytical results and simulated layer interface; (c) the evolutions of layer interface (lines) and $\theta(z)$ (color) in isopycnic coordinate; and (d) the evolutions of layer interface (lines) and $\theta(z)$ (color) in hybrid coordinate.

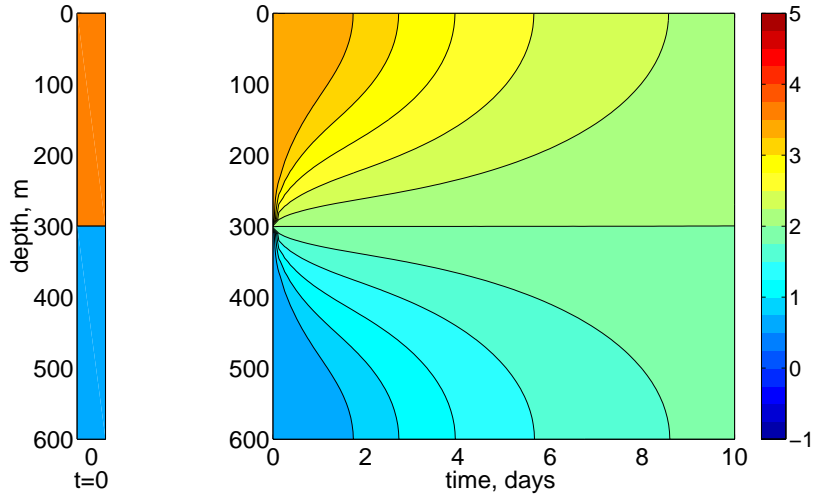


Figure 2.3: The same as Fig. 2.1 but for massless layer inflation experiment.

and long baroclinic time step (3600 sec) used cause one step of mixing to completely change the density of a thin layer.

To demonstrate this, we conduct two additional experiments using hybrid coordinate with the same configuration but shorter baroclinic time steps (360 and 36 sec, respectively). The results are illustrated in Fig. 2.5, from which we clearly see that as the time steps decrease, the inflation in hybrid coordinate becomes smoother and more efficient and compares better with that of isopycnic coordinate and with analytical results.

2.3 Two-dimensional ‘dam-break’ experiments

In section 2.2, we demonstrated that diapycnal mixing using different approaches can have the same numeric performance and can reproduce the analytical diffusion solutions. In this section, we investigate how KPP and TP compare in representing the outflow entrainment mixing.

An idealized two-dimensional like ‘dam-break’ configuration is designed (Fig. 2.6). The calculation domain has 130×7 grid points with a horizontal resolution of 0.05° (~ 5.5 km)

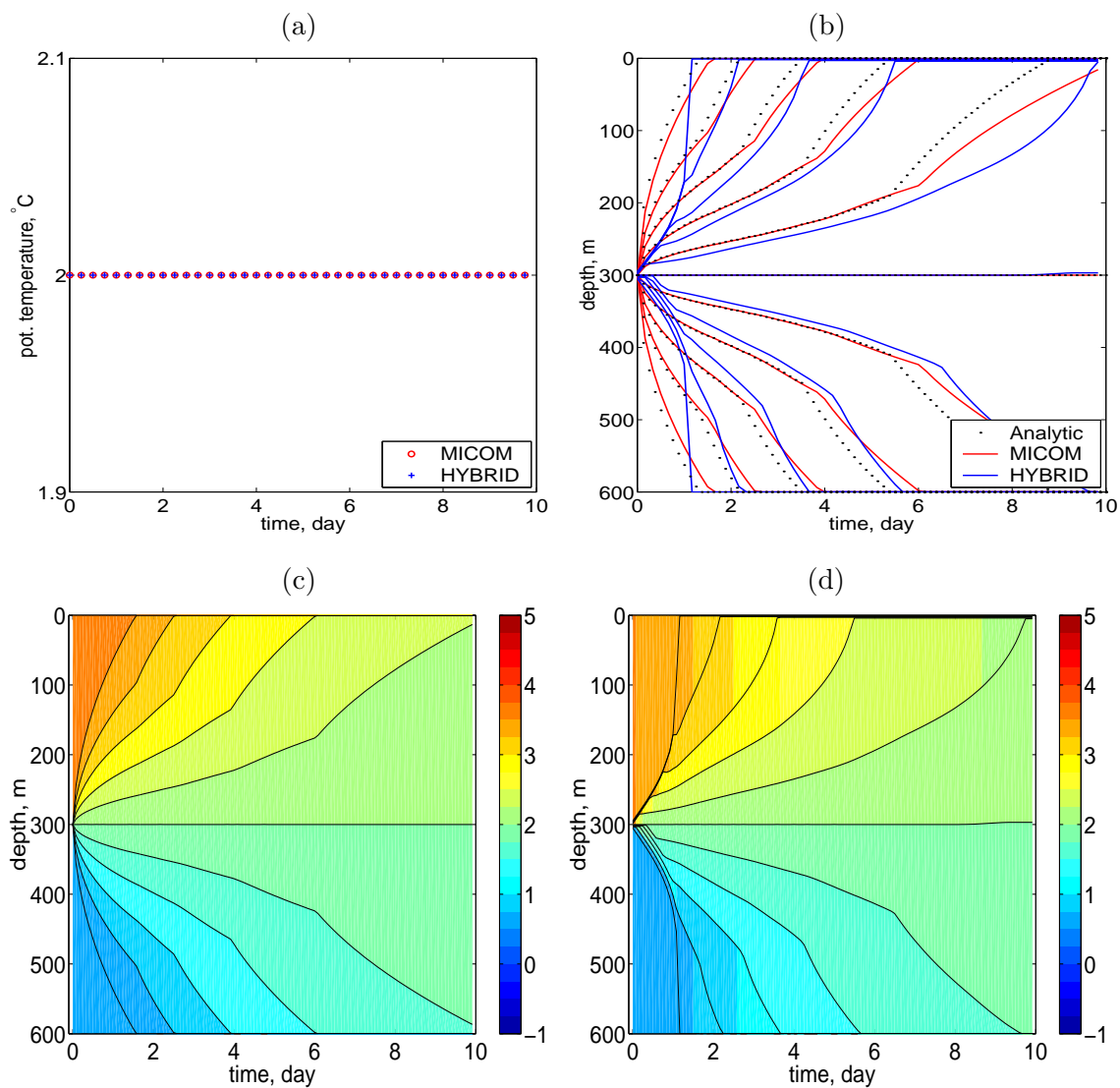


Figure 2.4: The same as Fig. 2.2 but for massless layer inflation experiment.

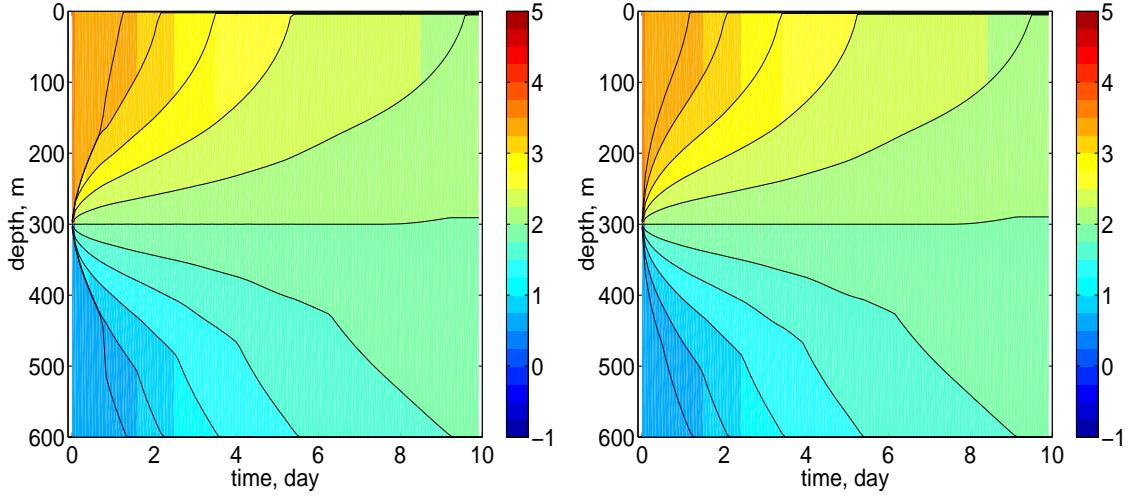


Figure 2.5: The same as Fig. 2.4d but with baroclinic time step of 360 sec (Left) and 36 sec (Right), respectively.

and 7 isopycnal layers in vertical. The bottom topography (H) is a smooth Gaussian function with minimum and maximum depth of 600 and 2000 m, respectively. The same linear equation of state (Eq. 2.15) is used. Two water masses (warm and cold), divided by a vertical front at the top of the sill, were initially filled in the west and east half of the sill. The reference isopycnals and the initial thickness of each layer in each basin are listed in Table 2.1. All four boundaries are closed and a free-slip boundary condition is applied. There is no surface forcing and rotation, so the flow is purely driven by the pressure gradient set up by the density contrast. The model is integrated for 4 days with baroclinic and barotropic time steps of 192 and 12 sec, respectively. Twin experiments differing only by the diapycnal mixing parameterization are conducted: one with KPP and the other with TP.

Table 2.1: The reference isopycnals and initial layer set up of the ‘dam-break’ configuration.

Layer k	1	2	3	4	5	6	7
$\hat{\sigma}_k$ (kg m^{-3})	27.60	27.68	27.76	27.84	27.92	28.00	28.08
h_k (m) west	10	$H - 10$	0	0	0	0	0
h_k (m) east	10	10	10	10	10	10	$H - 60$

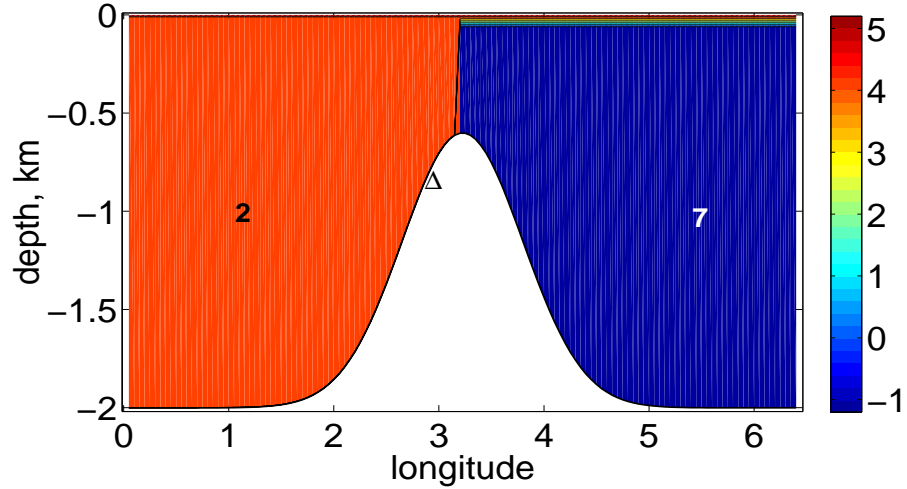


Figure 2.6: The vertical distribution of the pot. temperature before the dam break. Two water masses (θ of 5 and -1 °C) are divided by a vertical front on top of the Gaussian topography.

The vertical distribution of the potential temperature 4 days after the ‘dam-break’ is presented in Fig. 2.7. The contrast is clear and dramatic. In KPP, the mixing is so weak that the interfacial layers are barely inflated and the outflow water at the bottom of the sill retains its original properties (layer 7), whereas in TP the original water mass is mixed out at the flat bottom and the outflow water mainly consists of water of layer 3. This snapshot difference is reflected quantitatively (Fig. 2.8) as we diagnose the fraction of the total volume of outflow water masses (layer 3 \sim 7) in the west half of the domain. The volume of outflow water in the KPP experiment is only about half of that in TP. More importantly, the outflow is mainly from layer 7 in KPP experiment, but layer 3 in TP.

To explain the reason for this difference, we compare the time evolution of the diffusion coefficient κ and Richardson number Ri at a location near the top of the sill (marked as Δ in Fig. 2.6). The diffusivity in TP is estimated based on the definition of buoyancy flux (Eq. 2.7):

$$\kappa_k = F_k \frac{h_k}{\Delta \rho_k}. \quad (2.16)$$

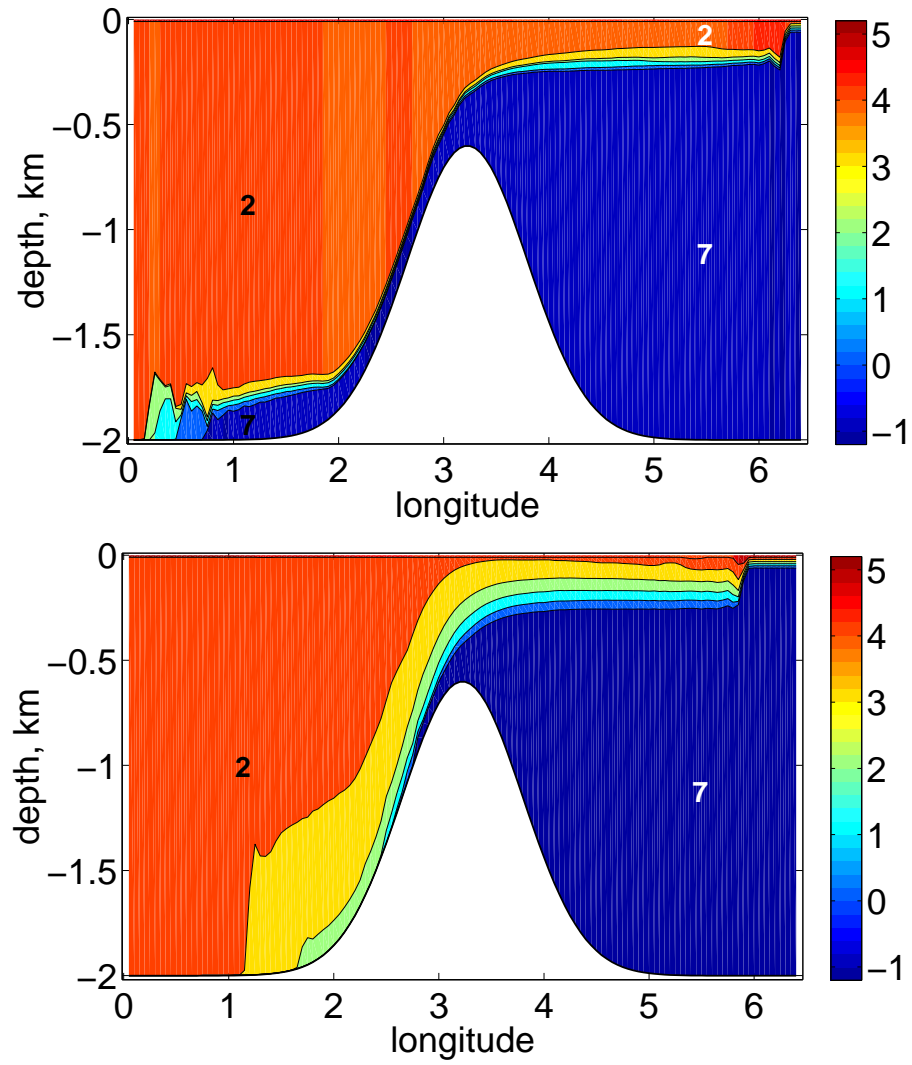


Figure 2.7: The vertical distribution of pot. temperature 4 days after the ‘dam-break’ along zonal section in HYCOM using KPP (upper panel) and TP (lower panel).

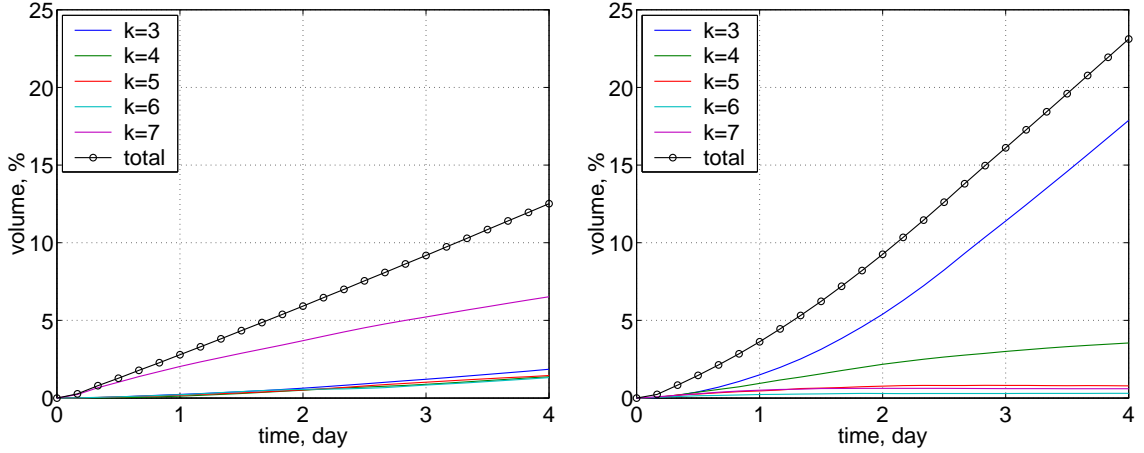


Figure 2.8: The time evolution of volume percentage of the outflow water (layer 3 ~ 7) in the west half of domain. KPP (left panel) and TP (right panel).

and the results are plotted in Fig. 2.9. Several points are worth of mentioning. First, the diffusivity in TP is about two orders of magnitude higher than that in KPP, explaining the dramatic difference shown in Figs. 2.7 and 2.8. The difference is due to the fact that diffusivity in KPP is constrained by K_{max} , while no such constraint is present in TP. Second, we might expect a higher value of Ri in KPP than in TP, because mixing in both schemes is parameterized as a function inversely proportional to Ri . This is not the case, however; Ri is actually significantly lower in KPP than in TP, since mixing in turn alters the velocity shear and stratification and hence the Ri . The weak mixing of KPP forces Ri to be small, whereas the strong mixing of TP keeps Ri close to $Ri_c = 0.8$.

Two converging experiments are conducted in order to further investigate whether it is the parameterization itself or the re-gridding process in the KPP implementation that leads to the different mixing shown in Fig. 2.7. The premise is that, if the difference is due to the mixing parameterization, the result would converge when one parameterization is modified to match the other. The experiments are listed in table 2.2. In *EXPT A*, KPP is unchanged, while TP is modified by constraining the buoyancy fluxes (Eq. 2.7) with a maximum diffusivity K_{max} . Therefore, the mixing in TP should become similar to that of

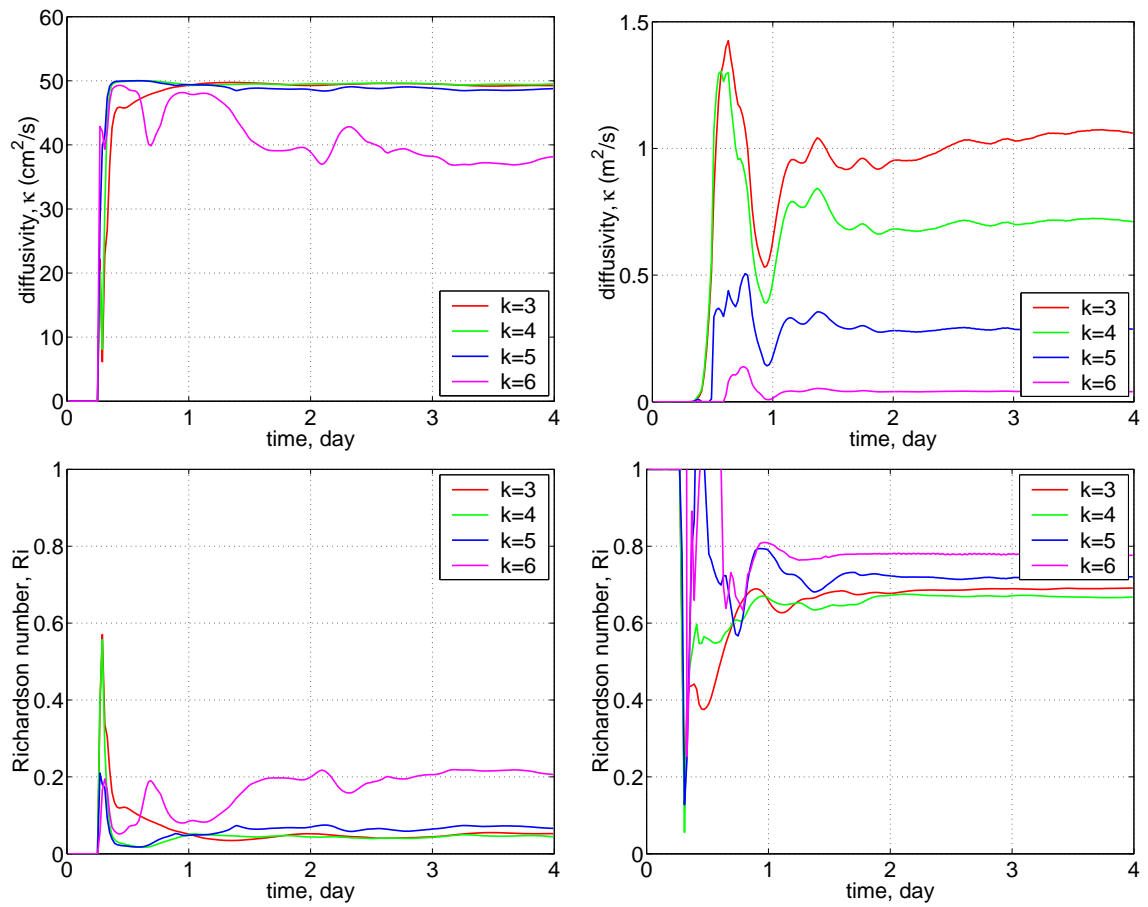


Figure 2.9: The time evolution of Ri and κ at station near the slope in HYCOM using KPP (left panels) and TP (right panels).

KPP. Different values of K_{max} are tested. In *EXPT B*, TP is essentially unchanged but Eq. 2.9 is multiplied by a factor C ($0 < C < 1$) to provide a different magnitude of mixing:

$$w_E = C\Delta U \frac{0.08 - 0.1Ri}{1 + 5Ri}. \quad (2.17)$$

In KPP, instead of using Eq. 2.2, the diffusivity K is diagnosed from Eq. 2.16 in which the calculation of the buoyancy flux F_k follows the same approach and parameterization as in TP (Eq. 2.8 and Eq. 2.17). Therefore, the mixing in KPP should become similar to that of TP. Similarly, three different values of C are tested.

Table 2.2: The modified mixing parameterization in converging experiments.

<i>EXPT A</i>	KPP unchanged; TP modified by constraining the buoyancy flux with K_{max} ; 3 values of K_{max} are tested: 0.01, 0.05 and $0.25 \text{ m}^2 \text{ s}^{-1}$.
<i>EXPT B</i>	TP (with Eq. 2.17); KPP modified by calculating diffusivity K from TP Eq. 2.16; 3 values of C are tested: 0.1, 0.2 and 0.5.

The results of converging experiment ‘*EXPT A*’ are presented in Figs. 2.10 and 2.11. For each K_{max} , the constrained TP produces a similar potential temperature distribution as in KPP. The volume of outflow with different water properties is also much more comparable than that seen in Fig. 2.8. And the increase in K_{max} clearly results in more entrainment, indicating that K_{max} indeed works as a hard limit on the entrainment. In a similar manner, the results of converging experiment ‘*EXPT B*’ are plotted in Figs. 2.12 and 2.13. The mixing between the modified KPP and TP compares well both in terms of the snapshot of temperature distribution and the time evolution of the outflow water volume. The total volume does not change dramatically when the factor C increases from 0.1 to 0.5. However, more dense water is clearly present in the $C = 0.1$ case, indicating less entrainment. It is

also worth mentioning that for both converging experiments, layer 2 in hybrid coordinate is not isopycnic (Fig. 2.10 and 2.12). This partially contributes to the difference in outflow volume between the TP and KPP simulations.

2.4 Summary and discussion

In this chapter, we compared the K-profile parameterization (KPP) and the Turner parameterization (TP) in representing the entrainment process of outflows. They differ in two ways. a) Numerically, KPP in HYCOM modifies the vertical density profile, and a ‘re-gridding’ process is used to restore the isopycnic condition. TP, on the other hand, directly solves a nonlinear equation of layer thickness. b) Both schemes are Richardson number (Ri) dependent. KPP prescribes the mixing coefficient (K) as a constant times a function of Ri , whereas TP describes the net entrainment velocity (w_E) into a layer by the velocity difference (ΔU) times another Ri -dependent function.

1-D diffusion experiments were first carried out to document the numerical performance of the two approaches (i.e., changing density vs. changing thickness) in implementing the diapycnal mixing. The comparisons show that these two approaches lead to similar results and that both are consistent with the analytical solution. Two idealized ‘dam-break’ experiments, which differed in the diapycnal mixing parameterization (KPP vs. TP) only, were then conducted. Large differences were found, with the experiment using TP showing much stronger entrainment than the one using KPP because of a higher value of effective diffusivity. An additional series of converging experiments further demonstrated that the differences are purely due to the differences in the parameterization. The K_{max} in KPP puts a hard limit for the shear-induced mixing, while such a constraint is avoided in TP by relating the entrainment velocity w_E to the velocity shear ΔU itself.

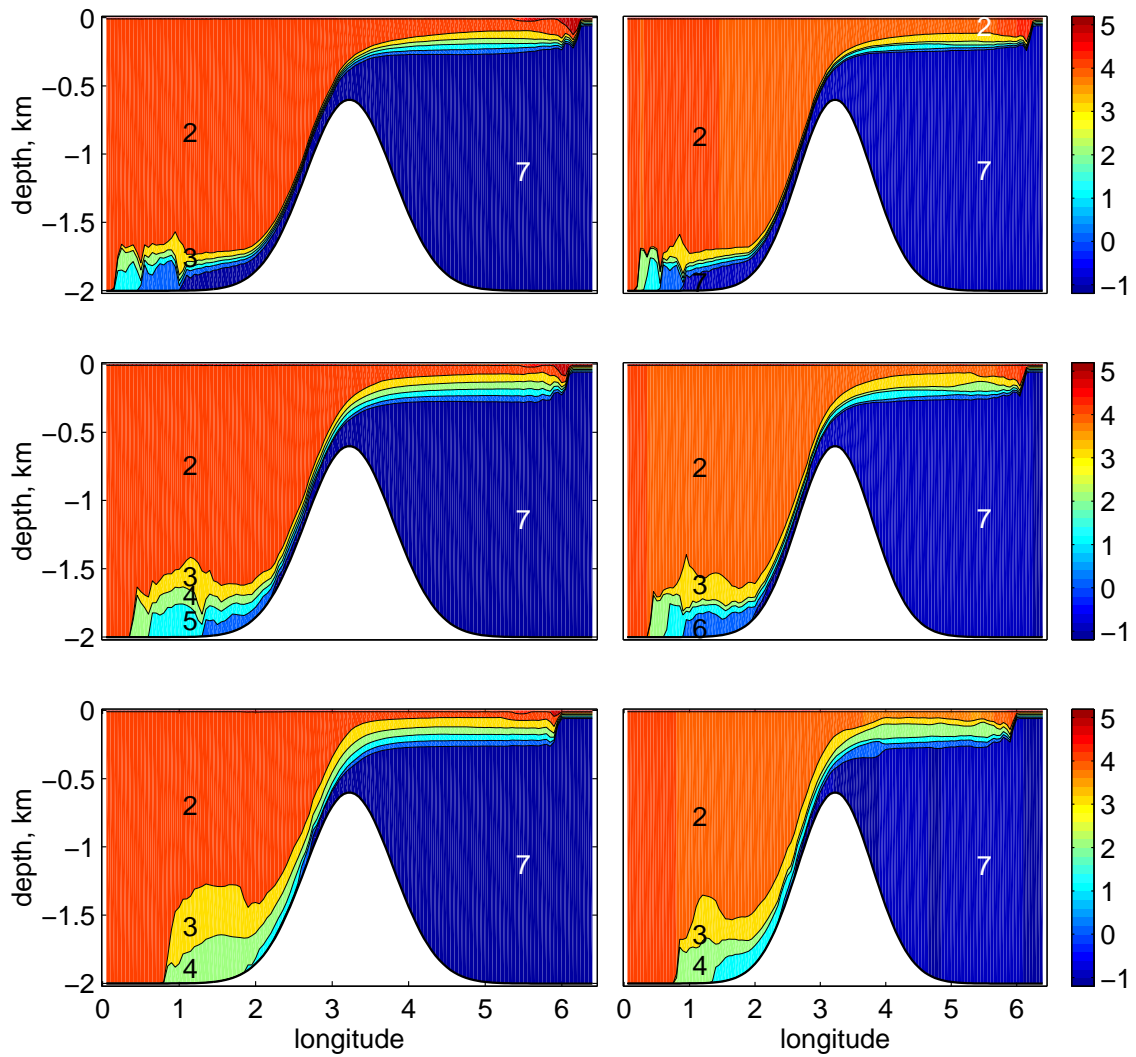


Figure 2.10: Result of EXPT A. The vertical distribution of pot. temperature in HYCOM using constrained TP (left panels) and KPP (right panels). From top to bottom, κ_{max} used are 0.01, 0.05 and $0.25 \text{ m}^2 \text{ s}^{-1}$ respectively.

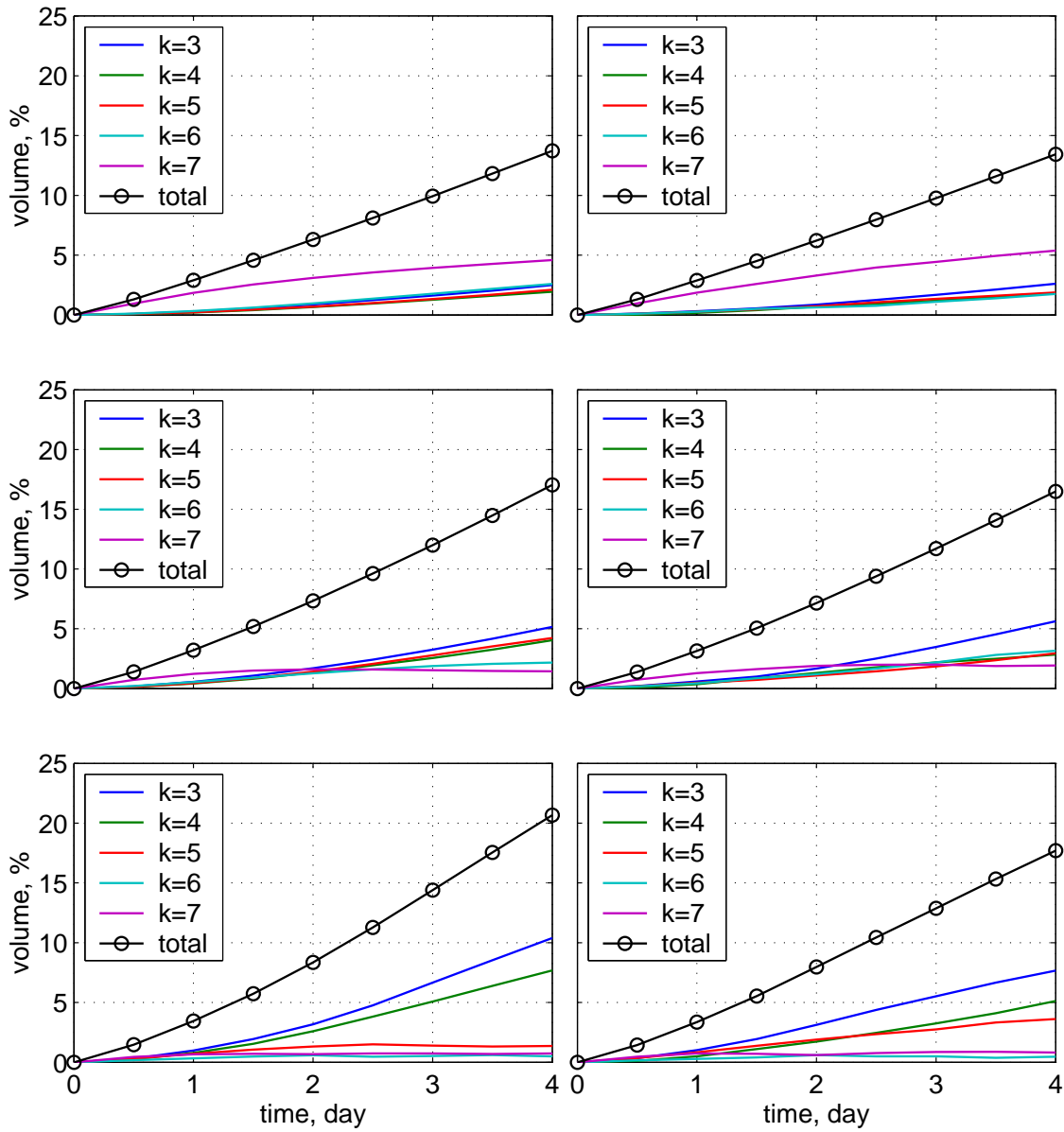


Figure 2.11: Result of EXPT A. The percentage of outflow water in the west half of the domain as function of time in HYCOM simulations using constrained TP (left panels) and KPP (right panels). From top to bottom, κ_{max} used are 0.01, 0.05 and 0.25 $\text{m}^2 \text{s}^{-1}$ respectively.

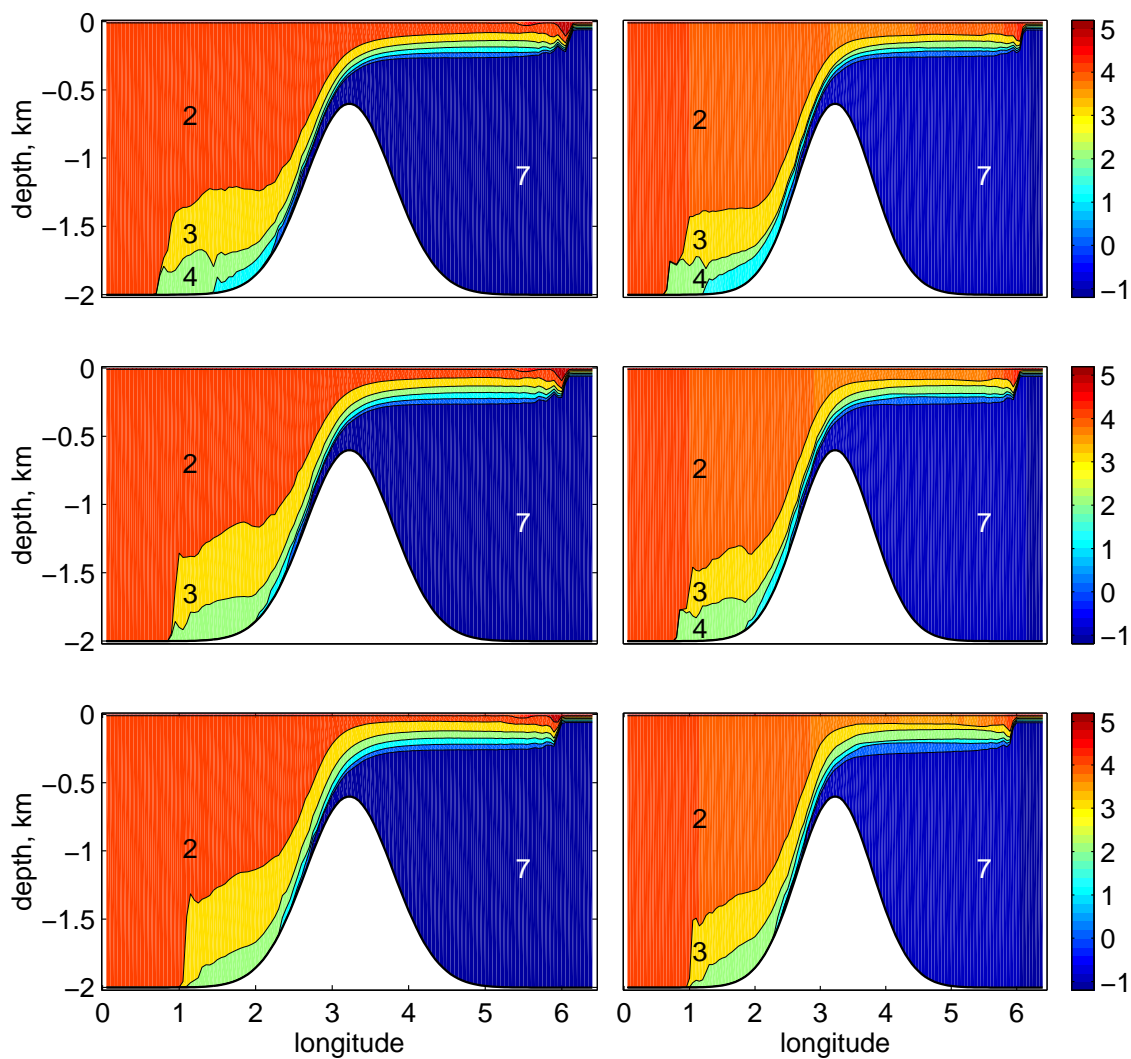


Figure 2.12: Result of EXPT B. The vertical distribution of pot. temperature in HYCOM using TP (left panels) and modified KPP (right panels). From top to bottom, factor C used are 0.1, 0.2 and 0.5 respectively.

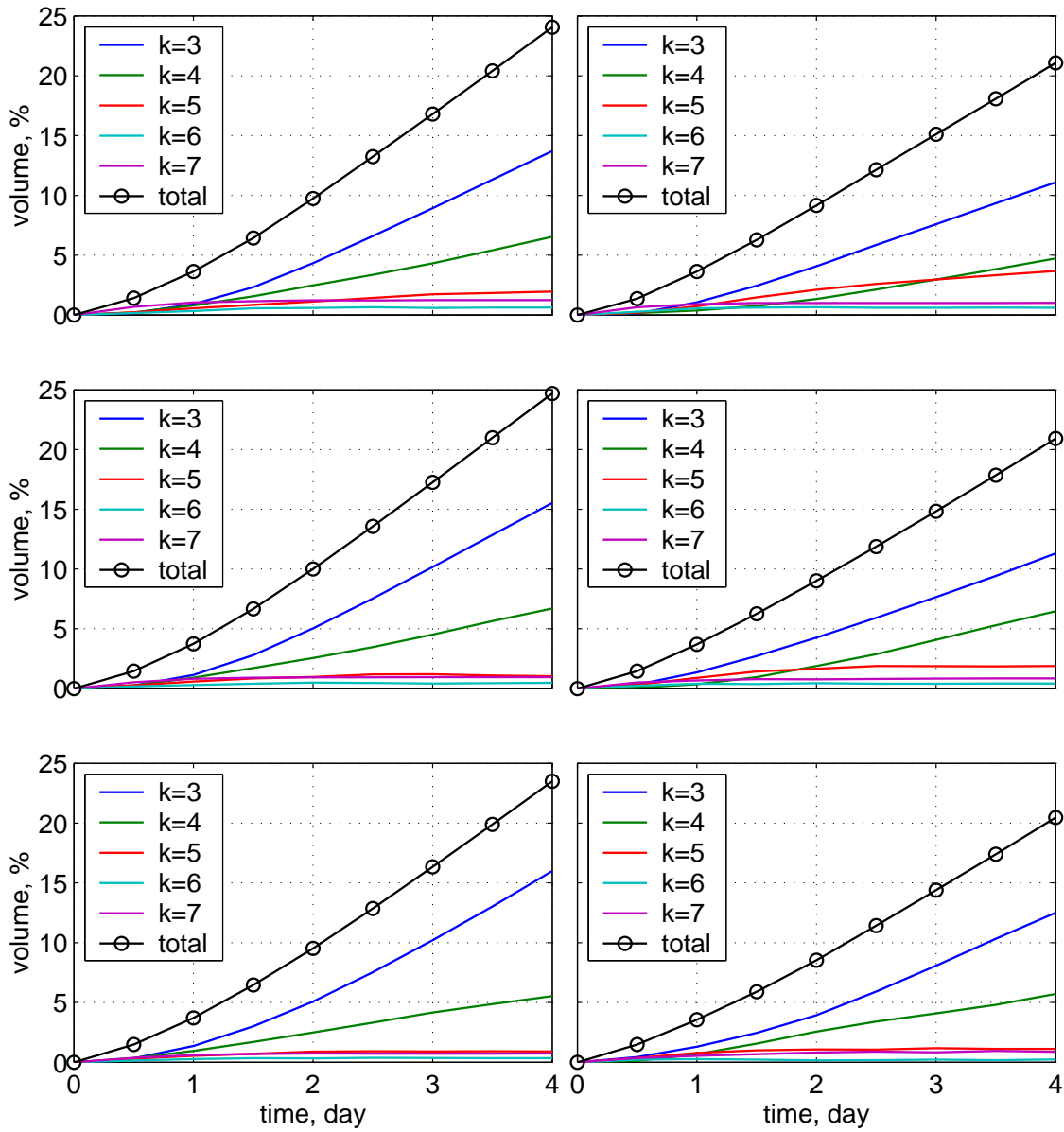


Figure 2.13: Result of EXPT B. The percentage of outflow water in the west half of the domain as function of time in HYCOM simulations using TP (left panels) and modified KPP (right panels). From top to bottom, factor C used are 0.1, 0.2 and 0.5, respectively.

This comparison sheds no light on which parameterization is more appropriate for outflow entrainment due to the lack of an independent ground truth. Further studies have been done by Chang et al. (2005), in which HYCOM simulations of gravity currents flowing over constant slopes are run with both KPP and TP, and where the results are compared to those of similarly-configured experiments from a nonhydrostatic, high-resolution model. The comparison shows that, as in the experiments presented in this chapter, the KPP-induced mixing is too weak, the while TP-induced mixing is too strong. Both parameterizations therefore need to be changed.

We previously noted that KPP can not be universally valid because of its simplistic formulation. The constant K_{max} used for interior mixing was determined from the large eddy simulations (LES) of the diurnal cycle of the surface mixed layer at the equator, which may not be representative of outflow scenario. Physical intuition leads to the expectation that K_{max} should vary with the strength of the forcing. Such turbulence dependence to forcing is included in KPP in the surface boundary layer via parameterizing the effect of wind and buoyancy forcing, convective adjustment, and non-local T/S fluxes. It is not included in outflow because first, there is no well-resolved bottom boundary layer, and second, the outflow forcing is primarily the downslope component of the reduced gravity, i.e., the buoyancy contrast between the outflow and ambient water, and the bottom slope angle.

TP relates the entrainment velocity w_E to the velocity shear ΔU rather than to a dimensional constant. This allows TP to have different magnitudes of mixing in response to various outflow forcing, which in part determines the speed of the outflow current and hence the shear. Chang et al. (2005) further show that, as the gravity current flows over different bottom slope angles, TP shows different levels of entrainment, while KPP does

not. Therefore TP has a more appropriate formulation for parameterizing the outflow entrainment than does KPP. However, one assumption underlying the concept of entrainment in Turner (1986) is that the entire gravity current is viewed as a single layer, so that ΔU and Ri_B in Eq. 2.9 are ‘bulk’ properties averaged over the cross-section of a stream-tube. The use of Ri_k raises an issue as to whether the local layer Ri_k s are able to represent the bulk Ri_B . Specifically, the real skill of an isopycnic model in representing a gravity current lies in the ability to migrate its resolution to the interfacial between the gravity current and the ambient water above. Thus, the layer Ri_k effectively becomes the shear Ri as defined by Eq. (2.3), leaving the implementation of Eq. (2.9) without a solid experimental foundation.

Chapter 3

Development of an entrainment parameterization using a high-order nonhydrostatic model

The aim of this chapter is to develop an entrainment parameterization of the form

$$E \equiv \frac{w_E}{\Delta U} = f(Ri), \quad (3.1)$$

in which Ri is the local layer Richardson number as defined in Eq. 2.11. We maintain a TP-like structure and keep ΔU as a relevant scale for w_E because 1) physically, the turbulence produced due to interfacial shear is the dominant energy source for mixing (Narimousa and Fernando, 1987); and 2) this allows different magnitudes of mixing in response to various forcings. The Ri -dependent function $f(Ri)$ is determined experimentally by comparing simulations of a generic gravity current flowing over various bottom slope with the hydrostatic HYCOM and a high resolution, nonhydrostatic model Nek5000.

3.1 The nonhydrostatic model Nek5000

The high-resolution simulation results from the 3-dimensional, nonhydrostatic, spectral element Navier Stokes solver Nek5000 (Fischer, 1997; Fischer et al., 2000; Fischer and Mullen, 2001) are used as our ground truth. Nek5000 is based on the spectral element method (SEM) and offers several advantages in various respects: a) combining the geometric flexibility of the finite element method with the numerical accuracy of spectral expansion, b) minimal dissipation and dispersion errors, c) providing convergence by increasing either elemental grid resolution or the polynomial degree, and d) computational advantages for scalability on parallel computers (Tufo and Fischer, 1999). The application to studies of bottom gravity currents with this model has been discussed in detail in Özgökmen and Chassignet (2002); Özgökmen et al. (2004b,a, 2005) and Chang et al. (2005). The model is able to resolve the turbulent mixing associated with gravity current, and to reproduce the major plume features as observed in laboratory experiments.

In the present set-up, Nek5000 is configured to solve the equations:

$$\begin{aligned}
 \left(\frac{\partial}{\partial t} + \mathbf{u} \cdot \nabla \right) \mathbf{u} &= -\nabla p + \left(\frac{\partial^2}{\partial x^2} + \frac{\partial^2}{\partial y^2} + r \frac{\partial^2}{\partial z^2} \right) \mathbf{u} - Ra S \hat{\mathbf{z}}, \\
 \nabla \cdot \mathbf{u} &= 0, \\
 \left(\frac{\partial}{\partial t} + \mathbf{u} \cdot \nabla \right) S &= Pr^{-1} \left(\frac{\partial^2}{\partial x^2} + \frac{\partial^2}{\partial y^2} + r \frac{\partial^2}{\partial z^2} \right) S.
 \end{aligned} \tag{3.2}$$

The variables in Eq. 3.2 are the velocity vector $\mathbf{u} = (u, v, w)$, salinity S , and pressure p . Parameters include a nondimensional Rayleigh number Ra representing the ratio of the strengths of buoyancy and viscous forces, the Prandtl number Pr representing the ratio of viscous and salinity diffusion, and the ratio of vertical and horizontal diffusivity r .

Table 3.1: Parameters of the Nek5000 nonhydrostatic model simulations.

Domain size ($L_x, L_z = H, L_y$)	(10 km, 1 km, 2 km)
Bottom slope (θ)	$1^\circ, 2^\circ, 3^\circ, 4^\circ$
Rayleigh number (Ra)	5×10^6
Prandtl number (Pr)	1
Ratio of vertical to horizontal diffusivity (r)	2×10^{-2}
Salinity range (S)	1.0 psu
Number of elements (x, z, y)	50, 8, 10
Polynomial degree (N)	6
Number of grid points	864,000
Time step (Δt)	0.85 sec

3.2 Experimental configuration

The Nek5000 channel-like model domain has a horizontal, streamwise length L_x of 10 km and a spanwise width L_y of 2 km. The depth of the water column at the inlet ($x = 0$) is $h_i = 400$ m. The maximum depth can reach 1000 m depending on the geometry dictated by constant slope angles of $\theta = 1^\circ, 2^\circ, 3^\circ$, and 4° . The boundary conditions at the bottom are no-slip and no normal flow for velocity, and no normal flux for salinity, $\partial S / \partial \mathbf{n} = 0$, where \mathbf{n} is the normal to the boundary. Rigid-lid and free-slip boundary conditions are used at the top. The model is initialized by placing a salty and therefore dense water mass at the top of the slope, and is driven by specifying velocity and salinity profiles at the inlet boundary. Periodic boundary conditions are applied at the channel sides. The domain is discretized using 4000 elements with 6th order polynomials in each spatial direction within the elements, so that a total of 864,000 grid points are employed. The remaining model parameters are listed in table 3.1 and the reader is referred to Özgökmen et al. (2004b) and Chang et al. (2005) for further details.

The configuration of the HYCOM experiments is set up to closely mimic that of Nek5000. The computational domain has a 20 km long, 2 km wide sloping bottom with the same angles

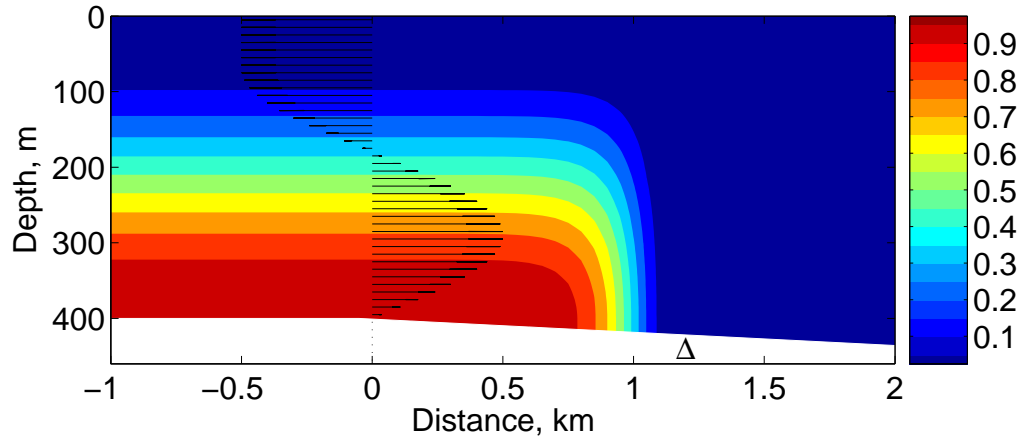


Figure 3.1: The initial distribution of the salinity anomaly and velocity profile in the relaxation zone ($x = -1$ to $x = 0$ km) in the HYCOM configuration. $X_0 = 1.2$ km is marked as a ‘ Δ ’.

as in Nek5000. A horizontal resolution of 100 m is used in all experiments. There are in total 7 layers in the vertical: a thin (10 m) mixed layer on top and 6 isopycnic layers corresponding to salinity anomalies of 0.0, 0.2, 0.4, 0.6, 0.8, and 0.9 psu. The initial condition consists of the same dense saline water over the first 1 km of the slope as in Nek5000. In a 1 km long relaxation zone of 400 m constant depth, the salinity and velocity profiles are relaxed to the Nek5000 profiles (Fig. 3.1).

3.3 Results from the nonhydrostatic 3D model

The evolution of the salinity distribution in Nek5000 experiments is shown in Fig. 3.2. The basic characteristics of such a flow field have been described and quantified in Özgökmen et al. (2004b), to which we refer the reader for further details. Fig. 3.2 clearly demonstrates that, as the slope angle increases, the turbulent overturning structures between the gravity current and the ambient fluid become larger and more vigorous, an indication of enhanced mixing and entrainment.

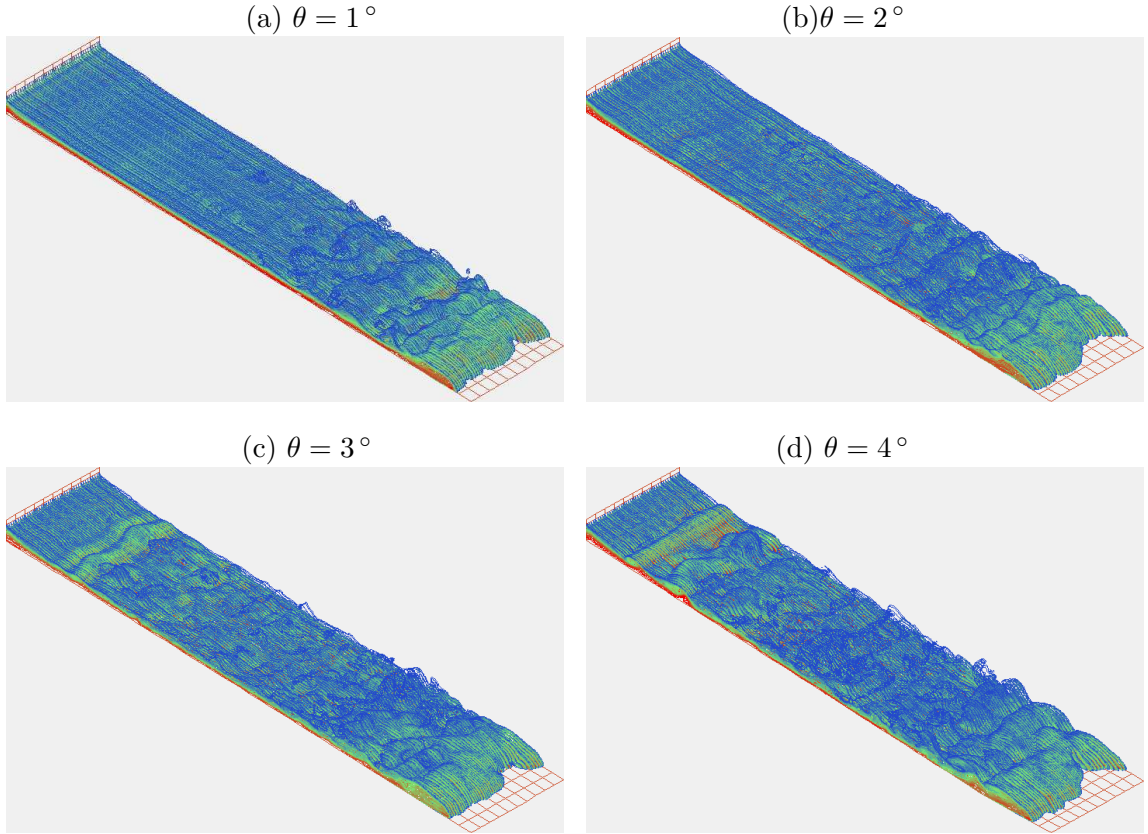


Figure 3.2: Snapshots of the salinity anomaly distribution in Nek5000 experiments with 4 different slope angles when the gravity current reaches the end of the domain.

In order to average over the 3D mixing structures, a spanwise-averaged length, or propagation distance of the gravity current, $\ell(t)$, is defined as

$$\ell(t) = L_y^{-1} \int_0^{L_y} X_F(y', t) dy' - X_0. \quad (3.3)$$

Here, $X_0 = 1.2$ km is a reference location immediately downstream of the dense water pool at the top of the slope before any entrainment occurs in Nek5000 or HYCOM, and $X_F(y, t)$ represents the leading edge of the plume. Its propagation speed is then defined as

$$U_F(t) = d\ell(t)/dt. \quad (3.4)$$

In the time evolution of ℓ and U_F (Fig. 3.3), the modeled gravity currents quickly attain a nearly constant speed of propagation for all slope angles. This property is well known from lock-exchange flows (e.g., Keulegan, 1958) and constant-flux gravity currents (e.g., Ellison and Turner, 1959; Britter and Linden, 1980). The propagation speed is insensitive to variations in slope angle for large θ since the increase in buoyancy force resulting from a greater slope angle is approximately compensated by the buoyancy gain from increased entrainment. Fig. 3.3 shows that there is approximately a 20% variation in U_F over the range of slope angles from $\theta = 1^\circ$ to 4° , which can be explained by the greater effect of the bottom friction at small slopes (Britter and Linden, 1980). With increasing θ , the corresponding change in U_F becomes increasingly smaller (Fig. 3.3).

The comparison of the Nek5000 and HYCOM simulations is quantified by an entrainment parameter \mathcal{E} and a volume-averaged salt flux F_S . Turner (1986) defines the entrainment \mathcal{E} as the change of the plume thickness h in the streamwise direction X :

$$\mathcal{E} \equiv \frac{dh}{dX}. \quad (3.5)$$

Following Özgökmen et al. (2004b), this is rewritten as

$$\mathcal{E}(t) \equiv \frac{\bar{h}(t) - \bar{h}_0(t)}{\ell(t)}, \quad (3.6)$$

where $\bar{h}(t)$ is the mean thickness between the reference location X_0 and the leading edge of the density current X_F :

$$\bar{h}(t) \equiv \frac{1}{\ell(t) L_y} \int_0^{L_y} \int_{X_0}^{X_F(y,t)} h(x', y', t) dx' dy'. \quad (3.7)$$

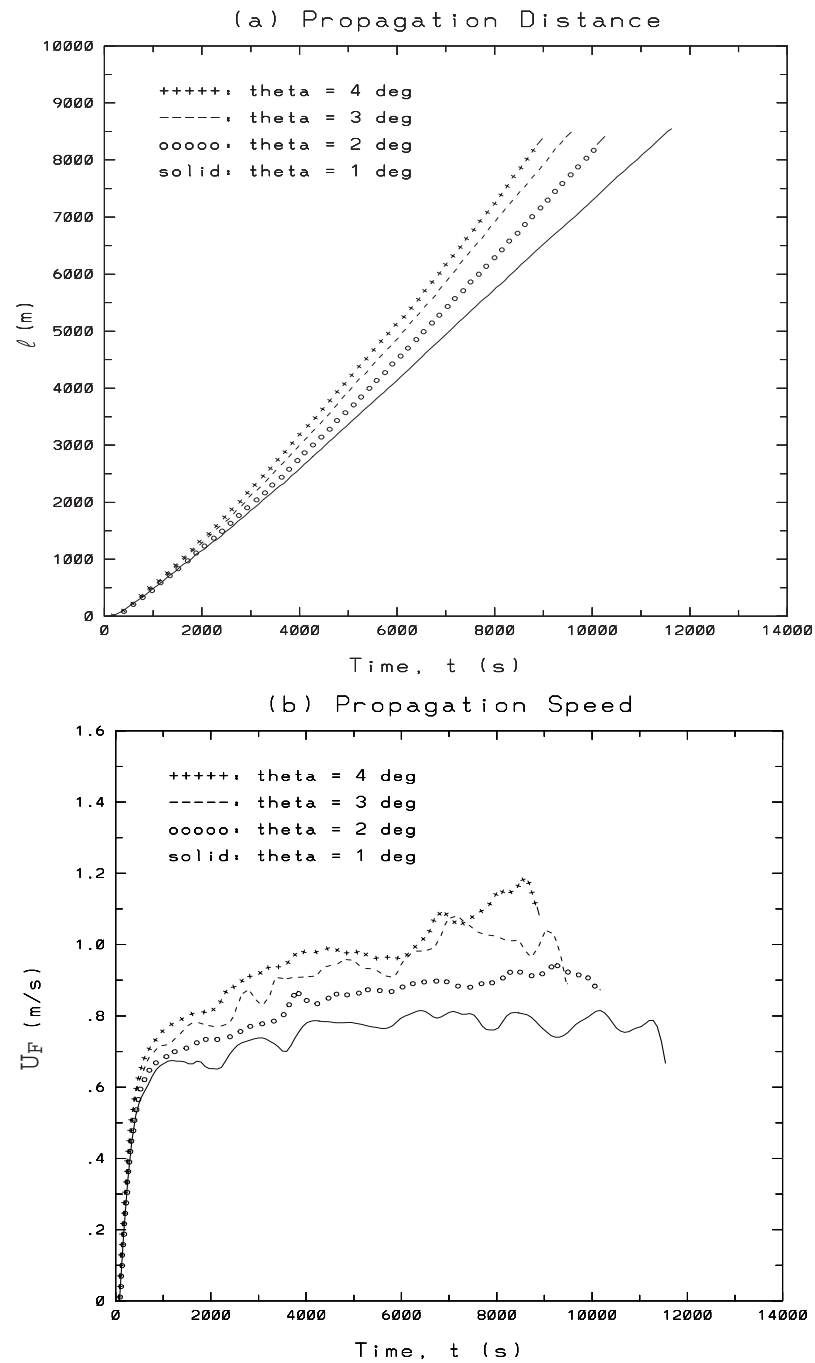


Figure 3.3: (a) Propagation distance ℓ in m and (b) propagation speed U_F in m s^{-1} of the gravity currents as a function of time in Nek5000 experiments with four slope angles.

The gravity current thickness h in (3.7) is defined as

$$h(x, y, t) \equiv \int_0^{z^b} \delta(x, y, z', t) dz', \text{ where } \delta = \begin{cases} 0, & \text{if } S'(x, y, z, t) < \epsilon \\ 1, & \text{if } S'(x, y, z, t) \geq \epsilon \end{cases}. \quad (3.8)$$

S' in Eq. 3.8 is the salinity anomaly, and the top of the plume is taken to be $\epsilon = 0.2$ psu surface since it delineates the coherent part of the gravity current in the Nek5000 simulations. Fluid particles with lower salinity tend to be detached from the current and to be advected with the overlying counter flow. Finally, $\bar{h}_0(t)$ in (3.6) is the mean thickness between X_0 and X_F when there is no entrainment. It is physically equivalent to the volume passing X_0 divided by the distance $\ell(t)$ and spanwise width L_y :

$$\bar{h}_0(t) \equiv \frac{1}{\ell(t) L_y} \int_0^t \int_0^{L_y} \int_{z^b+h}^{z^b} u(X_0, y', z', t') dz' dy' dt'. \quad (3.9)$$

The volume-averaged salt flux F_S ($\text{kg m}^{-2} \text{s}^{-1}$) is defined as

$$F_S(t) \equiv \frac{1}{\bar{X}_F(t) L_y h_0} \int_0^{X_F} \int_0^{L_y} \int_{z^b+h}^{z^b} \frac{\rho S'}{1000} u(x', y', z', t) dz' dy' dx', \quad (3.10)$$

where S' , h , and L_y are the salinity anomaly, gravity current thickness, and spanwise width, respectively. \bar{X}_F is the spanwise-averaged position of the gravity current edge, X_F , and $h_0 = 200$ m is the initial plume thickness.

Fig. 3.4 shows the evolution of the entrainment parameter \mathcal{E} and salt flux F_S as functions of plume propagation distance ℓ from the Nek5000 runs. For four runs, the entrainment parameter consistently decays with distance after the initial transients (Fig. 3.4a). Similar results are found in Özgökmen et al. (2004b) and Chang et al. (2005). We choose to present the evolution as a function of distance $\ell(t)$ rather than of time, in order to allow for

the same development in mixing along the plume path. As expected, $\mathcal{E}(\ell)$ increases with increasing bottom slope θ , with the variation magnitude comparable to Turner's (1986) formula $\mathcal{E} = 10^{-3} \times (5 + \theta)$. The salt flux $F_S(\ell)$ reaches an equilibrium value shortly after the initial descent of the gravity currents (Fig. 3.4b). The variations in S_F for different θ are due to the different gravity current velocities and entrainment characteristics as well.

3.4 HYCOM with linear parameterization functions

In order to keep the parameterization functions as simple as possible, we experiment with linear functions of the form:

$$E = \begin{cases} E_0 \left(1 - \frac{Ri}{Ri_c}\right), & \text{when } 0 \leq Ri < Ri_c \\ 0, & \text{when } Ri \geq Ri_c. \end{cases} \quad (3.11)$$

Since both E_0 and Ri_c are unknown, our first step is to investigate the effect of varying these two parameters: increasing E_0 means a larger magnitude of the entrainment, while increasing Ri_c implies that the gravity current can entrain over a wider range of flow conditions. Different combinations of E_0 and Ri_c might produce either different or somewhat similar evolution of the entrainment parameter $\mathcal{E}(\ell)$. We therefore seek to obtain the optimal values of E_0 and Ri_c in Eq. (3.11), or an envelope of functions from which a unified scheme could be developed.

Following this consideration, 4 experiment sets, A, B, C, and D, corresponding to four different values of Ri_c (Table 2), are performed. Each set is tested with 6 different values of E_0 . The chosen range of $Ri_c = 0.25$ to $Ri_c = 0.75$ spans plausible values between the linear stability threshold of stratified shear flows (Miles, 1961) and the onset of turbulence in laboratory experiments (Rohr et al., 1988) to the cut-off bulk Richardson numbers (Turner,

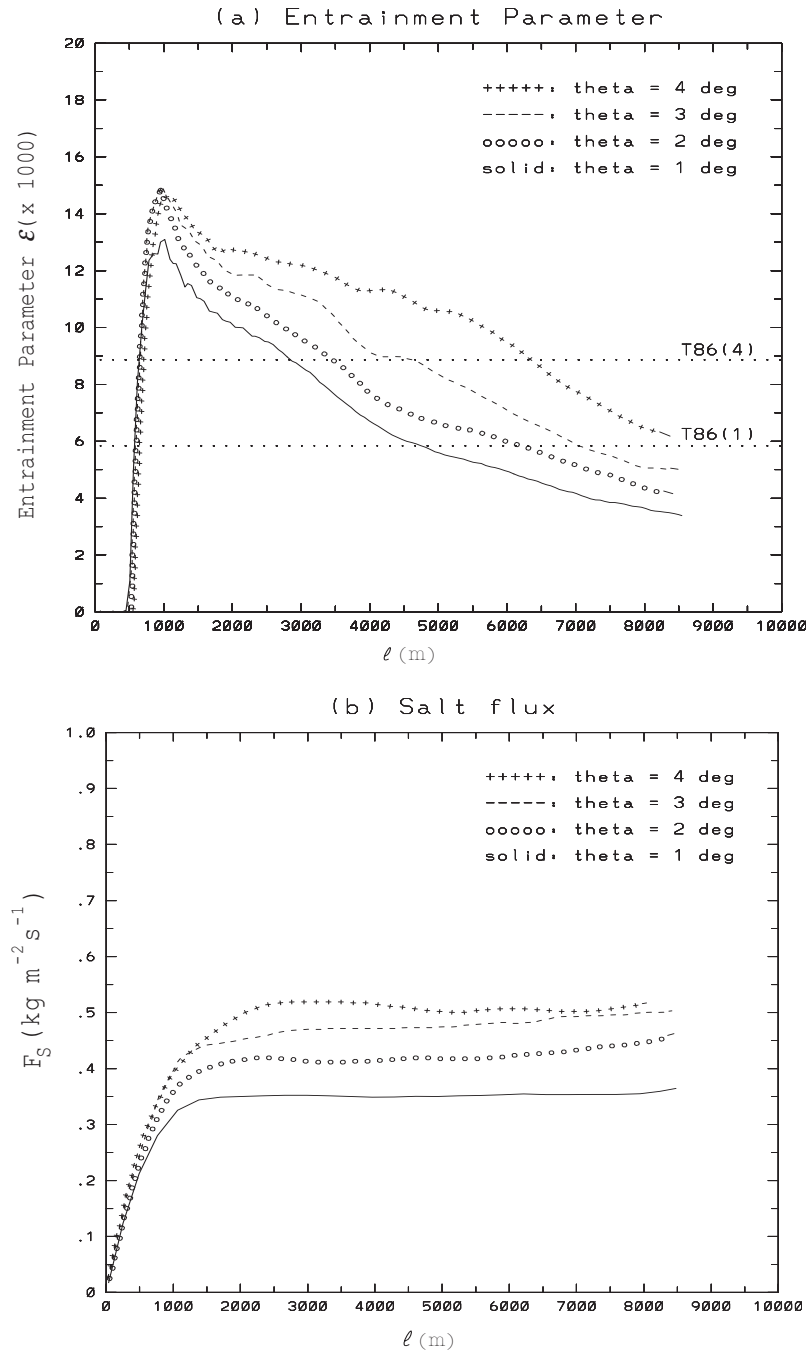


Figure 3.4: (a) Entrainment parameter \mathcal{E} and (b) salt flux F_S in $\text{kg m}^{-2} \text{s}^{-1}$ as a function of the gravity current length ℓ in Nek5000 experiments with four different bottom slopes. The dotted lines in (a) mark the values of \mathcal{E} corresponding to $\theta = 1^\circ$ and $\theta = 4^\circ$ in the formula $\mathcal{E} = 10^{-3} \times (5 + \theta)$ of Turner (1986).

Table 3.2: Values of E_0 in experiment sets A, B, C, and D.

#	Exp. A ($Ri_c = 0.75$)	Exp. B ($Ri_c = 0.50$)	Exp. C ($Ri_c = 0.35$)	Exp. D ($Ri_c = 0.25$)
1	0.0025	0.0025	0.0025	0.01
2	0.01	0.01	0.01	0.04
3	0.02	0.02	0.03	0.08
4	0.03	0.04	0.05	0.12
5	0.04	0.06	0.08	0.20
6	0.06	0.08	0.12	1.00

1986). Intermediate values of $Ri_c = 0.50$ and $Ri_c = 0.35$ are included to increase the information content. The chosen values of E_0 are based on the experience acquired when comparing the HYCOM experiments to the Nek5000 simulations.

For each experiment, the entrainment parameter $\mathcal{E}(\ell)$ and the salt flux $F_S(\ell)$ are calculated from the HYCOM simulations and compared to the results from Nek5000 as described in section 3.3. Considering the large number of parameter combinations, the comparison is conducted for $\theta = 1^\circ$ only. An optimal parameterization function derived from these comparisons is then tested for all slopes of 1° , 2° , 3° , and 4° , with results presented in section 3.5.

a) Exp. A: $Ri_c = 0.75$

Fig. 3.5 summarizes the results of the experiment set A. The parameterization functions with varying E_0 are plotted together with the original TP function (i.e., Eq. 2.9) for comparison (Fig. 3.5a). The criterion for a good entrainment parameterization is that it should be able to capture the evolution of \mathcal{E} along ℓ for different slope angles. In order to account for experimental design errors, we somewhat arbitrarily state that the results will be acceptable as long as they are within a $\pm 20\%$ tolerance band (Fig. 3.5b). 20% is also the range of variability shown by Nek5000 when the slope is varied by 1° (Fig. 3.4a). The evolution of $\mathcal{E}(\ell)$ in Exp. A for the different values of E_0 differs in HYCOM when

compared to Nek5000. First, the entrainment occurs earlier in HYCOM. This is because some time and distance are required for the plume in Nek5000 to develop turbulence and entrainment, while such a development process is not present in HYCOM. Second, $\mathcal{E}(\ell)$ in Nek5000 reaches a maximum value of about 0.013 shortly after the plume passes X_0 , and decays throughout time thereafter. In HYCOM, $\mathcal{E}(\ell)$ either attains an equilibrium state and does not decay (A1 to A3), or else it reaches a maximum comparable to Nek5000 but then decays more slowly (A4 to A6). Hence, none of these six parameterizations results in a satisfactory evolution of $\mathcal{E}(\ell)$.

In Exp. A, HYCOM and Nek5000 behave more similarly in terms of $F_S(\ell)$ than shown for $\mathcal{E}(\ell)$, both showing small variations in $F_S(\ell)$ after the initial transients (Fig. 3.5c). This is not surprising since the boundary forcing largely determines the salt flux. The variation of F_S from run A1 to A6 suggests that a stronger entrainment leads to a slightly weaker salt flux.

Since the entrainment rate E is parameterized as a function of the Richardson number Ri , the actual value of Ri in the simulated gravity currents is an important diagnostic of the entrainment process. In HYCOM, the Richardson numbers are defined at the center of each layer (i.e., Eq. 2.11). Fig. 3.5d shows the $Ri(t)$ of layer 3 at $x = X_0$ in HYCOM. Layer 3 is the most upper layer within the plume and the location of the most vigorous mixing. Ri is small when the head of the plume passes X_0 and increases quickly due to the strong entrainment, then decreases and finally settles at some level ranging from 0.1 to 0.6, depending on the strength of the entrainment. Stronger entrainment results in larger Ri because the entrainment reduces the velocity shear and increases the plume thickness, two factors that tend to increase Ri . Changes in Ri in turn affect the entrainment through the inverse proportionality of E to Ri in (3.11). The time-averaged Ri ($t > 6000$ sec) is

marked by circles in Fig. 3.5a, which indicates that, for different E_0 , different parts of $f(Ri)$ are active in determining the strength of the entrainment \mathcal{E} . As a result, the increase in \mathcal{E} becomes progressively smaller as E_0 becomes large although an increase in E_0 simply results in a corresponding increase in \mathcal{E} . This tendency is more pronounced in experiment sets B, C, and D than it is in A.

b) *Exp. B: $Ri_c = 0.50$*

Results of experiment set B are depicted in Fig. 3.6, similar to Fig. 3.5. The prescribed entrainment functions E of B1 to B6 are shown with the original TP in Fig. 3.6a. As in Exp. A, none of these 6 experiments is able to capture the evolution of \mathcal{E} along ℓ , although some improvement is shown in runs B5 and B6 (Fig. 3.6b). The F_S in the runs of Exp. B also show slight improvement over Exp. A (Fig. 3.6c). Stronger entrainment causes the Ri to be larger (Fig. 3.6d), and since E decreases faster with increasing Ri in Exp. B than in A, the feedback of Ri onto the entrainment becomes more significant.

c) *Exp. C: $Ri_c = 0.35$*

We further reduce the Ri_c to 0.35 in experiment set C (Fig. 3.7). Even though E_0 spans a large range, \mathcal{E} becomes close to the $\pm 20\%$ tolerance band later in time. Experiments C5 and C6 also show good matches in the entrainment maximum, thus improving the overall evolution of $\mathcal{E}(\ell)$. Corresponding to smaller variations in \mathcal{E} , the variations in F_S and Ri are also reduced. All 6 runs produce excellent matches in $F_S(\ell)$ to Nek5000. The narrow variability range of Ri can be explained by invoking the steady state momentum balance of gravity currents. The buoyancy forcing is balanced by bottom and entrainment stress. For the latter to be significant, Ri must be in a range where $E(Ri)$ is large enough to allow for a momentum balance. Hence, upon the change of $E(Ri)$ to a steeper function with shorter range in Ri from Exp. A and B to C, the simulated Ri settles into a narrower range.

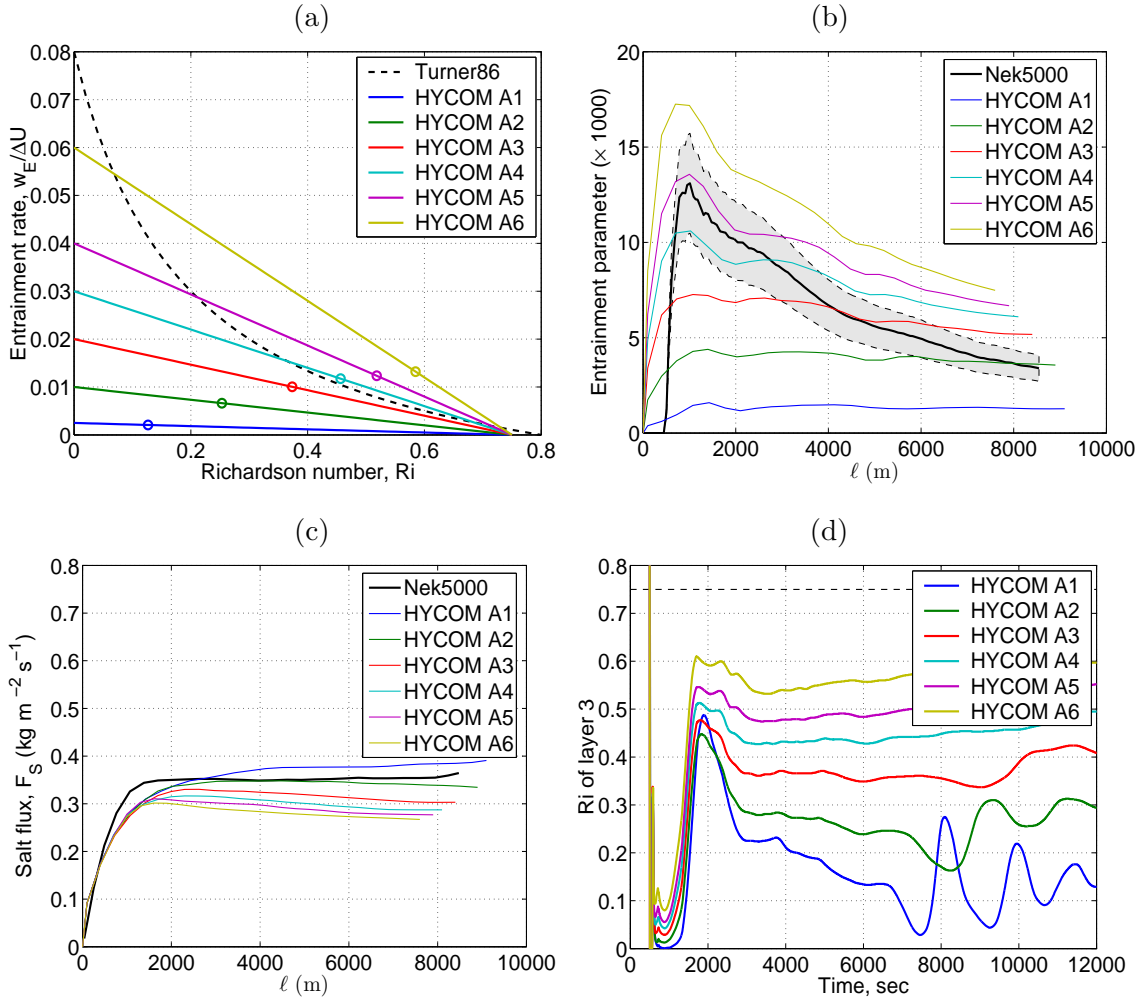


Figure 3.5: Results from Exp. A, $Ri_c = 0.75$. (a) Entrainment rate E as linear functions of Ri in experiments A1 to A6. The dash line is Turner's (1986) formula (2.9). The time-averaged Ri of layer 3 is marked as "o". (b) Entrainment parameter $\mathcal{E}(\ell)$ from Nek5000 and HYCOM. The shaded area represents a $\pm 20\%$ variance around Nek5000 results. (c) Salt flux $F_S(\ell)$ in $\text{kg m}^{-2} \text{s}^{-1}$ from HYCOM in comparison to Nek5000. (d) Richardson number $Ri(t)$ of layer 3 at $x = X_0$ from HYCOM experiments, with the dash line marks Ri_c .

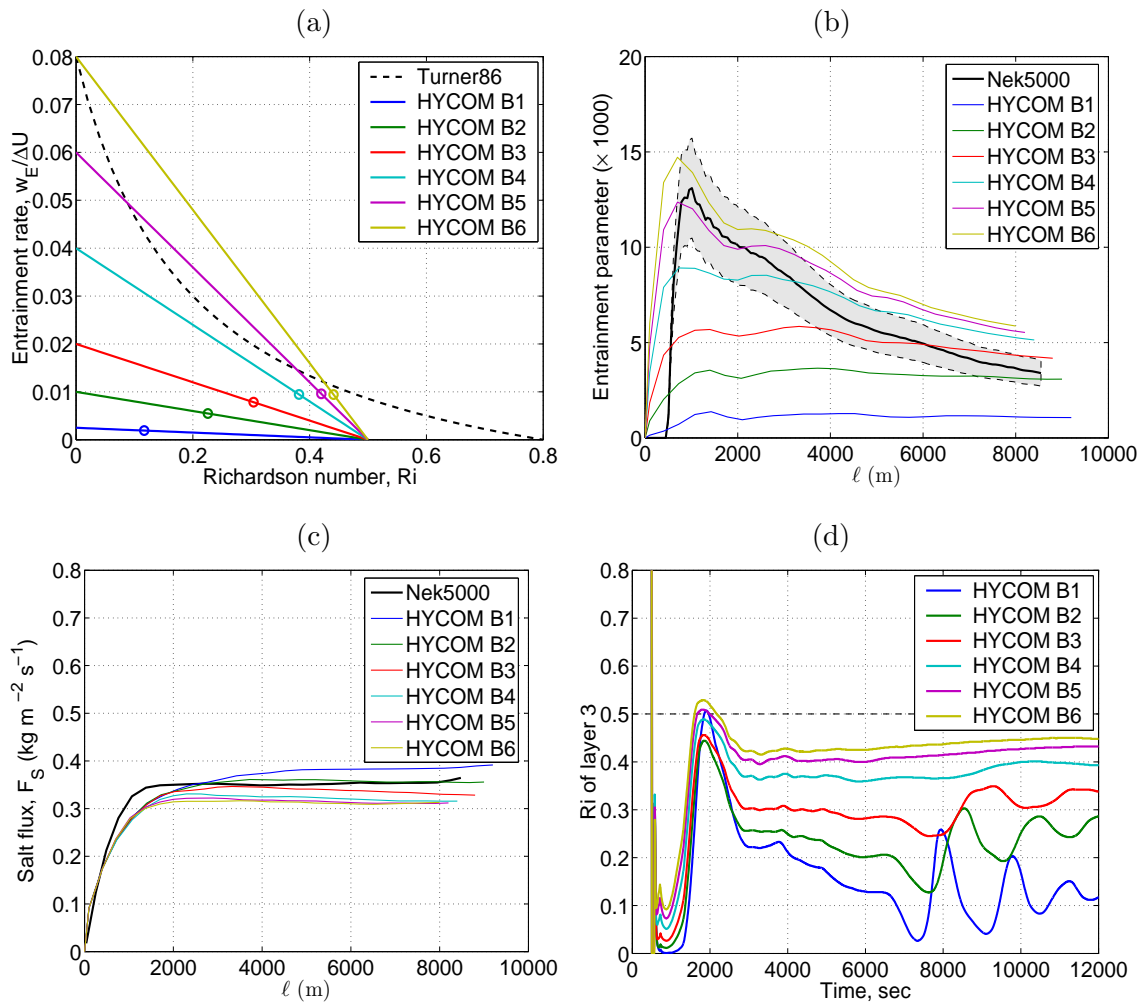


Figure 3.6: The same as in Figure 3.5 but for Exp. B, $Ri_c = 0.50$.

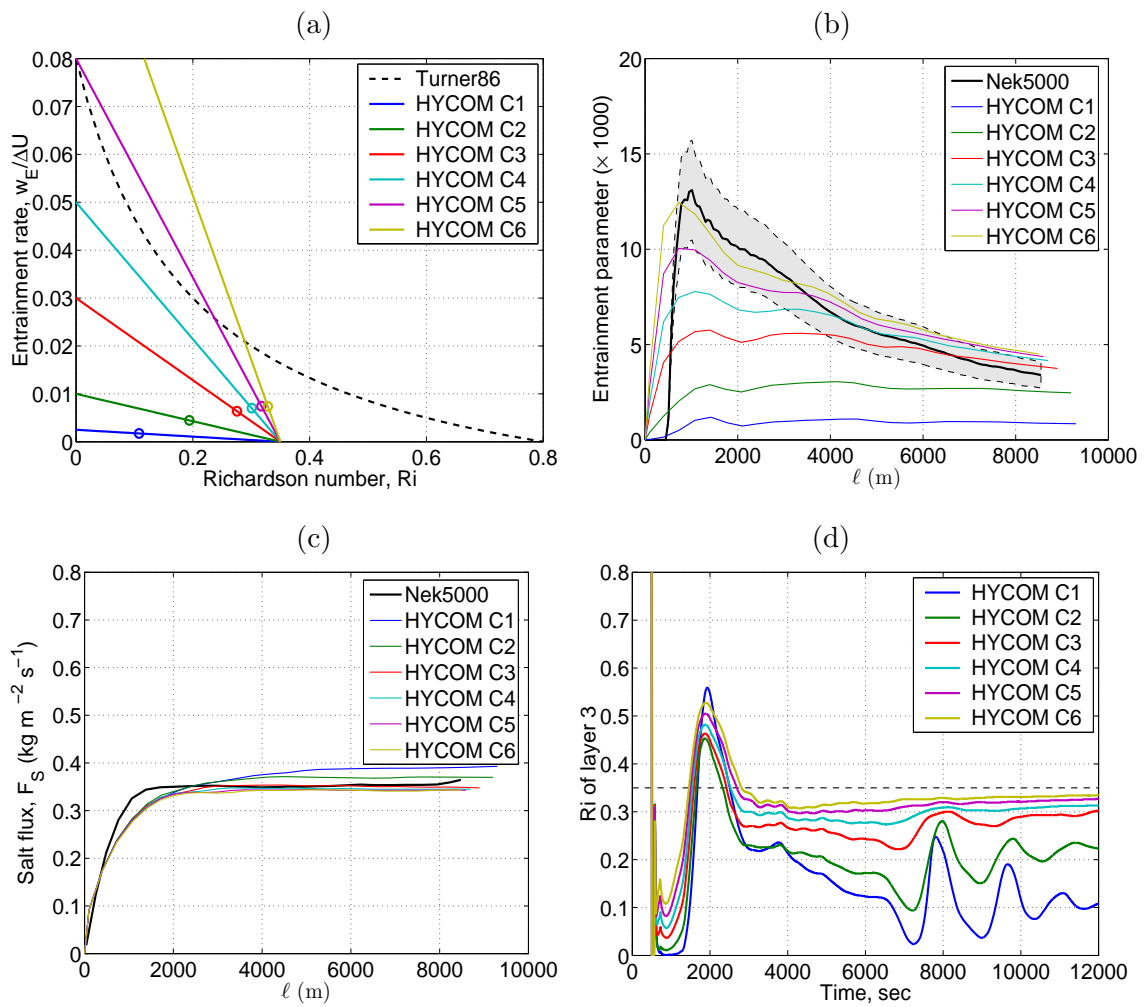


Figure 3.7: The same as in Figure 3.5 but for Exp. C, $Ri_c = 0.35$.

d) Exp. D: $Ri_c = 0.25$

Results of experiment D with $Ri_c = 0.25$ and E_0 of $0.01 \sim 1.0$ are illustrated in Fig. 3.8. As expected following the trend from Exp. A to C, the variability ranges of $\mathcal{E}(\ell)$, $F_S(\ell)$ and $Ri(t)$ become even smaller. The $\mathcal{E}(\ell)$ of experiments D2 to D6 closely follow the Nek5000 result when $\ell > 6000$ m (Fig. 3.8b). Meanwhile, runs D5 and D6 also reproduce an \mathcal{E} maximum comparable to that of Nek5000, and thus match the time-dependent behavior of the corresponding Nek5000 runs better than the previous three sets. The $F_S(\ell)$ of the 6 runs in Exp. D are nearly identical, and the steep curve in $E(Ri)$ forces the flow into a narrow range $Ri(t) \approx Ri_c$ for the same reason as discussed above.

e) Optimal values of Ri_c and E_0 in linear parameterization $E = f(Ri)$

By experimenting with various combinations of the cut-off Richardson number Ri_c and the “amplitude” parameter E_0 , we have found that the linear function $E = f(Ri)$ from experiments D5 and D6 produces in HYCOM the best match to Nek5000 in terms of \mathcal{E} as a function of ℓ . This simple parameterization states that there is no entrainment until Ri decreases below a critical value of about 0.25, and the entrainment increases linearly with decreasing Ri . $Ri_c \approx 0.25$ is consistent with our physical understanding of mixing, in that the turbulence in stratified shear flows is suppressed for $Ri > 1/4$ and grows for $Ri < 1/4$ (e.g., Miles, 1961; Rohr et al., 1988).

A physical upper limit for entrainment is $E_0 = 1.0$, which means that the maximum entrainment velocity w_E becomes the velocity difference ΔU itself. From experiment set D, we also observe that the evolution of $\mathcal{E}(\ell)$ is insensitive to E_0 as long as it is relatively large. This is because, when mixing takes place, the strength of the mixing is such that keeps Ri close to its critical value. Different formulas other than a linear one have been tested as well. It appears that the most important feature on the parameterization is the

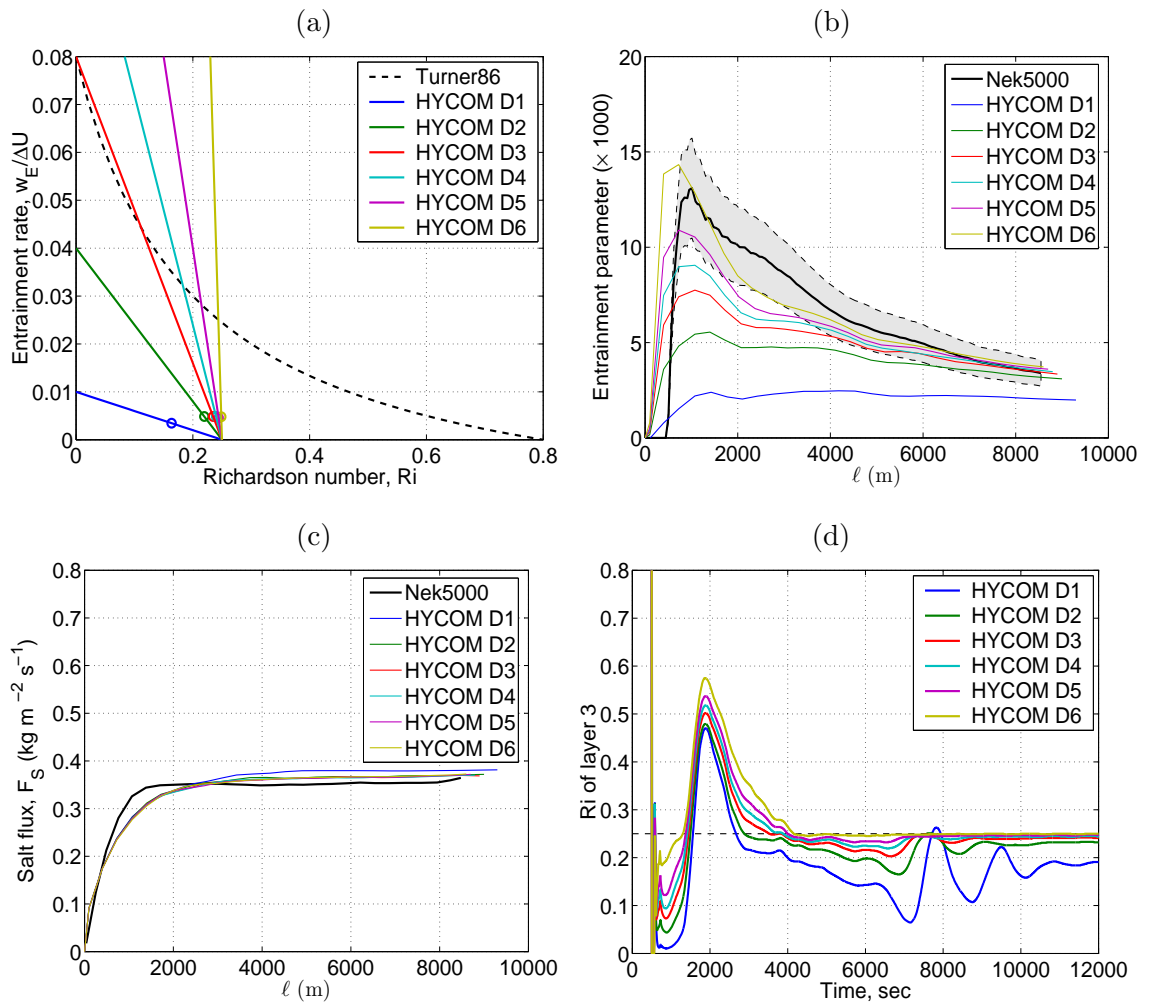


Figure 3.8: The same as in Figure 3.5 but for Exp. D, $Ri_c = 0.25$.

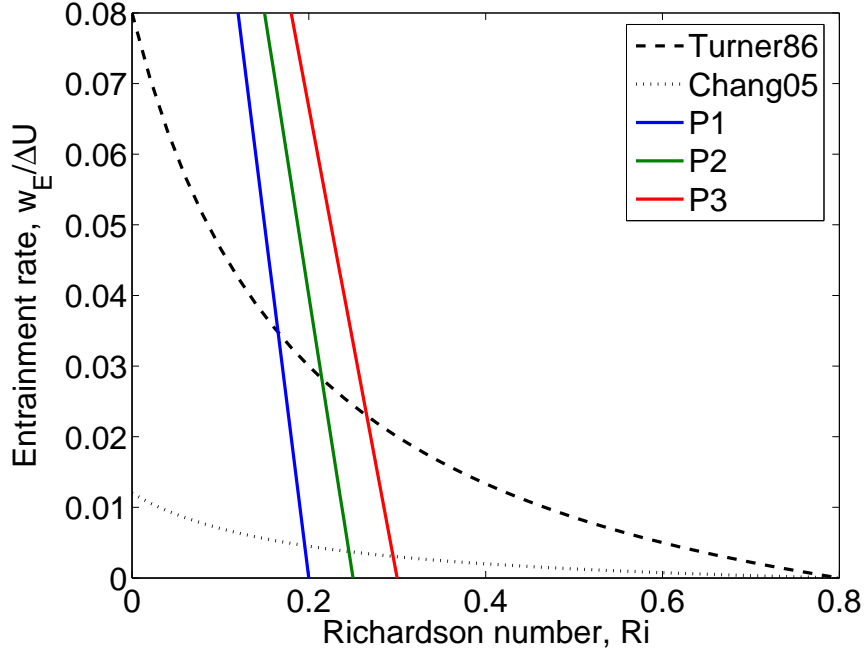


Figure 3.9: Entrainment rate $E \equiv w_E/\Delta U$ as function of Richardson number Ri . The solid blue, green and red lines are linear function Eq. (3.11) with parameters $E_0 = 0.20$ and $Ri_c = 0.20, 0.25$ and 0.30 ; the dash and dot black lines are the original TP and parameterization function of Chang et al. (2005) with $C_A = 0.15$, respectively.

increase of entrainment when Ri becomes close to 0.25. Hence, we simply set $E_0 = 0.20$ and $Ri_c = 0.25$ as the optimal values for entrainment parameterization (3.11). A variation of ± 0.05 is applied to $Ri_c = 0.25$ to investigate the sensitivity of entrainment to the specific values of Ri_c . We denote these parameterizations P1, P2, and P3 hereafter, for $E_0 = 0.20$ and $Ri_c = 0.20, 0.25$, and 0.30 , respectively (Fig. 3.9).

3.5 Detailed comparison between HYCOM with optimal $f(Ri)$ and Nek5000

The next stage is to investigate whether our optimal parameterization produces reasonable results in response to varying slopes. Therefore, we conduct the comparison for all 4 slope angles: $\theta = 1^\circ, 2^\circ, 3^\circ$, and 4° . Before giving quantitative details, we first present a

visual comparison between Nek5000 and HYCOM with entrainment scheme P2. Fig. 3.10 shows salinity anomaly snapshots of the simulated gravity currents approaching the lower end of the model domain in Nek5000 ($x = 10$ km). In Nek5000, fine-scale turbulent structures become more pronounced with increasing θ . This is not the case in HYCOM with P2 because none of the turbulence is resolved. For the same reason, the gravity current in Nek5000 has a more pronounced head, a non-hydrostatic feature that is not entirely reproduced in HYCOM. While there are naturally some differences between the Nek5000 and HYCOM results, our simple parameterization appears to allow fairly realistic gravity current simulations in HYCOM.

a) Entrainment parameter $\mathcal{E}(\ell)$

Fig. 3.11 depicts $\mathcal{E}(\ell)$ from the Nek5000 and HYCOM simulations for a slope angle θ of 1° to 4° . The five curves in the figure for HYCOM correspond to the following entrainment schemes: TP by Hallberg (2000), Chang et al. (2005), P1, P2, and P3 (see Fig. 3.9), respectively. The original TP actually reproduces the high entrainment maximum quite well, but overestimates the entrainment rate as the plume develops further in time (similar to A5). Multiplication of the right hand side of Eq. (2.9) by a factor of 0.15 as in Chang et al. (2005) leads to an entrainment that is flat along ℓ with no decay. This behavior is similar to that of A2. Our optimal formula shows a satisfactory match in $\mathcal{E}(\ell)$ to Nek5000 for all four configurations. Fig. 3.11 also suggests that $\mathcal{E}(\ell)$ is sensitive to the change in Ri_c .

b) Salt flux $F_S(\ell)$ and Richardson number $Ri(t)$

The salt flux F_S in the HYCOM results using P1, P2, and P3 compares well with that from Nek5000 (Fig. 3.12). The excess entrainment stress of the original TP slows down the plume and decreases F_S for all 4 slope angles, while the lack of entrainment in Chang et al. (2005) leads to slightly larger F_S especially for large θ .

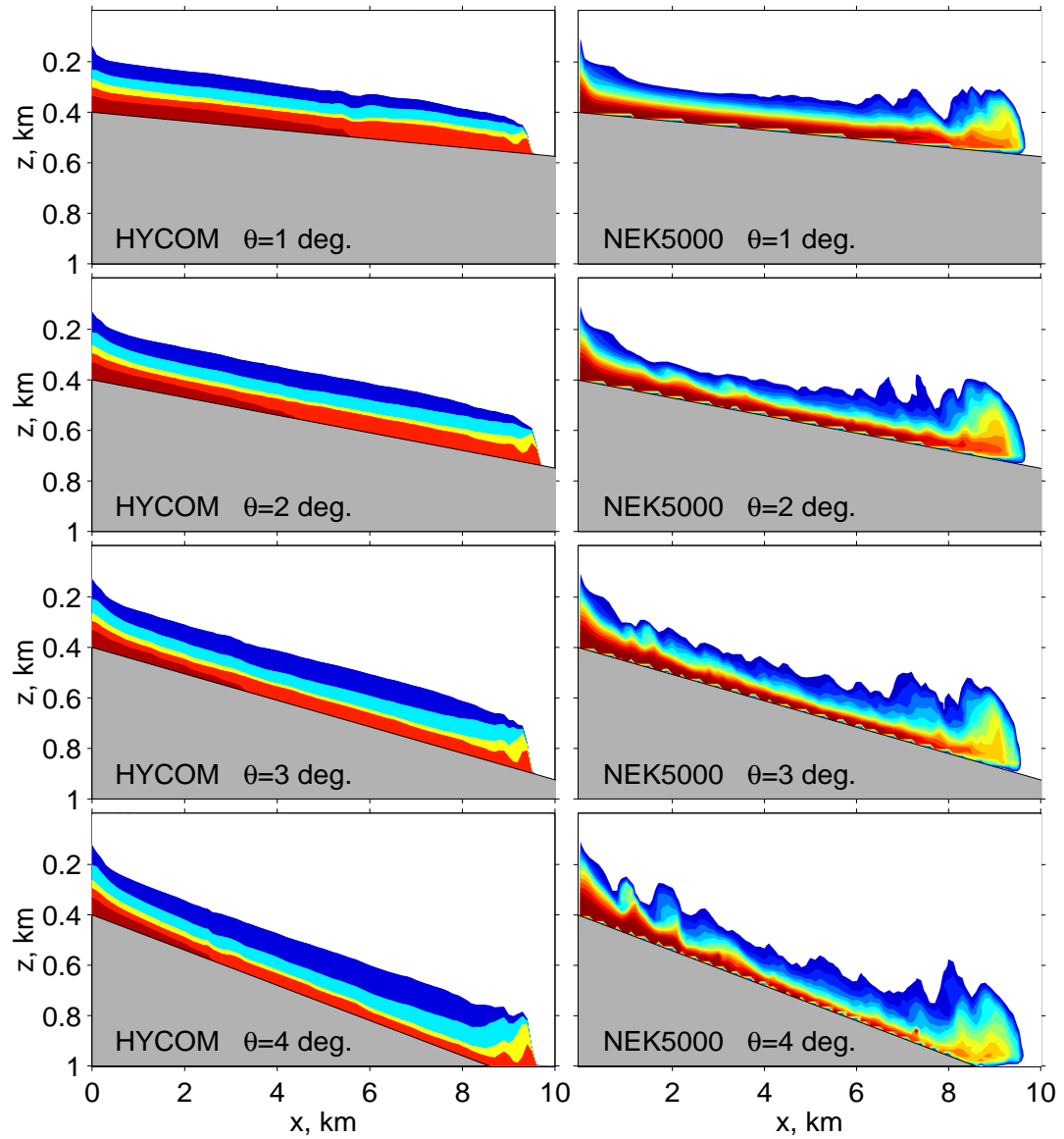


Figure 3.10: Salinity snapshots when the gravity currents plume approaches the lower end of domain; HYCOM using P2 (left) and Nek5000 (right) with different bottom slopes ($1 \sim 4^\circ$).

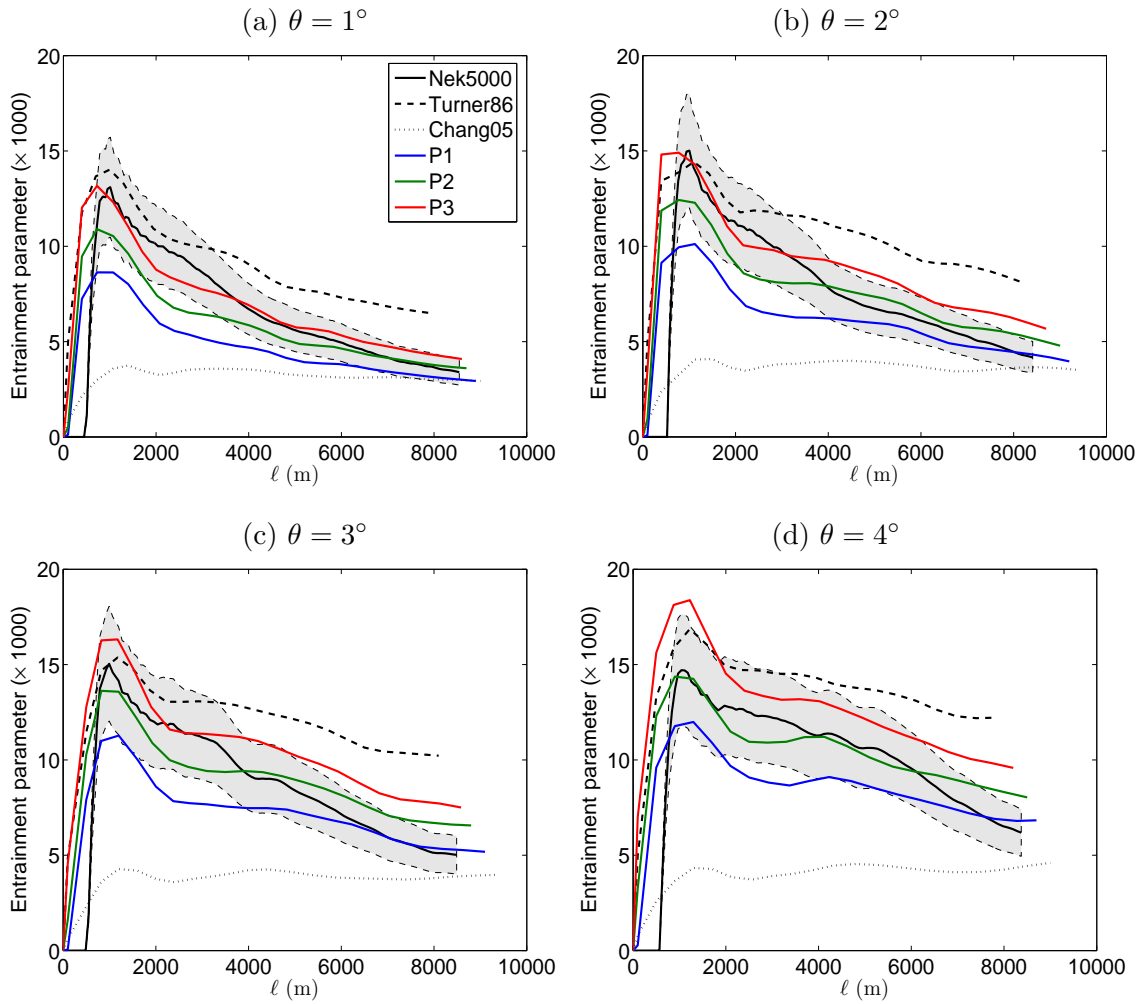


Figure 3.11: Entrainment parameter $\mathcal{E}(\ell)$ from Nek5000 and HYCOM experiments with different bottom slopes. The Nek5000 results appears with shaded $\pm 20\%$ variance; five entrainment schemes in HYCOM are Turner (1986), Chang et al. (2005), P1, P2, and P3, respectively.

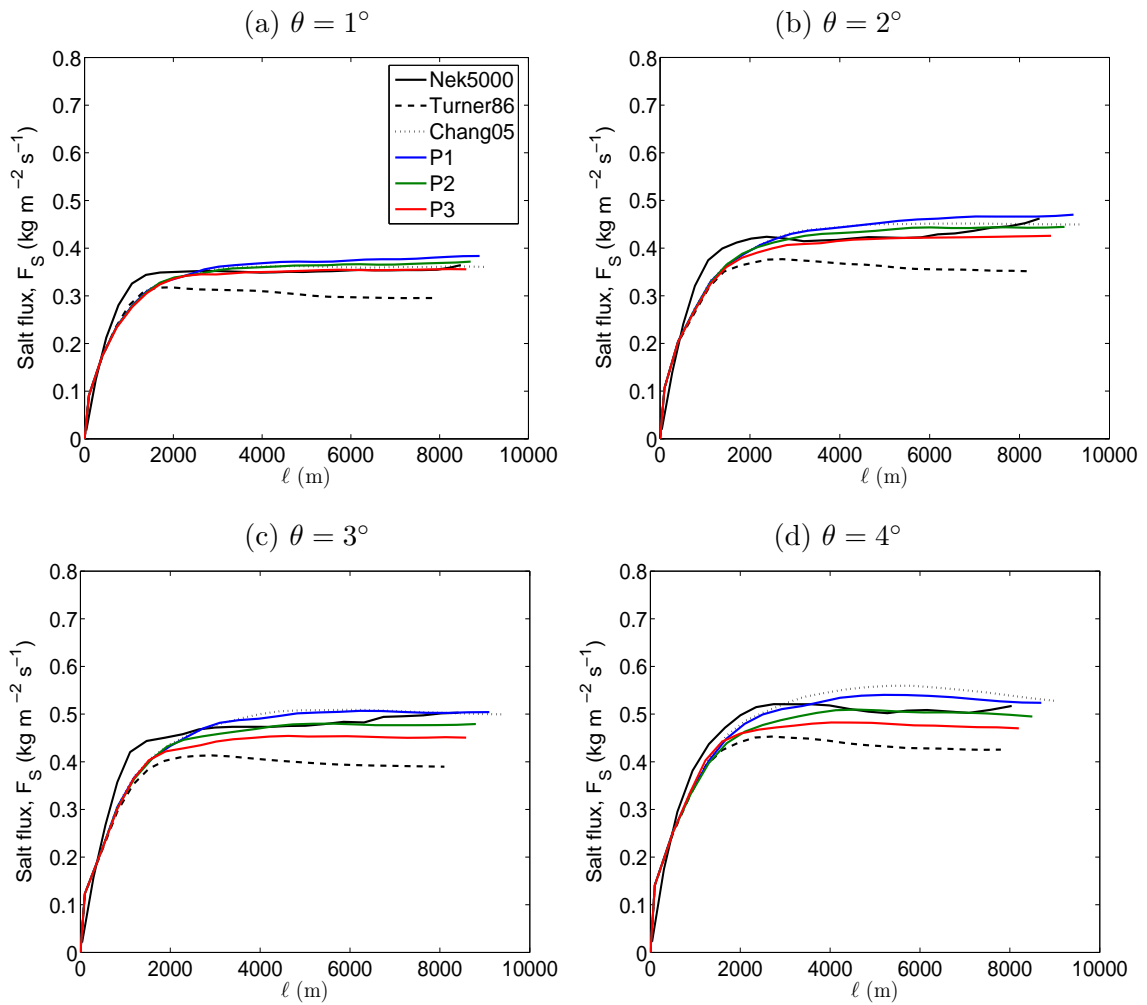


Figure 3.12: Salt flux $F_S(\ell)$ from Nek5000 and HYCOM experiments with different bottom slopes.

For configurations with increasing θ , the $Ri(t)$ show very similar evolution patterns, but decrease slightly (Fig. 3.13). This partly contributes to the increase in entrainment as seen in Fig. 3.11. As expected, the $Ri(t)$ of P1, P2, and P3 finally settle at levels close to the corresponding Ri_c of 0.20, 0.25, and 0.30. In contrast, the original TP and Chang et al. (2005) operate over a larger range of Ri . Therefore, the time evolution of Ri at the interface between the gravity current and the ambient water appears to be a characteristic feature of different parameterizations. Based on the spanwise-averaged velocity and salinity anomaly profiles taken at $x = X_0$, we calculated $Ri(t)$ from Nek5000 in an experiment with $\theta = 1^\circ$ (Fig. 3.14). The 5 selected depths are within the high shear interface where the most intense mixing takes place. These values of $Ri(t)$ are thus comparable to those of layer 3 in HYCOM (Fig. 3.13a). The comparison shows that $Ri(t)$ in Nek5000 and in HYCOM with entrainment scheme P2 are in reasonable agreement in terms of both magnitude and time evolution, providing further support for the parameterization.

c) Velocity profile $U(z)$ and plume propagation speed

In addition to the fundamental differences in model formulation, Nek5000 and HYCOM differ in the treatment the bottom stress. Due to the high spatial resolution, the bottom boundary layer is naturally resolved in Nek5000. In HYCOM an empirical quadratic drag law is applied in the lowest 10 m with a constant drag coefficient C_D . In a sensitivity test in HYCOM with P2, C_D is varied by two orders of magnitude (from 0.1×10^{-3} to 10×10^{-3}). Fig. 3.15 shows two time-averaged vertical profiles of zonal velocity at $x = 3$ and 5 km in experiments with $\theta = 1^\circ$ and 4° . The comparison suggests that, except for $C_D = 0.1 \times 10^{-3}$, HYCOM with the quadratic drag scheme works fairly well in reproducing the velocity profiles from Nek5000, and the results are sensitive to C_D only very near the bottom. $C_D = 3.0 \times 10^{-3}$ overall simulates the velocity maximum best. Our primary

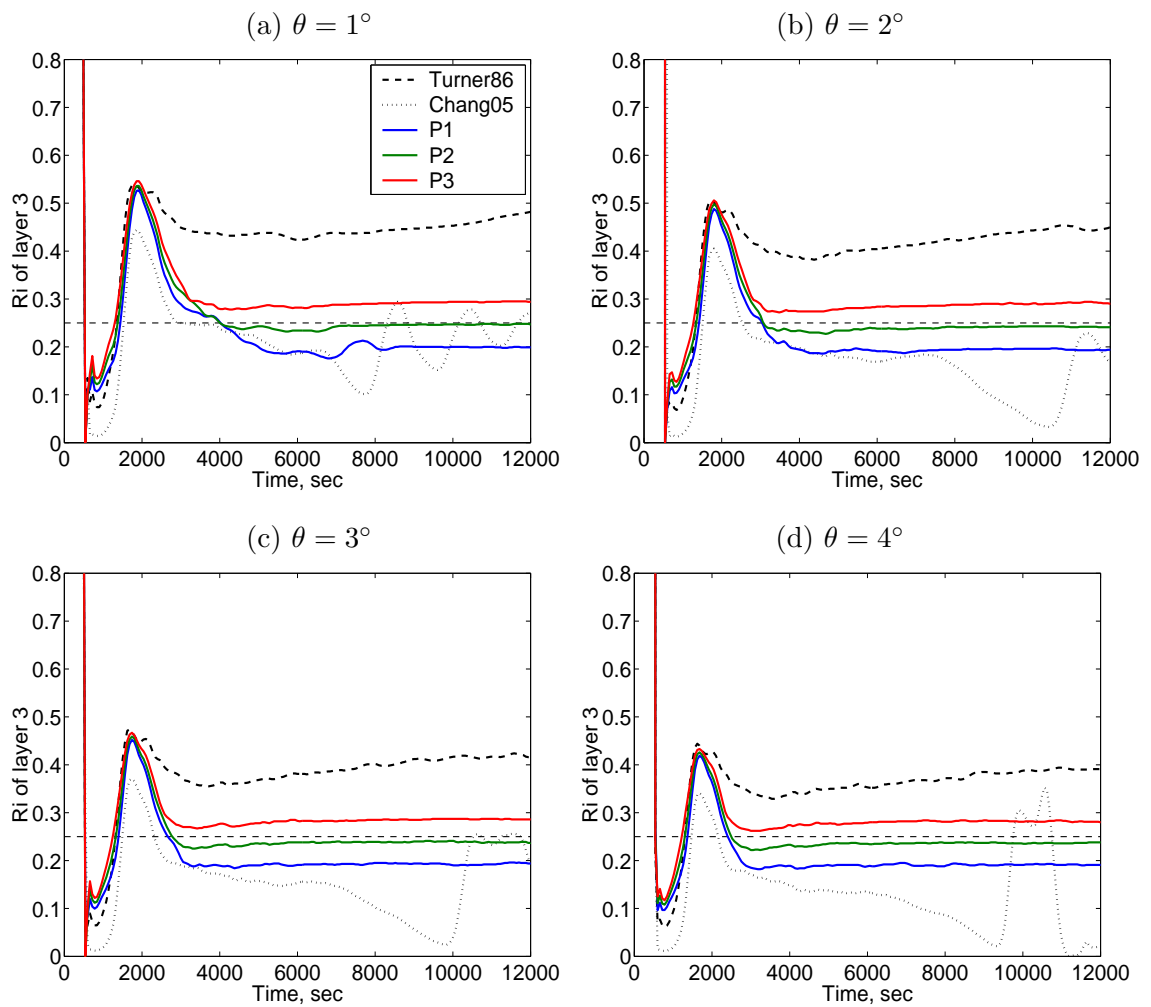


Figure 3.13: Richardson numbers $Ri(t)$ of layer 3 at $x = X_0$ from HYCOM experiments with different bottom slopes. The dash line marks $Ri = 0.25$.

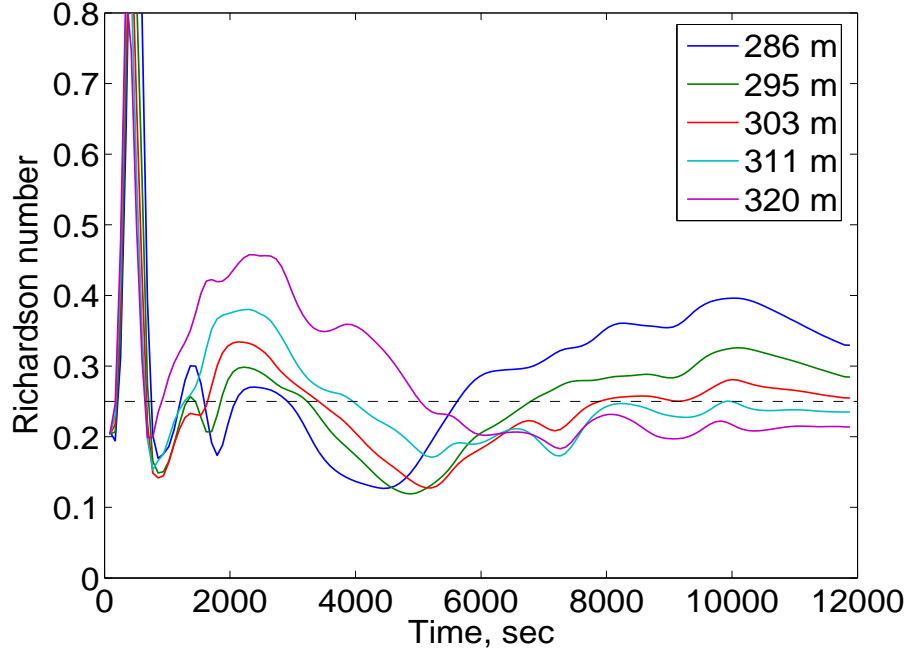


Figure 3.14: Richardson numbers $Ri(t)$ at different depths at $x = X_0$ from Nek5000 experiment with $\theta = 1^\circ$. The dash line marks $Ri = 0.25$.

concern is to have a comparable propagation speed of the plume in all experiments, since ℓ directly affects the calculation of \mathcal{E} and F_S . Fig. 3.16 suggests that for all 4 configurations, $C_D = 10 \times 10^{-3}$ shows the best match for $\ell(t)$ to the Nek5000 results, and this value has therefore been chosen for all the experiments discussed previously. The plume propagation speed is however not very sensitive to the value of C_D . With two orders of variation in C_D , $\ell(t)$ changes only approximately 10% for $\theta = 1^\circ$, even less for $\theta > 2^\circ$.

In summary, with a simple linear parameterization, HYCOM is shown to reproduce qualitatively the salinity anomaly distribution, and quantitatively the evolutions of entrainment $\mathcal{E}(\ell)$ (Fig. 3.11), salt flux $F_S(\ell)$ (Fig. 3.12), Richardson number $Ri(t)$ (Fig. 3.14), velocity profile (Fig. 3.15), and propagation speed (Fig. 3.16) of the bottom gravity current flow down different slope angles, as in the results of Nek5000.

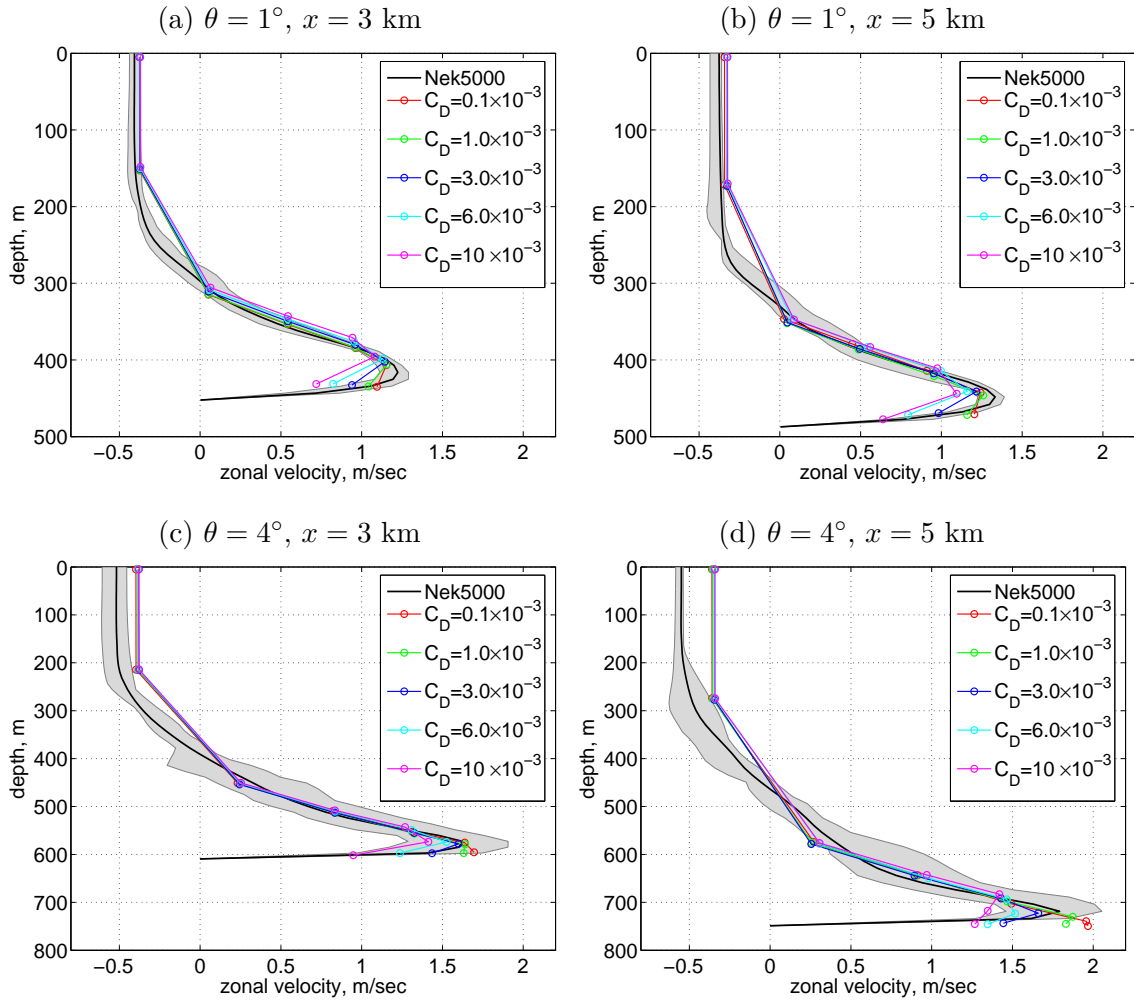


Figure 3.15: Zonal velocity profiles at station $x = 3 \text{ km}$ (left panels) and $x = 5 \text{ km}$ (right panels) from Nek5000 and HYCOM with linear entrainment scheme P2. The black line is the mean profile from Nek5000 with shading area representing the time variation; five different C_D s are tested in HYCOM, with center of each layer marked as “o”. The upper and lower panels are 1° and 4° slope configuration, respectively.

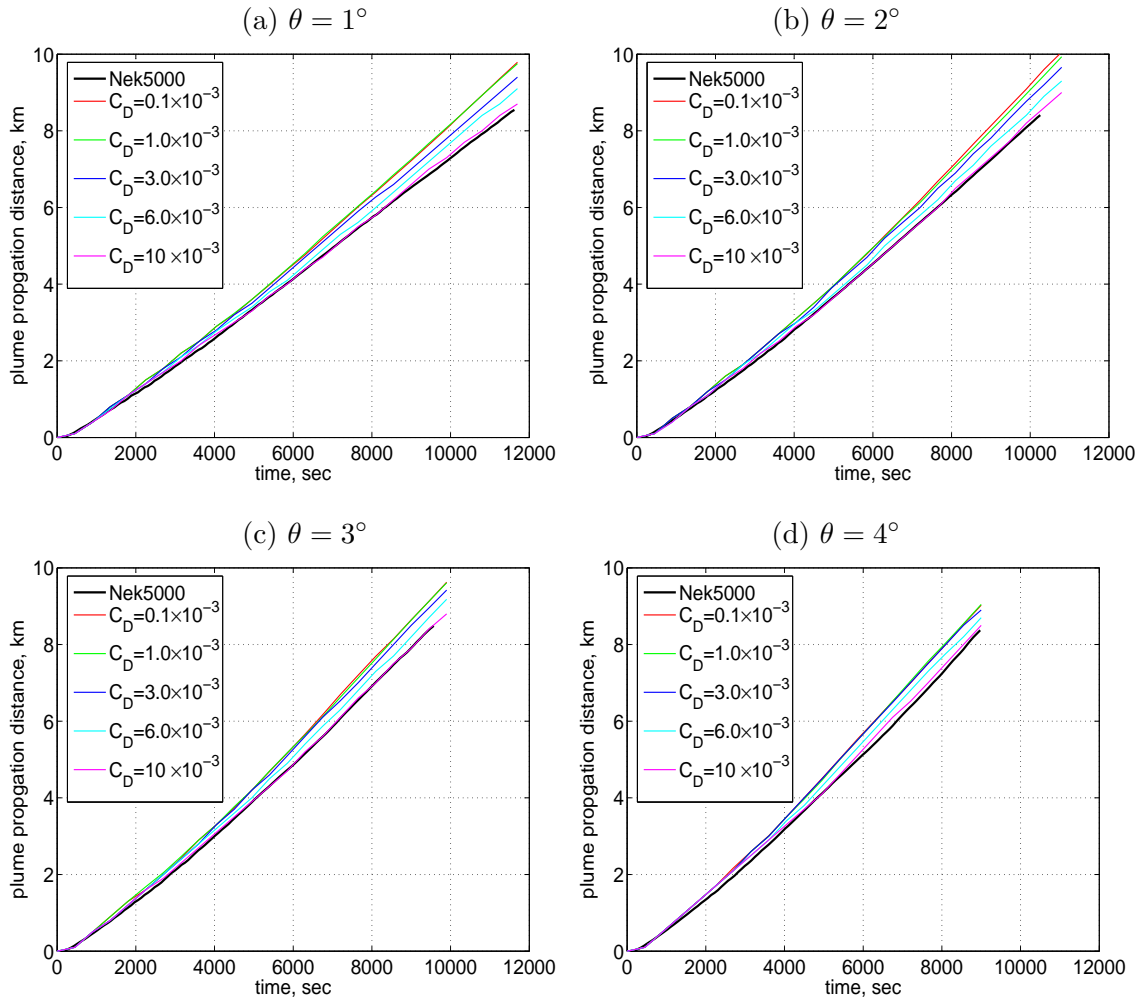


Figure 3.16: The plume propagation distance ℓ vs. time from Nek5000 and HYCOM experiments with different bottom slopes. HYCOM is run with the linear entrainment scheme P2 and five bottom drag coefficients C_D .

3.6 Summary and discussion

In light of the pressing need for reliable and physically-based parameterizations of mixing of outflows with ambient water masses in OGCMs, a new algebraic parameterization for isopycnic coordinate models has been derived based on the work by Turner (1986) and Hallberg (2000). The parameterization casts the entrainment velocity as a function of the Richardson number (Ri) times the velocity difference across layers, incorporating a dependence on the forcing. This formulation is consistent with Buckingham's Pi-Theorem (e.g., Kundu, 1990, Dynamic Similarity), which states that constants in a physical law should be dimensionless, and with the physical requirement that the interfacial shear is the dominant energy source for turbulent mixing in stratified flows.

To determine the function $f(Ri)$, we have compared simulated gravity currents flowing down various bottom slopes from the relatively low-resolution, hydrostatic model HYCOM to those from the high-resolution, nonhydrostatic spectral element model Nek5000, which served as ground truth. A linear function $E = E_0(1 - Ri/Ri_c)$, in which E_0 and Ri_c represent the entrainment magnitude and the cut-off Richardson number, is used in HYCOM with a 1° slope, and the results are quantified by an entrainment parameter $\mathcal{E}(\ell)$ and a salt flux $F_S(\ell)$. The comparison shows that $\mathcal{E}(\ell)$ is quite sensitive to the variations in E_0 and Ri_c , and that the best results are obtained for $E_0 = 0.20$ and $Ri_c = 0.25$. On the other hand, $F_S(\ell)$ is not very sensitive to changes in E_0 and Ri_c , and compares well to the Nek5000 in all simulations.

This simple, optimal, linear scheme is then applied in four configurations varying in bottom slope angle ($1^\circ \sim 4^\circ$). A detailed comparison of $\mathcal{E}(\ell)$, $F_S(\ell)$, $Ri(t)$, velocity profiles, and propagation speeds has been performed. The results suggest that HYCOM is able to reproduce the basic characteristics of the simulated gravity current from Nek5000 in

both qualitative and quantitative respects. In particular, this linear scheme reproduces the evolution of entrainment into a gravity current as a function of change in forcing better than the KPP and TP scheme do.

OGCMs used in large-scale circulation simulations, especially in climate studies, require simple yet physically-based parameterizations of mixing in general and especially of entrainment into gravity currents. The parameterization proposed herein, though radically simple, is consistent with the fundamental theoretical and laboratory results from stably-stratified shear flows: the shear-induced turbulence grows (decays) in the regime of $Ri < 0.25$ ($Ri > 0.25$). It thus appears to hold promise for realism and deserves a more detailed evaluation by comparing model results with observations in various outflow cases. A remaining issue that needs to be addressed is the dependence of the performance of the entrainment parameterization on the horizontal grid spacing. These questions will be investigated by carrying out a detailed comparison of model results with the observations of Baringer and Price (1997a,b) from the Mediterranean outflow.

Chapter 4

Simulation of the Mediterranean outflow in the Gulf of Cádiz

The aim of this chapter is to evaluate the performance of the algebraic parameterization developed in chapter 3 in simulating realistic oceanic outflows. In addition to its importance to water mass formation in the North Atlantic Ocean, two reasons lead us to choose the Mediterranean outflow as our test case. First, the Mediterranean outflow is one of the best-observed (e.g., Ambar and Howe, 1979a,b; Ochoa and Bray, 1991; Wesson and Gregg, 1994; Johnson et al., 1994; Johnson and Sanford, 1994; Baringer and Price, 1997a,b). Second, the Mediterranean outflow source water possesses a large density contrast with respect to the entrained ambient water, so that the modification of the outflow water properties is sensitive to the strength of the entrainment. The Mediterranean outflow source water is the densest water mass observed in the North Atlantic Ocean because of its high salinity. However, the product water equilibrates at an intermediate depth of about 1100 m. Therefore, the evolution of the Mediterranean outflow water provides an excellent test as to how accurate the entrainment is prescribed by the parameterization.

4.1 Introduction

The Mediterranean Sea is a semi-enclosed marginal basin in which strong evaporation exceeds the sum of precipitation and river runoff, thus transforming the relatively fresh North Atlantic surface water (salinity S of 36.1 psu) into the salty and dense Mediterranean water (S of 38.45 psu and potential density σ_θ of 28.95 kg m^{-3}). As this dense water mass exits the Strait of Gibraltar and spreads into the North Atlantic Ocean, it mixes with the surrounding waters, creating a warm and saline tongue of water at an intermediate depth of about 1100 m that can be traced throughout the entire subtropics (Levitus and Boyer, 1994). Moreover, the impact of the Mediterranean outflow water (MOW hereafter) extends well beyond the subtropics of the North Atlantic Ocean and the intermediate depth. Either through indirect or direct routes, the MOW is responsible for supplying salt to the near surface water that ultimately flows into the Nordic Seas and influences the deep water formation there (Reid, 1979, 1994; Iorga and Lozier, 1999a,b; McCartney and Mauritzen, 2001; Bower et al., 2002b). Therefore, studying the Mediterranean outflow is important for understanding not only the water properties and circulation in the subsurface of the eastern North Atlantic, but also the meridional overturning circulation in the entire Atlantic basin.

The circulation and evolution of the MOW begins as a bottom trapped gravity current flowing out the Strait of Gibraltar. This dense water plume descends the Iberian continental slope, on which dynamics such as the bottom topography, earth rotation, and bottom friction play a key role in controlling the plume pathway (Ochoa and Bray, 1991; Madelain, 1970; Zenk, 1975; Johnson et al., 1994; Johnson and Sanford, 1994; Price and Baringer, 1994). At the upper interface of the outflow plume, the entrainment of North Atlantic Central Water (NACW hereafter) increases the volume transport and consequently reduces the density contrast between the MOW and the ambient water (Ambar and Howe, 1979a,b;

Baringer and Price, 1997a,b; Price et al., 1993; Zenk and Armi, 1990). The outflow plume shows interesting spatial variations and multi-core features at about 7°W , as repeatedly reported (e.g., Zenk, 1970; Ambar and Howe, 1979a; Ambar, 1983; Ambar et al., 2002, etc.). The variations have usually been attributed to differential mixing with NACW (Baringer and Price, 1997a,b; Iorga and Lozier, 1999a). An important transition in plume behavior, from a bottom-trapped density current to a wall-bounded jet, the MOW undercurrent, occurs to the west of about 8°W , downstream from the point at which the plume becomes equilibrated in the water column and continues its travel at intermediate depths. Further downstream at Cape St. Vincent, the bottom topography abruptly changes direction, and the flow separation from the bottom slope promotes the generation of MOW anticyclonic vortices (meddies; McDowell and Rossby, 1978; Bower et al., 1997a). Beyond Cape St. Vincent, the undercurrent generally separates into two main branches flowing northward and westward (Daniault et al., 1994). However, the strength and destiny of these flows remain largely unknown, and these are at the heart of understanding the large scale impact of the MOW.

4.2 Observational data

The observational data used in this study are from the 1988 Gulf of Cádiz Expedition (Price et al., 1993). Drs. Dunlap and Sanford from the University of Washington have kindly provided the preprocessed data. More recently, there have been at least 4 observational surveys aimed at understanding various aspects of the vortices (or eddies) associated with the Mediterranean outflow undercurrent: the U.S funded program “A Mediterranean Undercurrent Seeding Experiment” (AMUSE; Hunt et al., 1998; Bower et al., 1997a,b, 2002a); the EU MAST III funded project “Canary Islands Azores Gibraltar Observations” (CANIGO;

Ambar et al., 2002); the Portuguese funded project “Mediterranean undercurrent - Eddies and Topographic Effects” (MEDTOP; Serra et al., 2005); and the French program “Sortie des Eaux Méditerranéennes en Atlantique Nord Est” (SEMANE; Chérubin et al., 2000). Compared to these surveys, the Gulf of Cádiz Expedition focuses on the descent and mixing of the Mediterranean outflow as it spreads into the Gulf of Cádiz, particularly the first 100 km of the path where the mixing was expected to be most intense. It therefore provides an excellent comparison truth for our numerical simulation. A number of papers describing results from this data set have been published (e.g. Baringer, 1993; Price et al., 1993; Johnson et al., 1994; Johnson and Sanford, 1994; Baringer and Price, 1997a,b, etc.).

The data to be discussed include 120 CTD profiles and 79 *in situ* horizontal current profiles gathered with the XCP (expendable current profiler). Fig. 4.1 shows the location of the stations. The CTD stations were laid out in 11 sections, labeled from A to K, with one section I running along the axis of the strait and the rest approximately normal to the outflow in the Gulf. The XCPs were obtained at sections A through F when a CTD cast indicated the presence of salty MOW. At some sites between section A and C, multiple drops are obtained at nearly the same location. All repeated profiles show remarkably similar velocity and density structures within the plume, implying a negligible tidal influence. The plume appears steady during the survey. For more details about this survey and the data calibration, the reader is referred to Baringer and Price (1997a) and the references therein.

Table 4.1: The reference densities $\hat{\sigma}_2$ (kg/m³) used in the Mediterranean outflow experiment.

k	1	2	3	4	5	6	7	8	9	10
$\hat{\sigma}_2$	23.50	26.00	27.75	29.25	30.50	31.75	32.95	34.01	34.91	35.45
k	11	12	13	14	15	16	17	18	19	20
$\hat{\sigma}_2$	35.80	36.04	36.20	36.38	36.52	36.62	36.70	36.77	36.83	36.89
k	21	22	23	24	25	26	27	28		
$\hat{\sigma}_2$	36.97	37.02	37.06	37.10	37.17	37.30	37.42	37.48		

4.3 Model configuration

A regional model is configured with horizontal resolution of 0.08° . The computational domain ($13.0 \sim 2.76^\circ\text{W}$, $34.2 \sim 40.8^\circ\text{N}$) includes the Northeast Atlantic Ocean, the Gulf of Cádiz, the Strait of Gibraltar, and a small part of the western Mediterranean Sea. There are 28 σ_2 layers in the vertical, with the reference densities listed in Table 4.1. The bottom topography is extracted from the North Atlantic simulation ‘ATLd0.08’. The model is initialized using the temperature and salinity fields from the climatology ‘Generalized Digital Environmental Model (GDEM3)’. With a process modeling perspective, no surface forcing is applied in this simulation, all boundaries are closed, and relaxation to climatology is applied at each boundary. For diapycnal mixing, the algebraic parameterization derived in Chapter 3 is used. The model starts from rest and is integrated for 6 months.

4.4 Results

4.4.1 Exchange through the Strait of Gibraltar

Unlike other numerical studies of the Mediterranean outflow (e.g., Jungclaus and Mellor, 2000; Papadakis et al., 2003), the model configuration used here includes the Strait of Gibraltar, thus dynamically modeling the exchange flow through the strait. The simulated vertical profiles of salinity and horizontal velocity near the Cardinal Sill (5.72°W , 39.1°N)

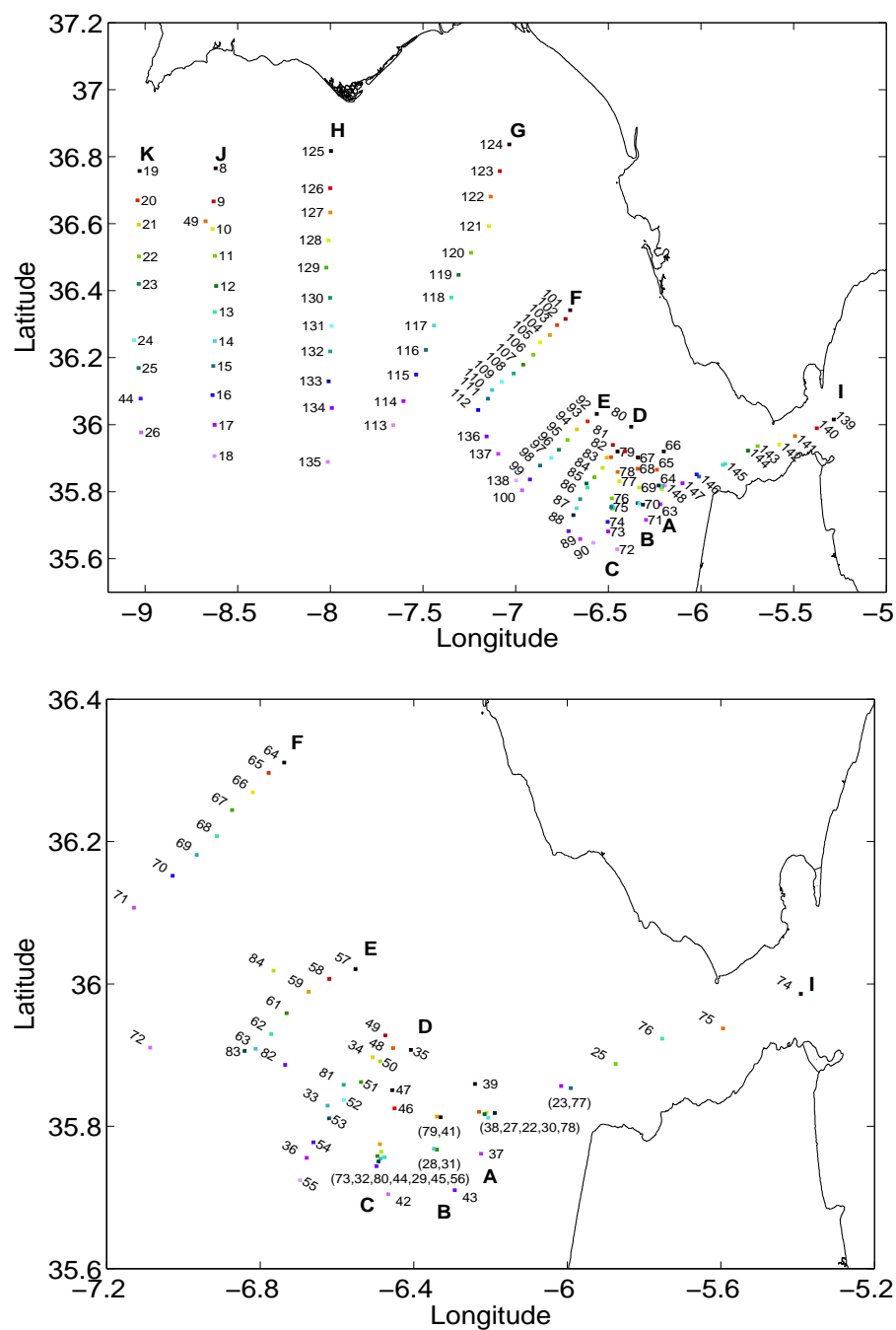


Figure 4.1: The locations of CTD (upper) and XCP (below) stations during the 1988 Gulf of Cádiz Expedition.

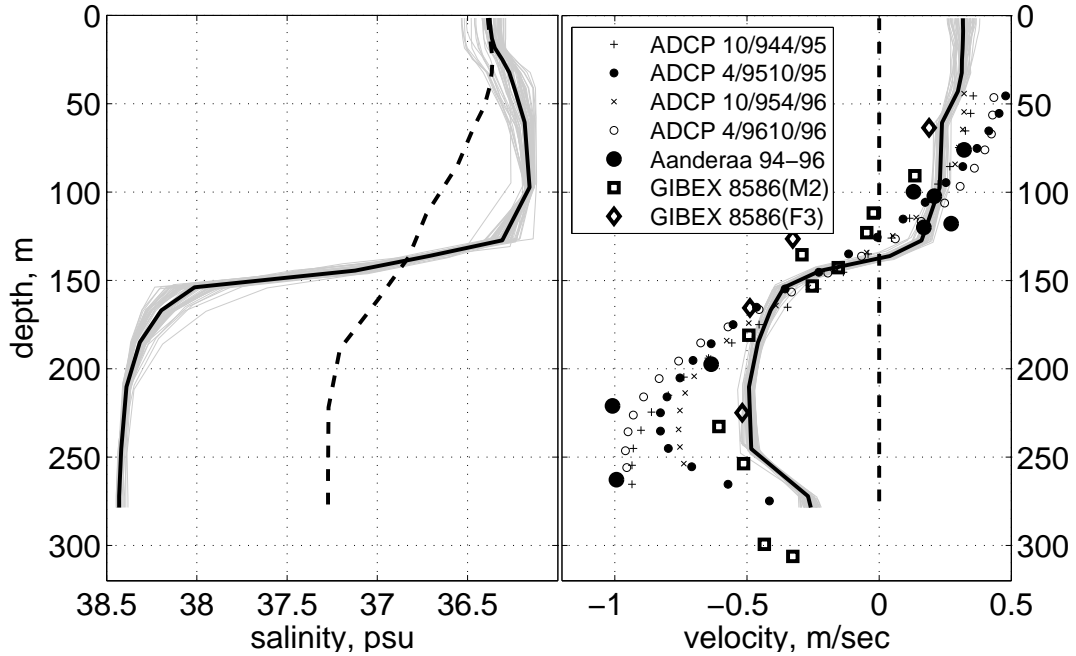


Figure 4.2: The simulated vertical profiles of salinity (left panel) and horizontal velocity (right panel) in the Strait of Gibraltar near the Cardinal Sill (5.72°W , 39.1°N). The thick dash lines are the initial profiles; the thin gray lines are simulated profiles in every 3 days; and the thick solid lines represent the time-averaged profile. The observed velocity profiles are reproduced from Fig. 5.7.5 of Candela (2001)

are shown in Fig. 4.2. The velocity profiles are plotted with observations obtained at close locations from the 1985-86 Gibraltar Experiment (GibEx85/86, Bryden et al., 1994) and from a more recent, two-year (Oct. 94 ~ Oct. 96) continuous observational program reported by Candela (2001). A steady two-layer exchange flow system is quickly reached, and both the salinity and velocity profiles remain nearly constant throughout the simulation. The simulated isohaline of 37.0 psu approximately marks the boundary between inflow and outflow, which have characteristic salinities of 36.2 and 38.45 psu, respectively. This agrees well with observations. The outflow velocity reaches 0.5 m s^{-1} , which is about the same magnitude as observed in GibEx85/86 but considerably weaker than the value (about 0.8 m s^{-1}) of Candela (2001).

The exchange through the strait more often is measured by a volume and/or salinity

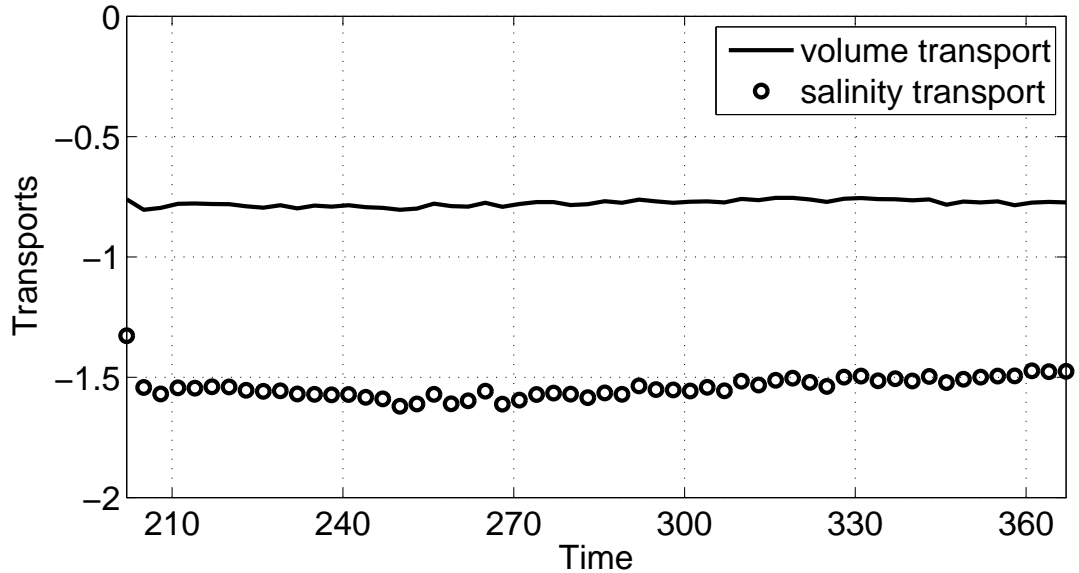


Figure 4.3: The simulated volume transport (in Sv) and salinity transport (in $10^3 \text{ m}^3 \text{ s}^{-1}$) of the Mediterranean outflow through the Strait of Gibraltar.

transport. A number of estimates using different methods have been reported (see Table 1 in Bryden et al., 1994). The volume transport based on evaporation and precipitation over the Mediterranean Sea ranges from 0.9 to 1.8 Sv ($1 \text{ Sv} = 10^6 \text{ m}^3 \text{ s}^{-1}$) (Hopkins, 1978), with the most widely quoted value being 1.2 Sv (Lacombe and Richez, 1982). Based on data from GibEx85/86, Bryden et al. (1994) estimate the volume and salinity transport of 0.7 Sv and $1.5 \times 10^3 \text{ m}^3 \text{ s}^{-1}$ ($1 \text{ Sv} \times 1 \text{ psu} = 1 \times 10^3 \text{ m}^3 \text{ s}^{-1}$), respectively. These were regarded as the most reliable estimates because of both their duration and their basis of direct current measurement. However, Candela (2001) estimates a higher volume transport of 1.0 Sv, consistent with the difference in observed outflow velocity. In addition, his observation shows for the first time an annual cycle of about 0.3 Sv. Our simulation does not show seasonal variability and has mean values of 0.76 Sv and $1.50 \times 10^3 \text{ m}^3 \text{ s}^{-1}$ (Fig. 4.3) for volume and salinity transport, respectively, in good agreement with the results of GibEx85/86.

4.4.2 Comparison of T/S profiles

Fig. 4.4 presents a direct comparison between the observed and simulated temperature and salinity profiles of all CTD stations shown in Fig. 4.1. The numerical results are linearly interpolated onto the location of each station and a time average (of the last 3 months of model simulation) is applied.

At sections A, B, and C, the outflow plume clearly shows a two-layer structure, a weakly stratified bottom layer and an interfacial layer. The bottom layer has a thickness of about 60 m and the maximum salinity decreases from 38.25 to 38.0 psu from section A to C. The interfacial layer, about 100 m thick, is sandwiched between the bottom layer and the NACW, which is characterized by a salinity minimum of < 36.0 psu. The simulation shows a similar two-layer structure. The maximum salinity at section A is about 0.5 psu less than observed, indicating that strong shear mixing has already taken place in the model. However, the simulated salinity maximum of sections A and B is found to be higher in shallower stations than in the deep ones, which is opposite to the observations. The outflow water is fresher in shallow areas possibly because the plume there is much thinner and thus can be diluted quickly. From the mixing point of view, one possible cause that can contribute to the model behavior is that the plume velocity is weaker in the shallower area, and thus the shear mixing is consequently weaker. It has to be mentioned, however, that the observed outflow plume at sections A and B spans less than 12 km (Baringer, 1993). Thus, the horizontal grid size used (~ 7 km) is still too large to resolve detail of the bottom bathymetry near the strait. The relatively large grid size also causes the simulated outflow to be significantly wider than in the observations.

Both the observations and the simulation show that the weakly-stratified bottom layer is mixed away since section D, while the outflow plume is still bottom trapped. The edge

stations sample the ocean water profile outside the observed outflow plume. Because the MOW is warmer and saltier than the ocean water at the same depth, the T/S profiles with the presence of MOW stand out from the profile of ocean water near the bottom. However, all stations in the simulation contain MOW, which indicates that the simulated outflow plume spreads wider than has been observed. At sections F and G, the simulation shows fresher MOW in the shallower area than in the deep, consistent with the observations. Farther west at section H (about 8°W), the MOW plume becomes detached from the ocean floor, and the plume continues its travel downstream at intermediate depths between 1000 and 1500 m.

The evolution of water properties of MOW in the Gulf of Cádiz is compared in the T-S diagram in Fig. 4.5. The outflow begins at σ_0 of $\sim 29 \text{ kg m}^{-3}$, and mixes with the NACW above as the plume spreads into the Gulf of Cádiz, substantially decreasing the salinity and thus the density. When the plume is equilibrated at intermediate depth after section H, the MOW has a σ_0 value of about $\sim 27.8 \text{ kg m}^{-3}$. The comparison shows that the simulation reproduces this evolution quite well.

4.4.3 Comparison of horizontal velocity profiles

Fig. 4.6 presents a direct comparison between the observed and simulated velocity profiles for all XCP stations shown in Fig. 4.1. The same linear interpolation and time averaging process as in the temperature and salinity profiles comparison is applied.

At section I, the observed velocity profiles contain much stronger variations than that in the simulation. The variations in the strait are mainly due to the tidal fluctuations, which are not included in our model configuration. The tidal effect becomes negligible after the plume exits the strait. As mentioned above, repeat XCP drops in section A, B, and C show

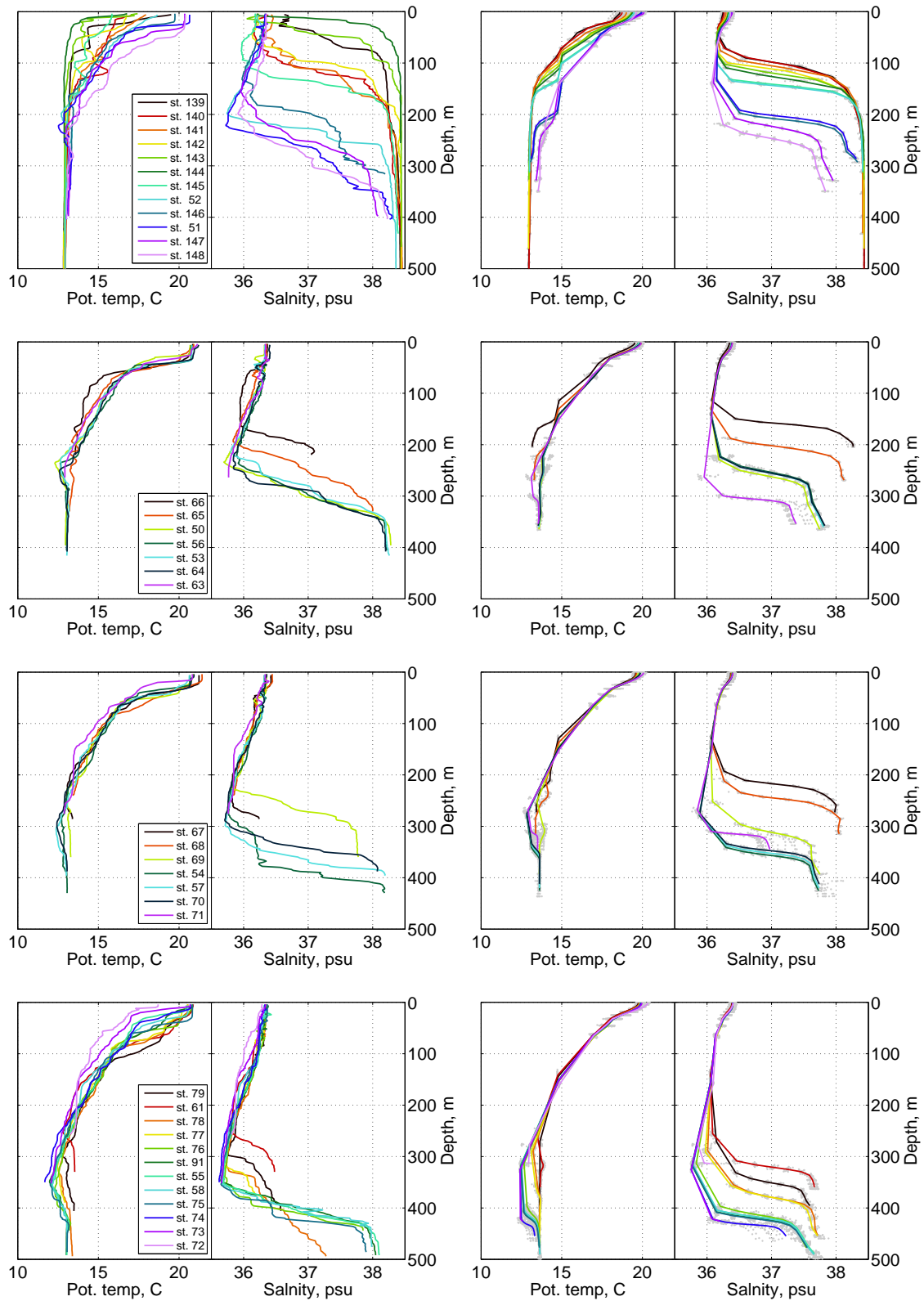


Figure 4.4: Comparison of T/S profiles of CTD sections between observation (left panels) and model (right panels). From top to bottom are sections I, A, B, and C.

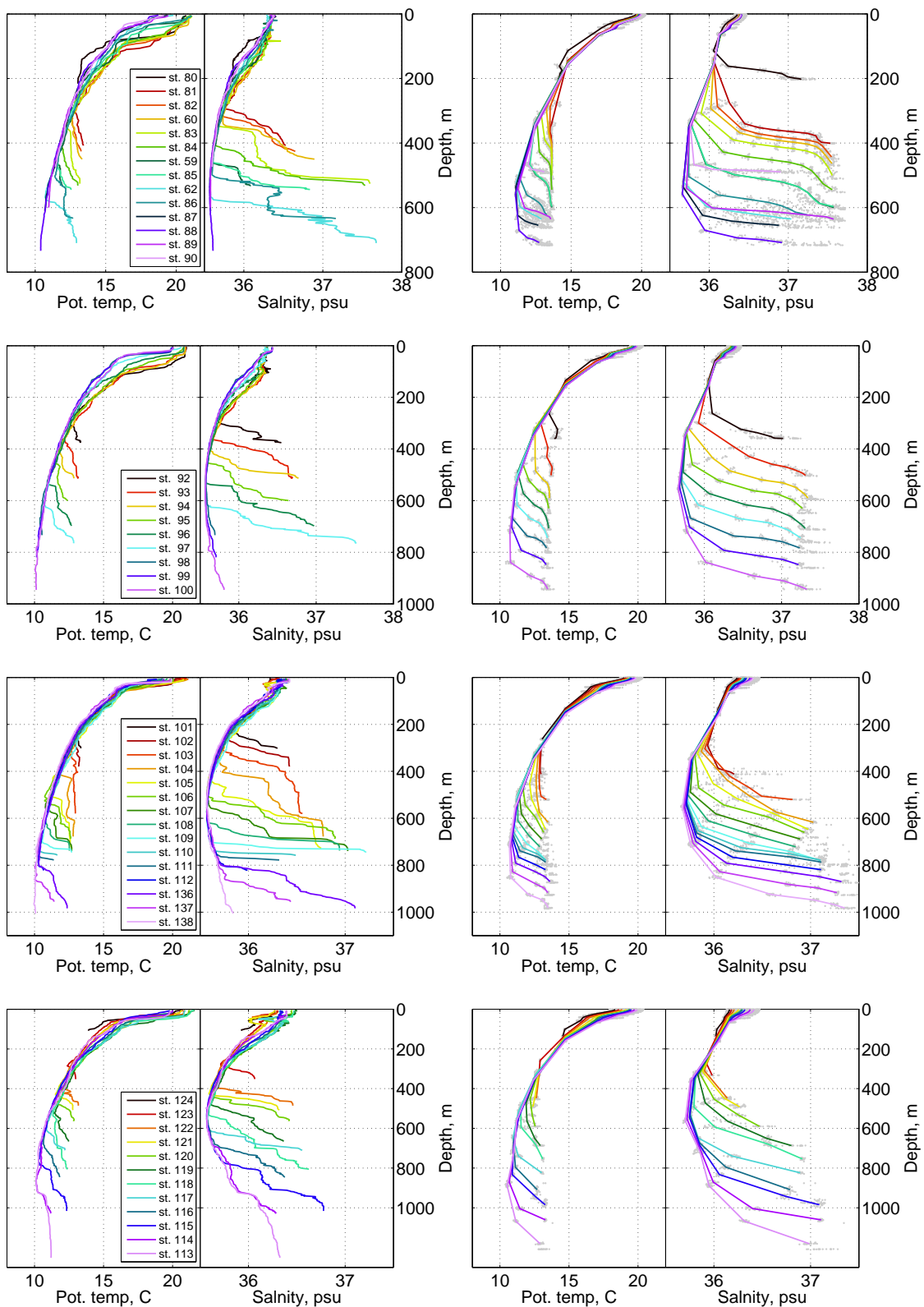


Figure. 4.4 continued, for sections D, E, F, and G.

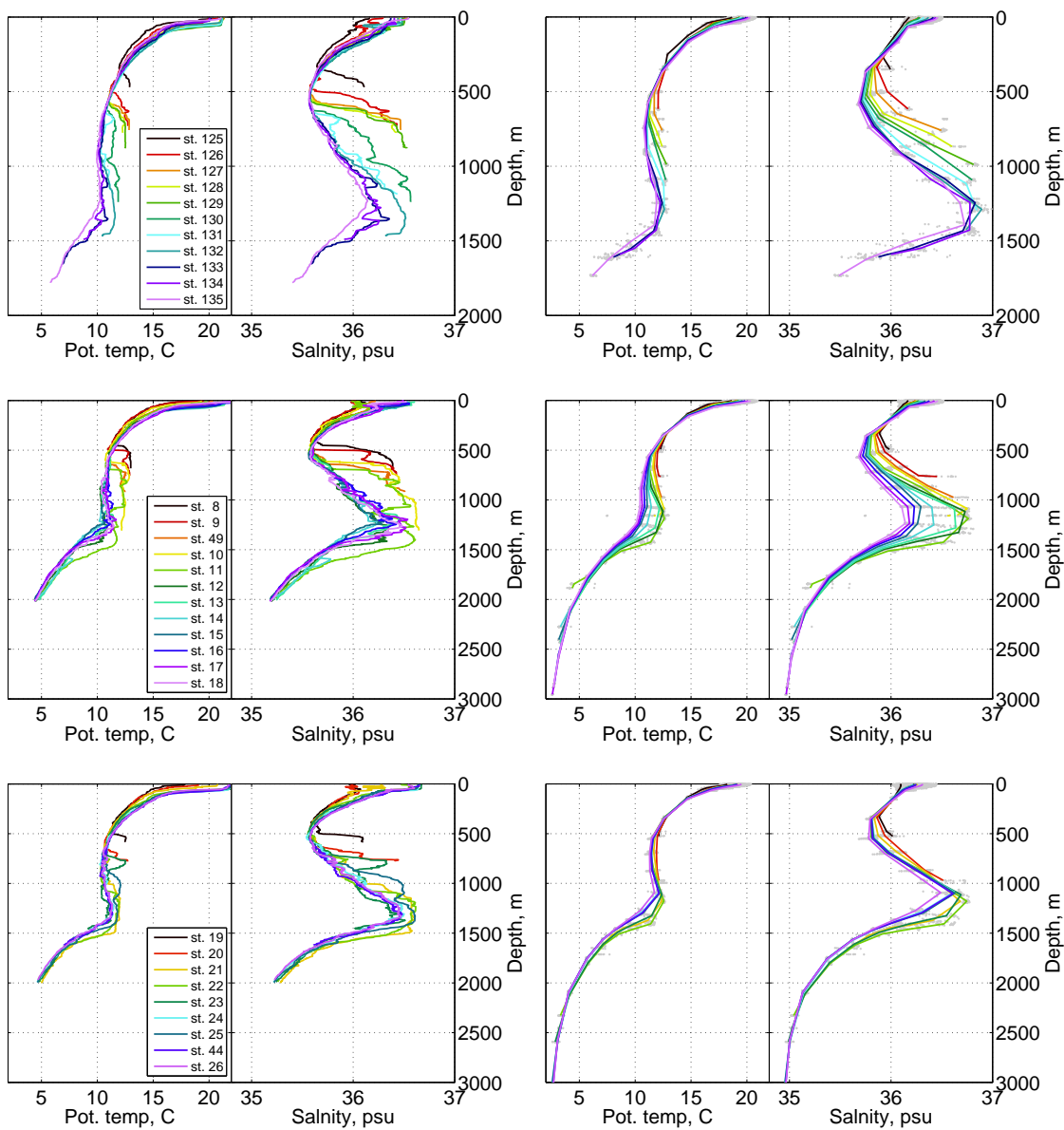


Figure. 4.4 continued, for sections H, J, and K.

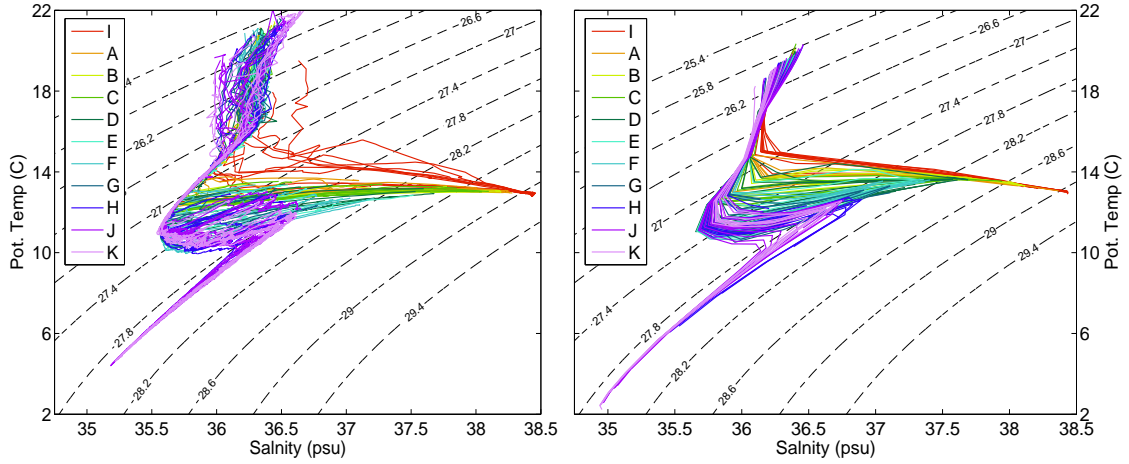


Figure 4.5: Comparison of T/S diagrams for all CTD sections between observation (left panel) and model (right panel).

nearly identical velocity profiles. The simulation reproduces both the observed velocity magnitude of about 1 m s^{-1} in sections A to C and the typical vertical structure of the outflow velocity, with a maximum located between the weakly-stratified bottom layer and the interfacial layer of the outflow plume. This is due to the presence of both the bottom stress and the entrainment stress. The simulation also reproduces the change in outflow plume direction from southwestward at section B to northwestward at section C. As the plume travels farther downstream, the velocity decreases, and overall the simulated profiles are consistent with the observations.

4.4.4 Steering and spreading of the outflow plume

While the MOW plume is naturally characterized by its westward velocity near the Strait, in the Gulf of Cádiz, it is defined in our simulation as the water mass below the NACW with salinity $S \geq \max(S_c, S_0 + \Delta S)$, in which S_0 is the initial mean salinity profile in the Gulf and ΔS and S_c are constants of 0.05 psu and 36.0 psu, respectively. The idea is to ‘capture’ all the newly-formed MOW in the Gulf. Based on this definition, the vertically

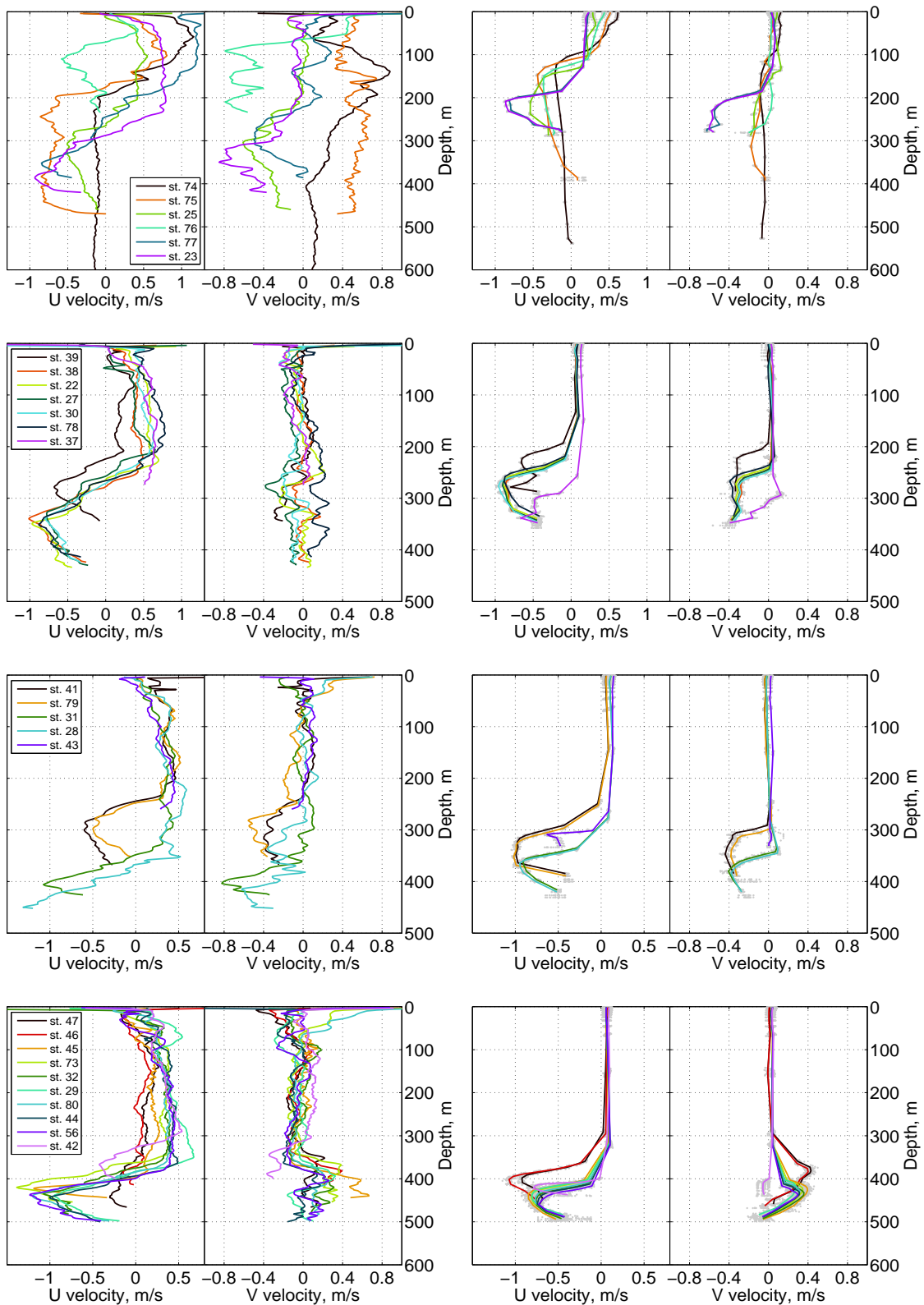


Figure 4.6: Comparison of U/V profiles of XCP stations between observation (left panels) and model (right panels). From top to bottom are sections I, A, B, and C.

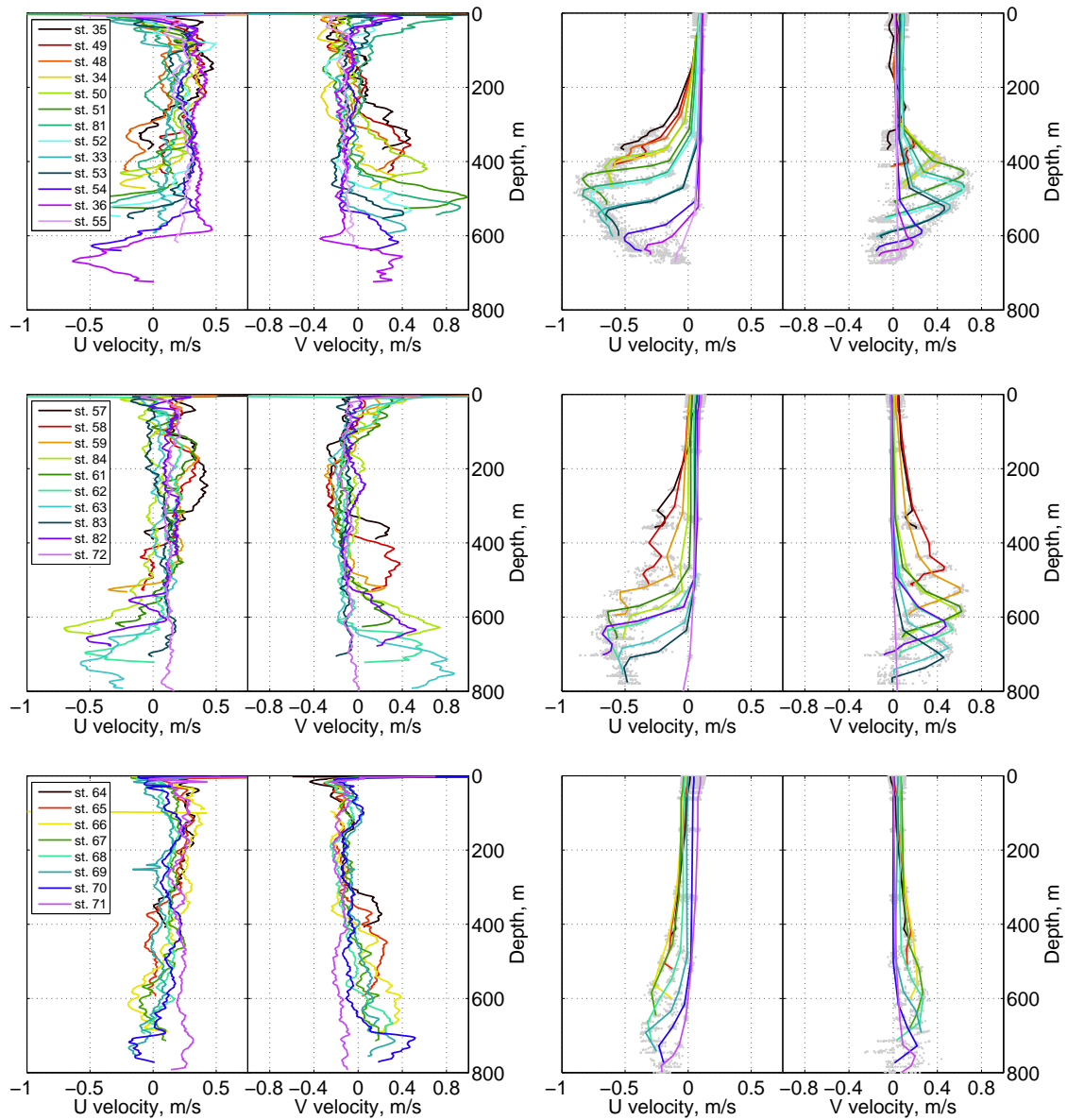


Figure 4.6 continued, for sections D, E, and F.

averaged velocity of the MOW plume $\bar{\mathbf{u}}$ is then calculated by

$$\bar{\mathbf{u}}(x, y, t) = h^{-1} \int_D^{D+h} \mathbf{u}(x, y, z, t) dz, \quad (4.1)$$

in which D and h in are the lower interface depth and the thickness of the outflow plume. The time-averaged (over the last 3 months) h and $\bar{\mathbf{u}}$ are shown in Fig. 4.7. The flow bears a pattern similar to that in the schematic diagram of Madelain (1970). The plume flows southwestward at the exit of the strait, where it is channel-constrained, then steers sharply to the northwest at the longitude of $\sim 6.4^\circ\text{W}$. A separation takes place at $\sim 7.0^\circ\text{W}$ and 36.0°N , where a small part of the plume deviates zonally while the greater part continues its travel northwestward along the continental slope. At $\sim 7.6^\circ\text{W}$ and 36.5°N , the plume encounters the Guadalquivir Bank which divides the flow into two branches, the larger part flowing southwestward and the remains northwestward. The MOW plume merges at west of 8.0°W and narrows as the steepness of the continental slope increases. The thickness h and velocity $\bar{\mathbf{u}}$ of the MOW plume from the CTD and XCP data are also plotted in Fig. 4.7 for comparison. XCPs were taken only near the exit of the Strait where the plume steering is clearly shown. Both the simulation and the observations show a thin outflow plume ($< 100\text{ m}$ thick) when it is bottom-trapped. The plume thickens at $\sim 8.0^\circ\text{W}$ where it becomes equilibrated at intermediate depth. However, the simulated MOW is considerably thicker than observed. This is because the upper interface of the outflow plume is shallower than that in the observations as shown in the T/S profile comparisons of sections H, J, and K. Also, the simulated MOW intrudes farther south than in the observation. The salty water is carried out from the westward-flowing outflow plume by an eddy formed at $\sim 8.2^\circ\text{W}$ moving southeastward slowly.

In the absence of bottom friction, the MOW plume accelerates down the slope driven

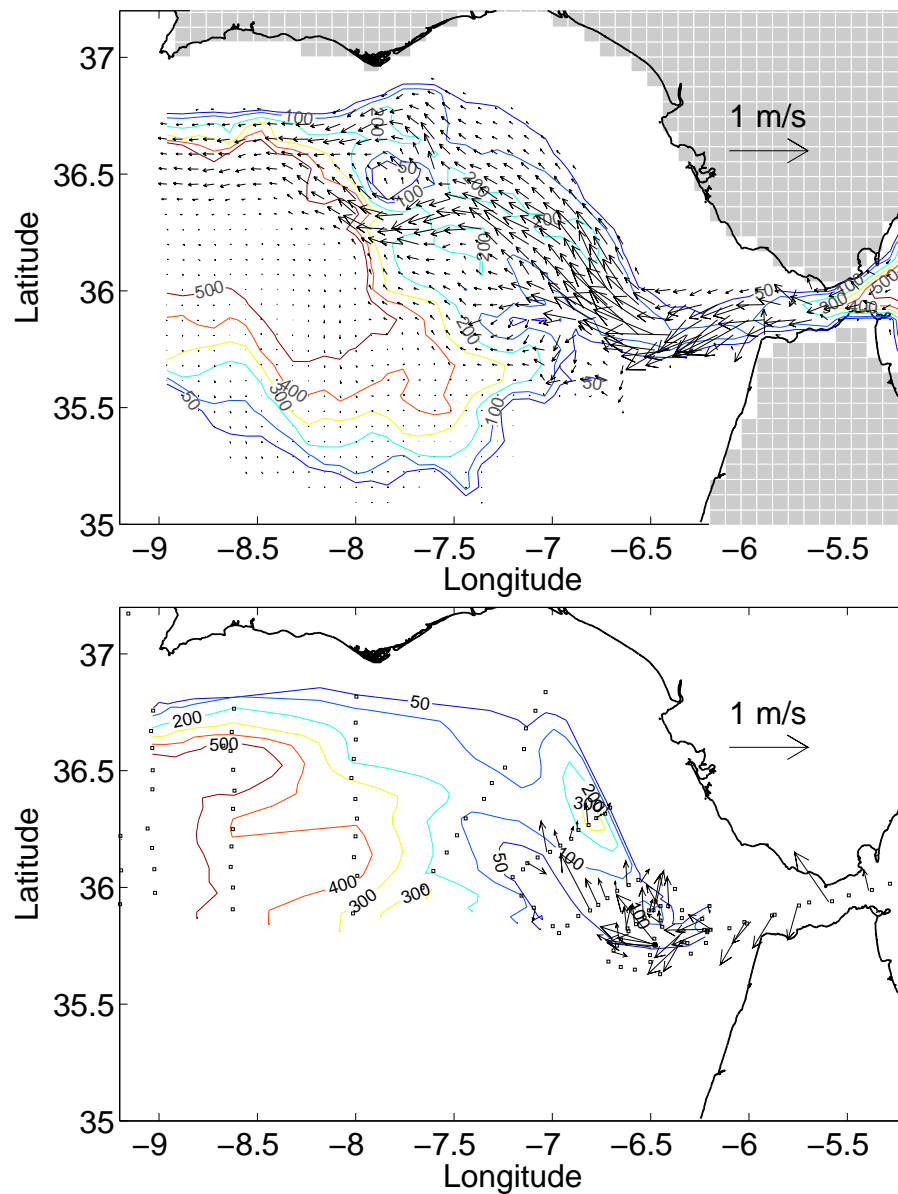


Figure 4.7: The horizontal structure of the simulated (upper panel) and observed (lower panel) MOW plume in the Gulf of Cádiz. The contour lines are 10 m, 50 m, 100 m, 200 m and 400 m time mean thickness; the arrows are the time and vertically averaged plume velocity.

by the strong pressure gradient, which is then balanced by the Coriolis force in the presence of earth rotation. The plume therefore undergoes a geostrophic adjustment which, for constant f , steers the flow direction from downslope to along the isobath. Baringer (1993) estimated a curvature *Rossby* number (the ratio of the Coriolis force to the curvature) of about $1/2$, implying that inertial effects are important in the cross section momentum balance. The mechanism underneath this sharp steering is a topic of debate. Ochoa and Bray (1991) attribute it to the presence of a northwest-southeast ridge, but Kenyon and Belderson (1973) suggest that the ridge itself is depositional and is likely caused by the persistence of outflow over decades. The present simulation does not resolve the ridge due to insufficient resolution. Nevertheless, it shows a flow direction change comparable to that observed. The steering therefore is mainly due to the Coriolis force associated with the swift outflow plume. However, the topography likely plays an important role in guiding the weak bottom flow just above the ocean floor. A small part of the simulated plume near the bottom ‘leaks’ southward, while most of it steers northward after exiting the strait.

An inviscid geostrophic adjustment alone is insufficient to account for the descent of the outflow plume down the continental slope. The bottom stress damps the inertial motion and allows the plume to descend (Price and Baringer, 1994). Furthermore, the entrainment of the NACW introduces an entrainment stress at the upper interface of the plume. A classical Ekman layer theory would predict a southward (downslope) deflection in the lower part of the plume and a northward (up-slope) deflection in the upper part. This baroclinic structure, or secondary circulation, is observed in the XCP data, from which Baringer (1993) estimated an ensemble mean angle of 8.6° between the averaged velocities above and below the velocity maximum. The simulation shows a similar structure (Fig. 4.8), with an average angle difference of 12.6° . This secondary circulation determines the spreading

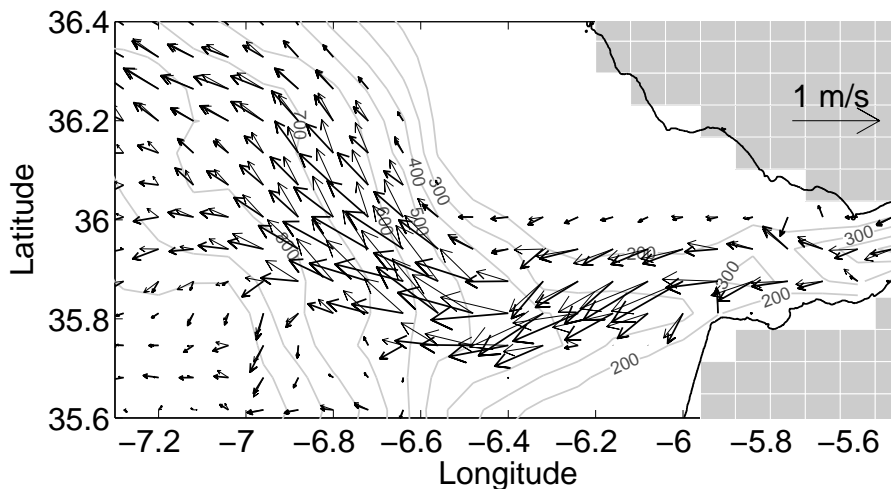


Figure 4.8: The mean horizontal velocity of the upper and lower half of the MOW plume, represented by thin and thick arrows, respectively. The contours show the isobaths increasing from 100 to 1000 m with interval of 100 m.

and broadening of the outflow plume. It also tends to carry the upper and more diluted part of the outflow water inshore and the lower and less diluted part offshore, and therefore plays a role in the spatial variation of outflow T/S properties in the cross section direction.

4.4.5 Descent and entrainment

The water properties of the Mediterranean outflow plume undergo a significant modification due to the entrainment of NACW as the plume descends along the continental slope of the Gulf of Cádiz. An important feature of the entrainment process, as shown both theoretically and observationally (Baringer, 1993; Price and Baringer, 1994), is the varying strength of entrainment along the stream, with strong entrainment associated with the initial steep descent of the outflow plume. In this section, we examine the ability of our simulation to reproduce this localized entrainment.

The downstream evolution of outflow water properties

One method of examining the entrainment is to diagnose the downstream evolution of outflow water properties. Considering the outflow plume as a whole, we can calculate the mean salinity S_{mean} and transport weighted salinity \bar{S} along different meridional sections as

$$S_{mean}(x, t) = \frac{\int_0^W \int_D^{D+h} S dz dy}{\int_0^W h dy}; \quad \bar{S}(x, t) = \frac{\int_0^W \int_D^{D+h} S u dz dy}{\int_0^W \int_D^{D+h} u dz dy}, \quad (4.2)$$

in which h and W are the thickness and width of the outflow plume, respectively. It is also straightforward to diagnose the maximum salinity of the outflow, $S_{max}(x, t)$, and the minimum salinity of the NACW above the outflow plume, $S_{NA}(x, t)$. The evolution of these four simulated salinities as a function of longitude is illustrated in Fig. 4.9. Several points should be made when compared with observations, in which S_{max} , S_{mean} , and S_{NA} are estimated directly from each CTD section, and in which \bar{S} is taken from Baringer (1993, table 2.3). First, the simulated maximum salinity of the outflow between 6.5°W and 8.0°W is significantly higher than observed. This is due to a small amount of salty water flowing slowly at the very bottom. This problem is much improved by including bottom boundary layer mixing in the model. Second, the simulated S_{mean} and S_{NA} have very similar evolution, both decrease rapidly from 38.3 to 36.8 psu between the exit of the strait and $\sim 6.8^\circ\text{W}$, while decreasing slowly farther downstream. This is consistent with the observational results, in which the salinity decrease is localized east of section D. Finally, the simulated salinity is overall higher than observed. This is primarily because the climatology used as initial condition has saltier NACW above the outflow plume. The minimum salinity of NACW, which remains almost constant throughout the simulation, is about $0.1 \sim 0.2$ psu higher than that in the observation.

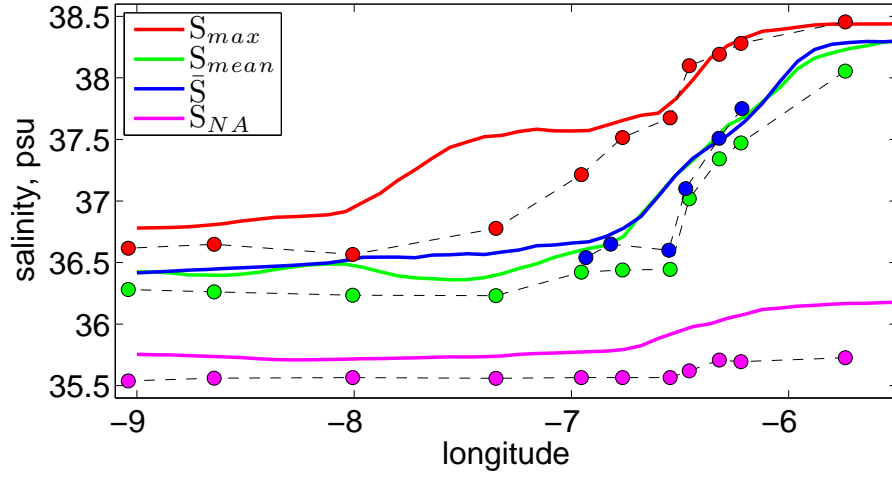


Figure 4.9: The evolution of salinities as a function of longitude. The solid lines are from simulation while the dash dot lines are from the observations. The color red, green, blue, and magenta represent S_{max} , S_{mean} , \bar{S} , and S_{NA} respectively.

The downstream evolution of volume transports

The second method of examining the entrainment is through the downstream increase of the outflow volume transport $Q_{out}(x, t)$, defined as

$$Q_{out}(x, t) = \int_0^W \int_D^{D+h} u dz dy. \quad (4.3)$$

As shown in Fig. 4.10, the simulated outflow transport increases from 0.76 Sv at the strait to ~ 1.7 Sv at 7° W, and remains nearly constant farther downstream. The near-doubling of the transport within the eastern Gulf of Cádiz is consistent with that shown in the XCP data (Price et al., 1993; Baringer, 1993), in which the transport increases from 0.88 Sv at section A to 1.53 Sv at section F. While the time-mean transport of the outflow within the strait might now be regarded as fairly well known, the transport within the Gulf of Cádiz is not. Most studies indicate that the MOW transport increases by a factor of about 3 somewhere in the Gulf of Cádiz (e.g., Ambar and Howe, 1979b; Ochoa and Bray, 1991; Rhein and Hinrichsen, 1993). But exactly where and how this increase takes place is unclear. West

of 8°W , the simulated transport decreases slightly. This is likely due to horizontal mixing with the relatively fresh water in the interior so that part of the outflow water has salinity less than S_0 .

Assuming the Mediterranean outflow source water has a constant salinity, $S_{Med} = 38.44$ psu, and the entrained NACW has the salinity of S_{NA} , we can use the conservations of mass and salt to estimate the transport of pure Mediterranean water Q_{Med} and the transport of the entrained NACW Q_{ent} :

$$Q_{out} = Q_{Med} + Q_{ent}; \quad \bar{S} Q_{out} = S_{Med} Q_{Med} + S_{NA} Q_{ent}, \quad (4.4)$$

Eq. 4.4 can be rewritten as

$$Q_{med} = \left[\frac{\bar{S} - S_{NA}}{S_{Med} - S_{NA}} \right] Q_{out}; \quad Q_{ent} = \left[\frac{S_{Med} - \bar{S}}{S_{Med} - S_{NA}} \right] Q_{out}. \quad (4.5)$$

Q_{out} , Q_{Med} and Q_{ent} are plotted as a function of longitude in Fig. 4.10. The Mediterranean source water transport (red line), which by definition should remain constant, decreases by about 25% from the strait to 8.5°W . This indicates that the flux of pure Mediterranean water was not conserved exactly and that the transport increase was only approximately consistent with the decrease of salinity \bar{S} . The evolution of Q_{ent} (blue line) is similar to that of Q_{out} since Q_{Med} varies only slightly. The entrainment is primarily taking place east of $\sim 7^\circ\text{W}$.

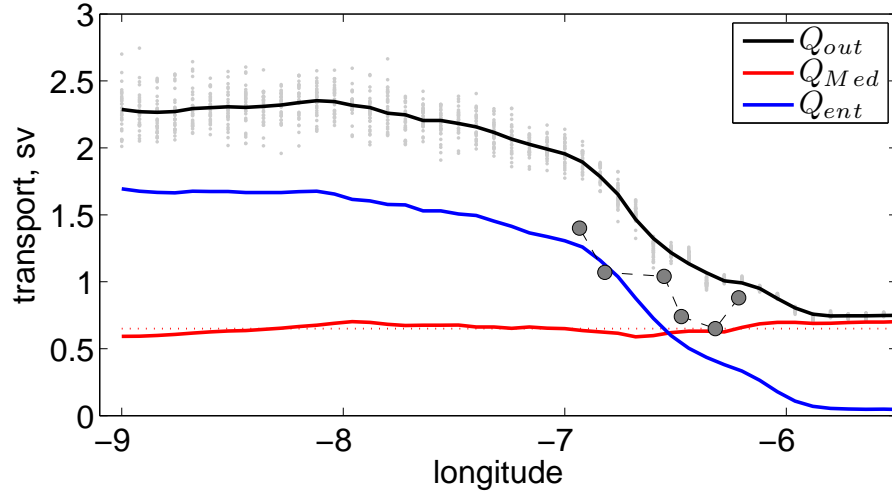


Figure 4.10: The evolution of volume transports as a function of longitude. The black line is the 3-month mean total transport, with the gray dots present the transport in every 3 days. The black dots are the volume transport through sections A to F, from the Table 1 of Baringer and Price (1997a). The red and blue lines are Q_{Med} and Q_{NA} , from Eq. 4.5.

The entrainment velocity w_E

Based on the evolution of salt flux or entrainment transport, we can estimate the entrainment velocity w_E . The equation for the salinity integrated over the cross section is

$$\partial_x \int_D^{D+h} \int_0^W S u dz dy = - \int_0^W w_E S_{NA} dy. \quad (4.6)$$

Using the continuity equation, this can be rewritten as

$$\bar{u} \partial_x \bar{S} = \frac{(\bar{S} - S_{NA}) w_E}{\bar{h}}, \quad (4.7)$$

where \bar{u} and \bar{h} are the averaged plume velocity and thickness, and \bar{S} and S_{NA} are transport weighted outflow salinity and entrained NACW salinity, respectively. Alternatively, the entrainment velocity can also be estimated directly from the evolution of the entrainment

transport Q_{ent} alone. By definition we have

$$\partial_x Q_{ent} = w_E W. \quad (4.8)$$

The estimated w_E s are plotted in Fig. 4.11. Based on the downstream evolution of salt flux, w_E reaches a maximum of about 0.4 mm s^{-1} just west of 6.0°W and another maximum of close to 0.8 mm s^{-1} at about 6.5°W . It then decreases rapidly and remains small west of $\sim 7.0^\circ\text{W}$. The evolution of the w_E based on the entrainment transport is very similar, but its magnitude is considerably lower, 0.4 mm s^{-1} . Overall, this localization of entrainment is consistent with the observations, in which the entrainment primarily takes place between sections C and D. The simulated entrainment velocity magnitude is smaller by a factor of 2 or 3 than the estimates of Baringer (1993). The difference is primarily due to the fact that the simulated outflow plume is wider than observed and that the entrainment takes place over a longer distance. The total effects of the entrainment, as seen in Fig. 4.9 and Fig. 4.10, are in good agreement with the observations.

The vertical structure of outflow volume transport

To investigate additional detail of the evolution of MOW, we plot the vertical structure of the total MOW transport through sections A to F in comparison to that from observations (Fig. 4.12). For the depth and density classes, the transport is divided into bins of 20 m and 0.01 kg m^{-3} , respectively. The observation shows that the outflow descends primarily between sections B and E (Baringer and Price, 1997a). The simulation reproduces the overall increase of depth and decrease of density quite well, including that, at section D, both observation and simulation show multiple transport maxima at different depth. However, there are two major differences. 1) An eastward return flow is present in the observation

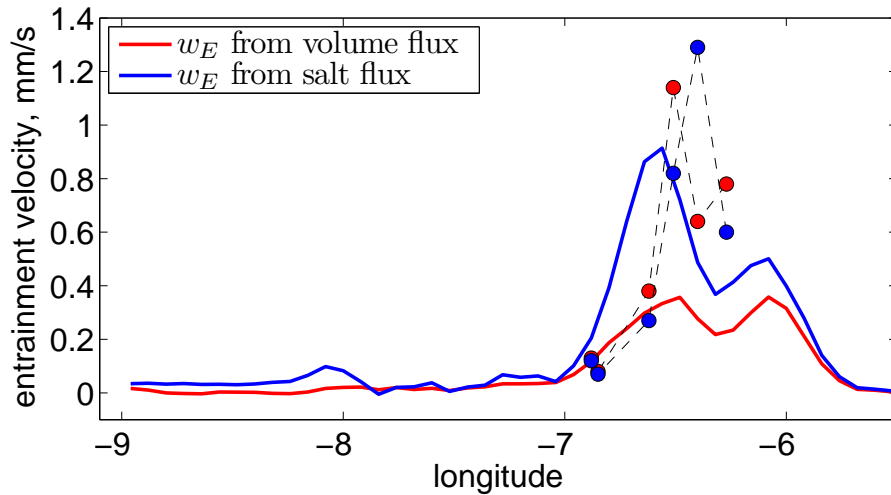


Figure 4.11: The entrainment velocity w_E (in mm s^{-1}) as a function of longitude estimated from simulation (lines) and observations (dot lines). The observations estimates are taken from Baringer and Price (1997b). The color red and blue represent the velocity diagnosed from volume and salt flux, respectively.

at all six sections just above outflow. In the simulation, the return flow is much weaker at sections D and E, and totally in absent at section F. This is because the configuration has closed boundaries and has no surface forcing so that the circulation in the upper ocean is not well represented. 2) The observations suggest that little entrainment takes place east of section A, and that the outflow water at section A is mainly the source water with a high density of 28.9 kg m^{-3} . In the simulation, however, strong entrainment has already taken place east of section A, which significantly modifies the outflow water properties.

4.5 Summary and discussion

To evaluate the performance of the entrainment parameterization in simulating realistic outflows, a regional HYCOM simulation of the Mediterranean outflow with a horizontal resolution of 0.08° is carried out and the numerical results are compared to field data obtained in the Gulf of Cádiz Expedition (1988). The model is forced by the density contrast between the North Atlantic Ocean and the Mediterranean sea, which drives a

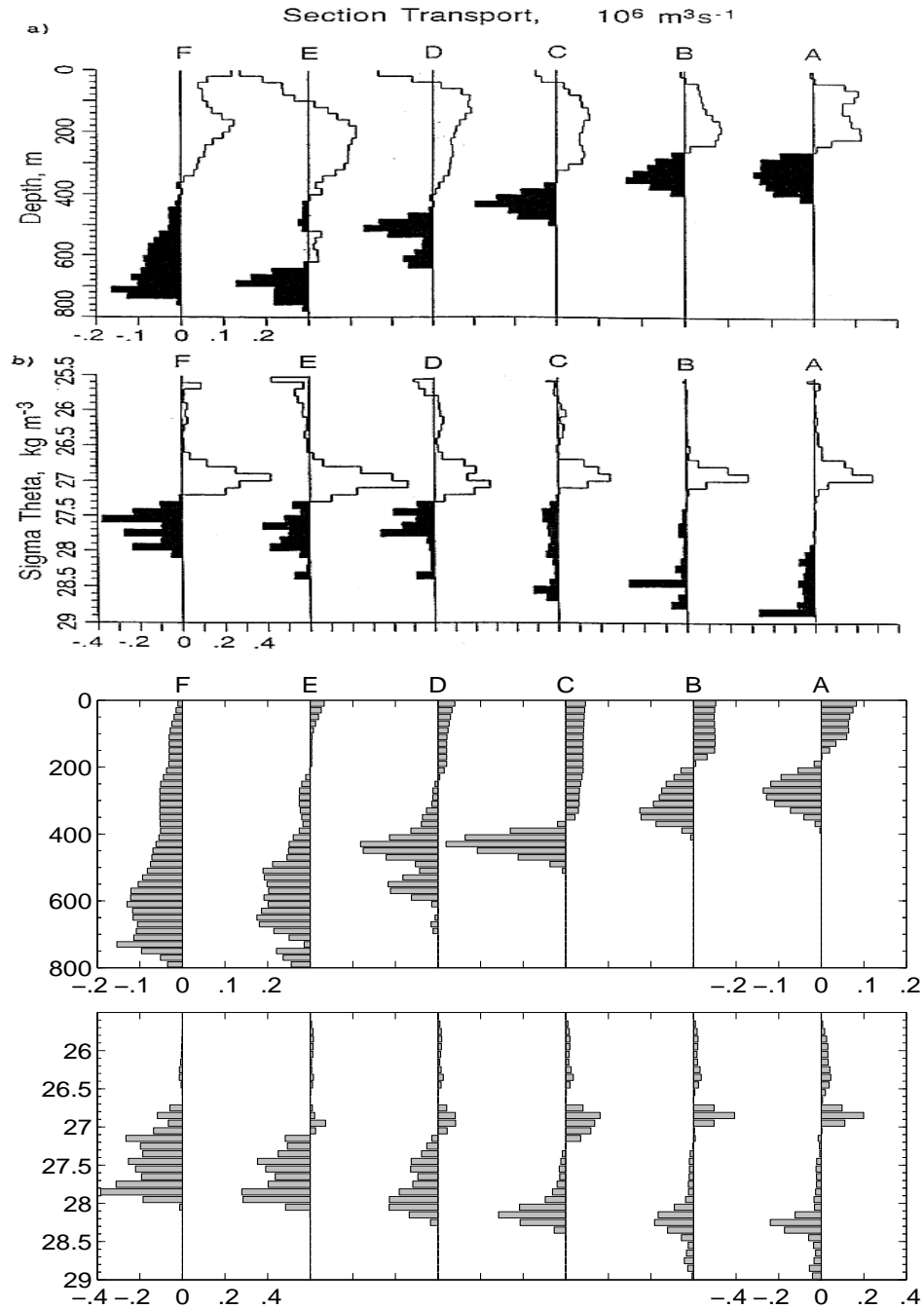


Figure 4.12: Volume transport of MOW (in Sv) in classes of depth (in bins of 20 m) and of potential density (in bins of 0.01kg m^{-3}) through sections A to F. The upper two panels are observations from Fig. 14 of Baringer and Price (1997a) and the lower two panels are from the simulation.

rather realistic exchange flow through the Strait of Gibraltar.

The model-data comparison shows that the simulation reproduces the observed Mediterranean outflow in the Gulf of Cádiz quite well, including the evolution of temperature, salinity and velocity profiles, the steering and spreading of the outflow plume as it descends along the continental slope, and most importantly, the localized entrainment immediately west of the strait where the outflow water experiences a significant modification in both volume transport and water properties. This localized entrainment, as both observationally and theoretically shown, is associated with the descent of the outflow.

Chapter 5

The sensitivity to horizontal and vertical resolution

The model-data comparisons in chapter 4 show that the 0.08° HYCOM simulation with the algebraic entrainment parameterization reproduces the observed evolution of MOW in the Gulf of Cádiz quite well. The aim of this chapter is to investigate how well this parameterization performs with different resolutions. This is an important question because regional, basin-scale, and global climate models run with a wide range of grid sizes. And since the parameterization is Ri -dependent, its performance might strongly rely on the model's capability in resolving Ri . Using an idealized configuration, Chang et al. (2005) show that with a specific parameterization, HYCOM simulations with horizontal grid size ranging from 50 m to 1 km display a similar entrainment evolution. Here we focus on the sensitivity to the resolutions (0.08° , 0.16° , and 0.32°) that are typical in eddy-resolving or eddy-permitting simulations. Associated with the variations of horizontal resolution is an issue of the representation of bottom topography in the model, Different approaches are therefore investigated. The sensitivity to vertical resolution will also be addressed.

5.1 Experiments with decreasing horizontal resolution

Our first approach is to use the 0.08° configuration as a reference and decrease the horizontal resolution. Two configurations with horizontal grid size of 0.16° and 0.32° are designed, in which the computational domain, vertical layer set-ups, relaxation near the boundaries, and background diffusivity and viscosity are all the same as in the 0.08° configuration. The topography, temperature, and salinity fields are averaged from those used in the 0.08° model. In doing so, high-resolution features of the topography (including the coast line) are smoothed. This results in a slightly wider and shallower Strait of Gibraltar in the coarse resolution configurations (see Table 5.1). The geometry of the strait is a key factor that controls the exchange flow. The 0.16° configuration originally had a volume transport through the strait about 15% less than that of 0.08° and 0.32° and we artificially ‘deepened’ the strait by 20 m in this configuration in order to have a comparable flux. The resulting volume and salinity transports as a function of time are plotted in Fig. 5.1 with time averaged values listed in Table 5.1. It should point out the 0.32° configuration has the sill shallower than the other two while simulates a comparable volume transport. This is because that the strait becomes zonal with 0.32° since there is only one grid point in the strait. The volume transport of the 0.32° run also shows larger variations than in the other two runs. But overall, the time-averaged fluxes from the runs with different resolution compare well to observational values, which provides a basis for further comparison.

Table 5.1: The geometry of the Strait of Gibraltar, the simulated volume and salinity transports (time mean \pm standard deviation) across the strait in 3 different configurations.

horizontal resolution ($^\circ$)	0.08	0.16	0.32
strait width (grid nums/km)	3/21.6	2/28.8	1/28.8
sill depth (m)	287	241	210
volume transport ($10^6\text{m}^3\text{s}^{-1}$)	-0.76 ± 0.018	-0.76 ± 0.023	-0.75 ± 0.058
salinity transport ($10^3\text{m}^3\text{s}^{-1}$)	-1.54 ± 0.050	-1.46 ± 0.062	-1.43 ± 0.132

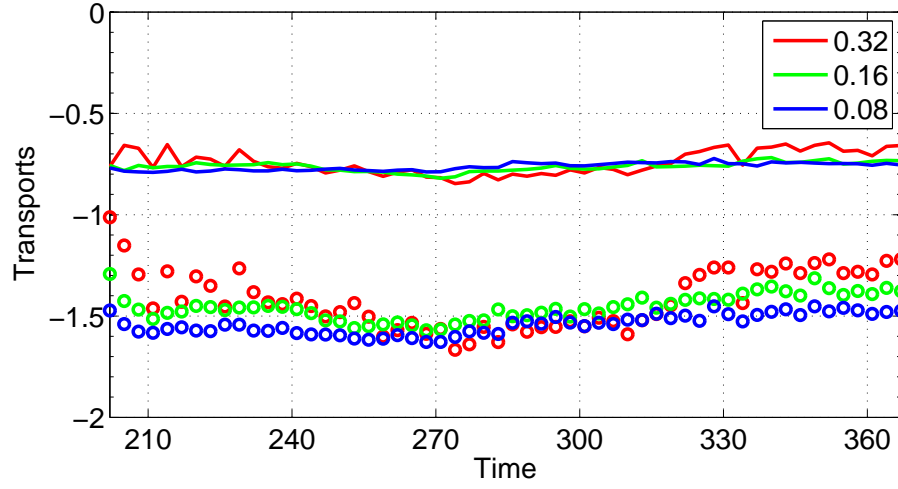


Figure 5.1: Time evolution of the simulated volume transport (lines, in Sv) and salinity transport (circles, in $10^3 \text{ m}^3 \text{ s}^{-1}$) through the Strait of Gibraltar. Values are negative because the transport are westward. The red, green, and blue color represent horizontal resolution of 0.32° , 0.16° and 0.08° , respectively.

Snapshots of the simulated salinity distribution at 2 meridional sections (9°W and 8°W) are compared in Fig. 5.2. For the 0.08° and 0.32° configurations, the simulated MOW equilibrates at depths between 1000 m to 1500 m, comparing well with observations. The core salinity at 9°W is about 36.7 psu, slightly higher than the observed value of 36.6 psu. The MOW in the 0.16° run extends deeper and has a slightly lower salinity maximum compared to the other two runs. The reason, as shown in the 8°W section, is that part of the salty water at the bottom descends underneath the salinity maximum and mixes with the fresh water there. From the 8°W plot, it is also clear that the MOW at 0.32° resolution has a higher core salinity value than in the 0.08° run, indicating weaker entrainment.

The horizontal velocity structure of the simulated MOW plume in the Gulf of Cádiz with resolutions of 0.16° and 0.32° is plotted in Fig. 5.3. In comparison to Fig. 4.7, the plume loses the detailed features of meandering, sharp steering, and splitting due to the lack of resolution and fine topographic detail. Otherwise, the simulations are similar in terms of the general pattern. All show a widely spread, thin plume in the eastern gulf,

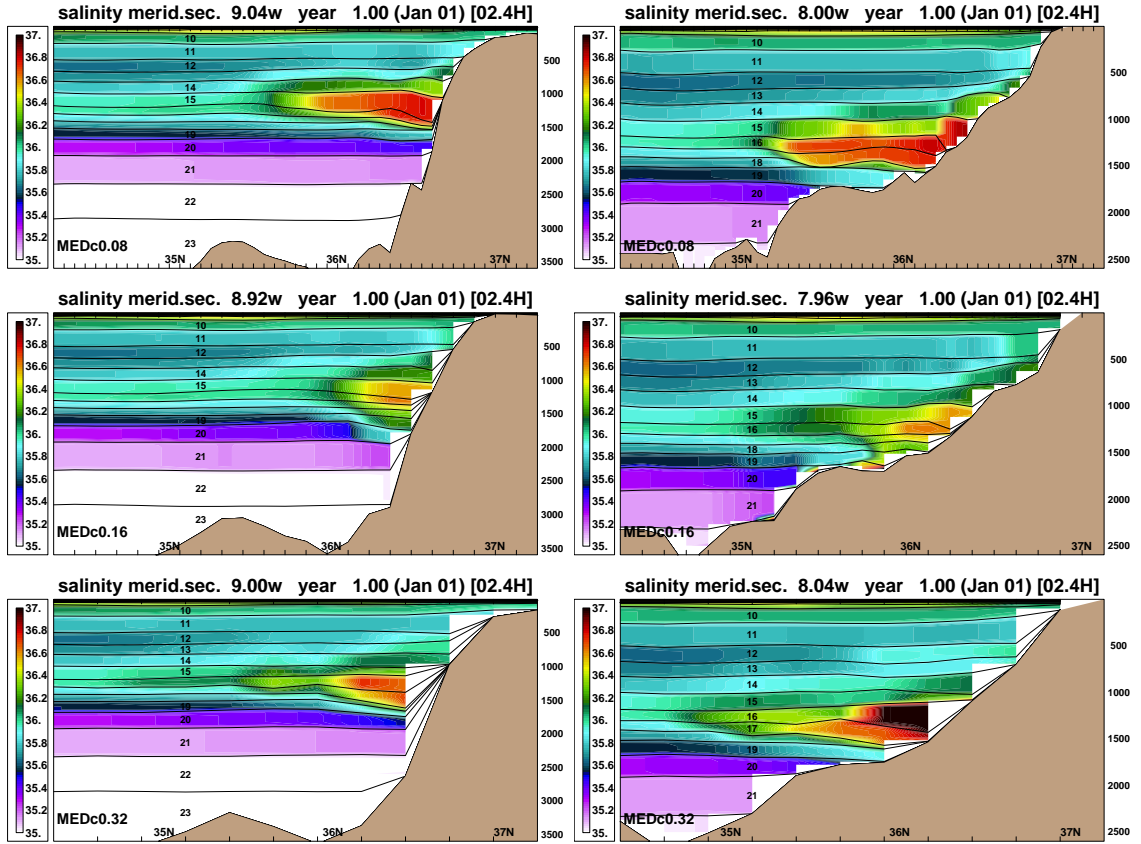


Figure 5.2: Snapshots of the salinity distribution at 9°W and 8°W . From top to bottom are simulations with horizontal resolutions of 0.08° , 0.16° , and 0.32° , respectively.

merging at $\sim 8^\circ\text{W}$ into a relatively narrow and thick boundary current. Although the model is configured with the same background viscosity parameters, the velocity of the plume becomes systematically weaker as the resolution decreases.

To quantitatively compare the simulated plumes, we calculated the width W , the meridionally-averaged thickness \bar{h} , depth \bar{D} , and velocity $|\bar{u}|$, the volume transport Q_{out} , and the salinity \bar{S} . The results are plotted in Fig. 5.4 as a function of longitude. For all three configurations, the plume increases its width from ~ 20 km at the strait to ~ 140 km at about 7°W , remains nearly constant in width until about 8.5°W , and narrows slightly farther downstream. \bar{h} is nearly constant (~ 100 m) between the strait and $\sim 7.3^\circ\text{W}$, then increases rapidly to ~ 400 m at $\sim 8.0^\circ\text{W}$, and stabilizes farther downstream. \bar{D} shows

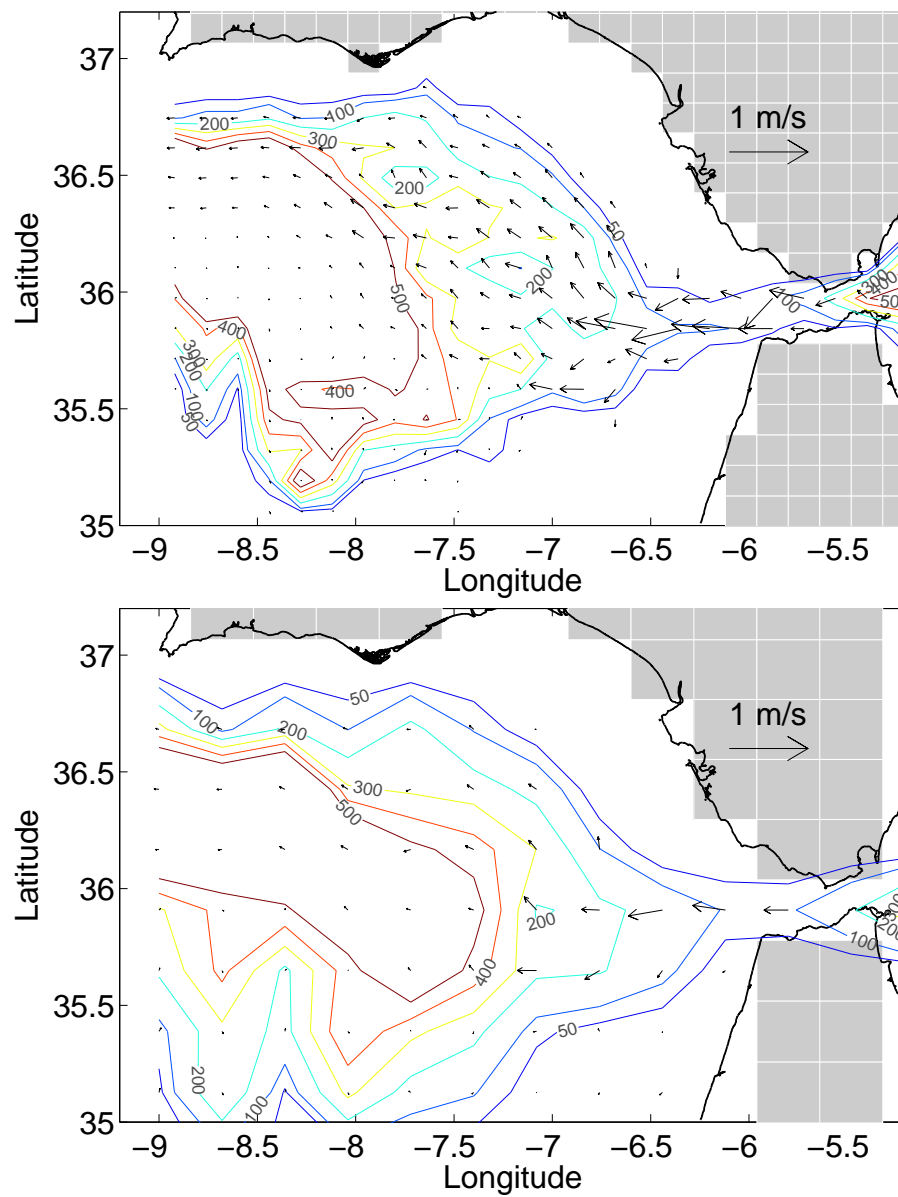


Figure 5.3: The same as Fig. 4.7 but for configurations with horizontal resolutions of 0.16° (upper panel) and 0.32° (lower panel), respectively.

a continuous increase from 200 m at the west end of the strait to > 1.0 km at 8°W , and then remains at that level. It is also clear that the simulated plume flows at greater depth when the resolution is decreased, indicating that the entrainment is becoming weaker. \bar{u} increases after the plume flows out of the strait and reaches the maximum velocity between 6°W and 6.5°W , where the plume undergoes steering, then decreases continuously farther downstream. The magnitude of \bar{u} decreases as the resolution increases. The outflow volume transport shows a different evolution in the 3 configurations. The transport in the 0.32° configuration continuously increases from the strait to 9°W , while the increase is localized east of 7°W in the 0.08° and 0.16° configuration. The volume transport of the 0.16° configuration decreases to the west of 7°W . This is primarily because part of the outflow water is excluded from the transport estimate after it mixes with the deep fresh water. The transport weighted salinity decreases from the strait to just east of 7°W and remains nearly a constant farther west. Overall, the entrainment becomes weaker as the horizontal resolution decreases. The simulated MOW with resolutions of 0.08° , 0.16° , and 0.32° all equilibrate at an intermediate depth of 1000 to 1500 m.

5.2 Experiments with increasing horizontal resolution and step topography

The three experiments discussed in section 5.1 have different topography because of the averaging process. The high-resolution features are filtered out when resolution decrease. To have an identical topography, the experiment must start from a low resolution configuration and the 0.32° configuration of section 5.1 is taken as the low resolution case. There are two possible method to represent topography as the resolution increases. One method is to keep the ‘step-like’, or the ‘bumpy’ topography, the other method is to linearly interpolate the

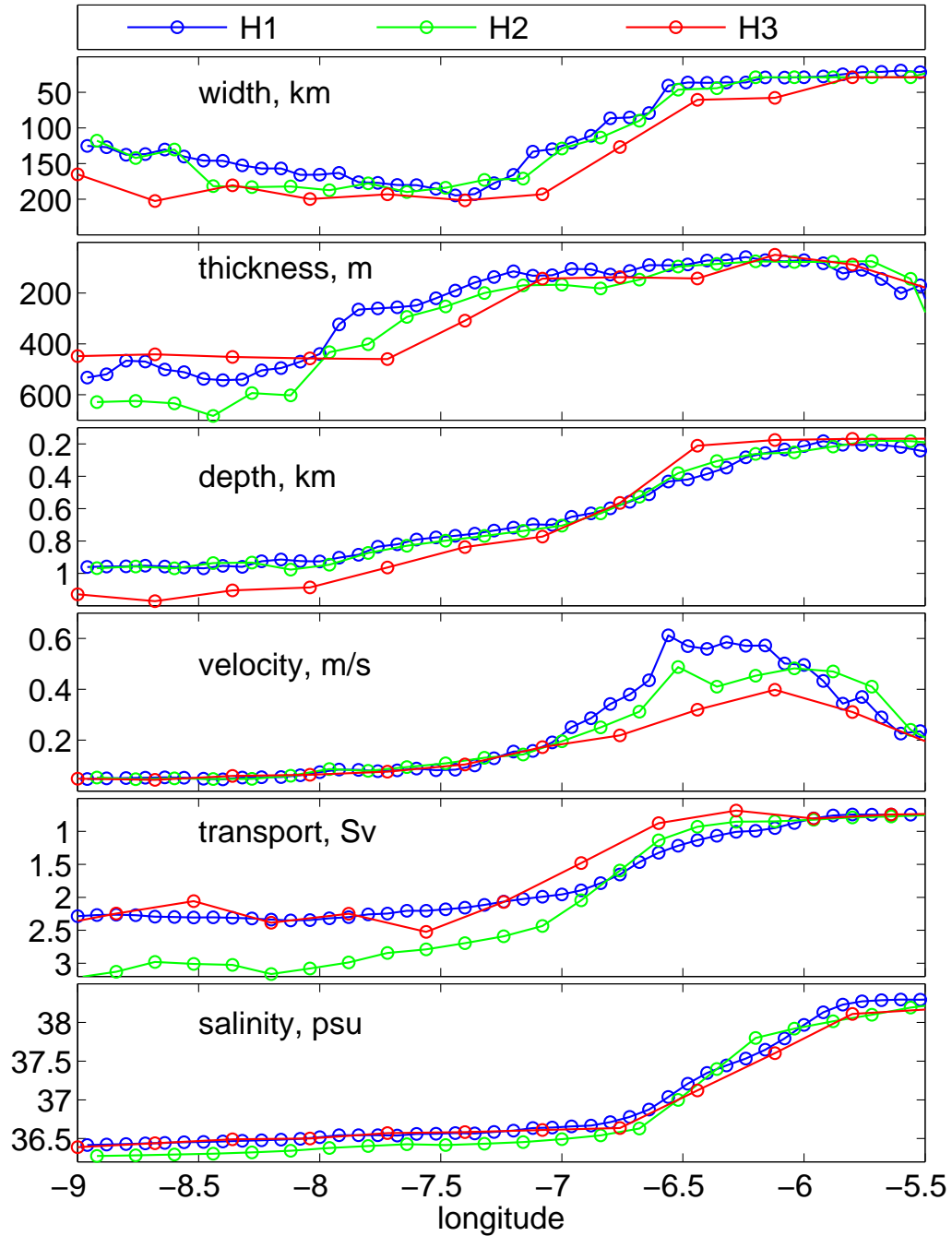


Figure 5.4: The width W , thickness \bar{h} , depth \bar{D} , velocity \bar{u} , volume transport Q_{out} , and salinity \bar{S} of the simulated Mediterranean outflow plume as a function of longitude. The color red, green and blue represent the configuration with horizontal resolution of 0.32° , 0.16° , and 0.08° , respectively.

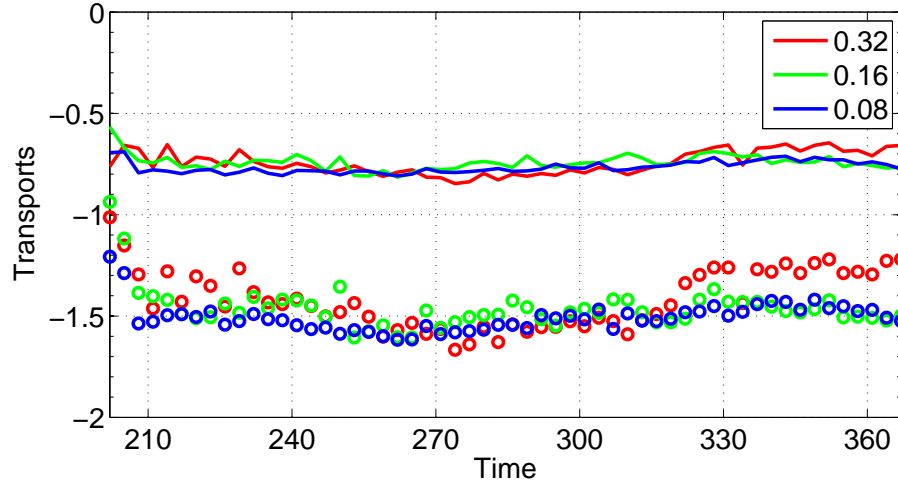


Figure 5.5: The same as Fig. 5.1 but for experiments with increasing horizontal resolution and step topography.

topography. The experiment with interpolated topography will be discussed in section 5.3. By dividing each grid box of the entire computational domain into a 2×2 and 4×4 cell, we obtain 2 configurations with resolution of 0.16° and 0.08° but step-like topography. The time evolution of the volume and salinity transport through the strait is plotted in Fig. 5.5, with the mean and standard deviation values listed in Table 5.2. Not surprisingly, the fluxes compare very well given the identical topography of the strait.

Table 5.2: The same as Table 5.1 for experiments with increasing resolution and step topography

horizontal resolution ($^\circ$)	0.08	0.16	0.32
strait width (grid nums/km)	4/28.8	2/28.8	1/28.8
sill depth (m)	210	210	210
volume transport ($10^6 \text{m}^3 \text{s}^{-1}$)	-0.77 ± 0.026	-0.75 ± 0.029	-0.75 ± 0.058
salinity transport ($10^3 \text{m}^3 \text{s}^{-1}$)	-1.52 ± 0.049	-1.48 ± 0.058	-1.43 ± 0.132

Snapshots of the salinity distribution at two sections in the Gulf of Cádiz are plotted in Fig. 5.6. The simulation with different resolutions differs significantly. Compared with 0.32° , the simulated MOW of 0.16° and 0.08° configurations equilibrate on deeper and denser isopycnals at 9°W . The layer interface of the 0.08° run shows some spurious ‘noisy

jumps' at 8.6°W with a spacing of $2\Delta x$. The difference of the three simulations highlights the importance of representing the topography change $r_{\Delta x}$ (defined as $\Delta H/\Delta x$) in the model, since the outflow is bottom-trapped and flows across the isobath. Even though the topography H is identical in the 3 configurations, the topography change $r_{\Delta x}$ ($\Delta H/\Delta x$) is not. While $r_{0.32}$ is continuous and smooth, $r_{0.08}$ is 'step-like', jumping between 0 and $4 \times r_{0.32}$.

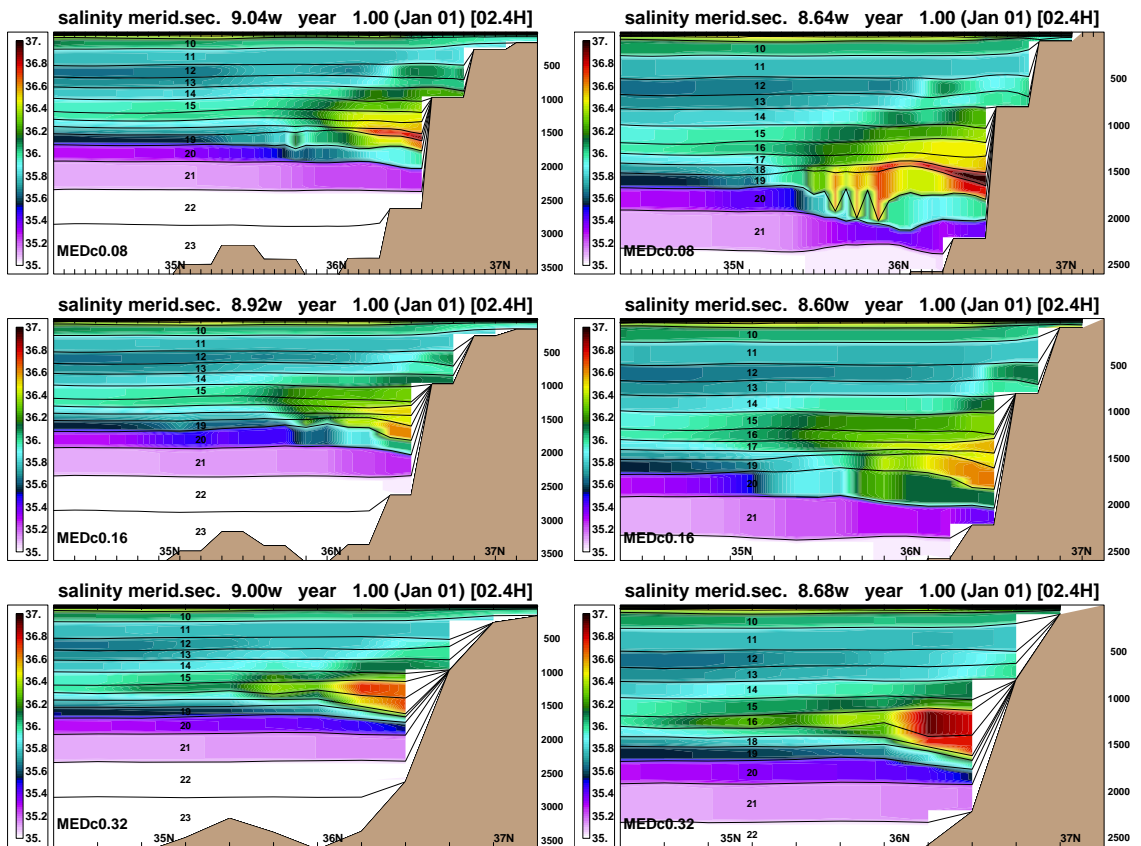


Figure 5.6: Snapshots of the salinity distribution at 9°W and 8.6°W . From top to bottom are simulations with horizontal resolution of 0.08° , 0.16° , and 0.32° , respectively.

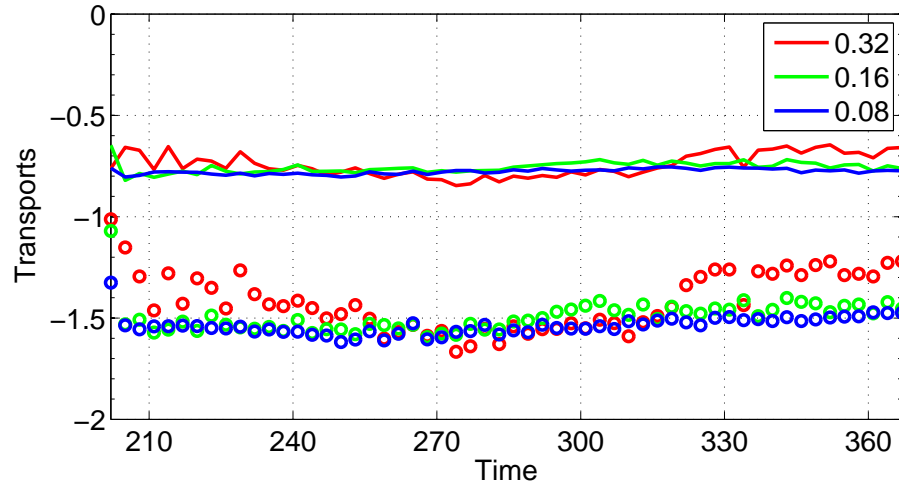


Figure 5.7: The same as Fig. 5.1 but for experiments with increasing horizontal resolution and interpolated topography.

5.3 Experiments with increasing horizontal resolution and interpolated topography

In order to investigate the sensitivity to horizontal resolution without the implication of different topography, and to examine if the results shown in Fig. 5.6 are due to the step-like topography, we carry out the experiments with increasing resolution and linearly interpolate the topography. In this way, the topography over different resolutions are consistent with one another in that they are the same topography mapped on different resolution. The difference from section 5.1 is also clear. The 0.08° configuration in section 5.1 contains high-resolution features that are gradually filtered out as the resolution decreases, whereas here none of the configurations has high-resolution features. The time evolution of the volume and salinity transport through the strait is plotted in Fig. 5.7, with the statistics listed in Table 5.3.

Snapshots of the simulated salinity distributions at 9°W and 8°W are compared in Fig. 5.8. These do not exhibit the ‘noise’ problem shown in Fig. 5.6. However, there are still

differences between Figs. 5.8 and 5.2, indicating that the high-resolution topographic detail is also important. Quantitatively, the bulk properties of the simulated MOW are compared in Fig. 5.9. Comparing to Fig. 5.4, the 0.16° and 0.08° configurations lead to stronger volume transport and equilibrate at shallower depths, indicating the entrainment is stronger with the smooth topography configuration. And the trend toward weaker entrainment in the lower resolution configurations becomes more significant.

5.4 Sensitivity to vertical resolution

The choice of vertical resolution, just like the choice of the vertical coordinate, is important for any numerical simulation. Here we briefly examine how sensitive the entrainment parameterization is to different vertical resolutions. The Mediterranean outflow product water equilibrates at layer 16. Thus what is important for the entrainment parameterization is the resolution below this layer. Four experiments with horizontal resolution of 0.08° are designed, which are identical except for the number and the distribution of the target densities from 36.62 to 37.48 kg m^{-3} the reference experiment as discussed in chapter 4 has 13 layers, two coarser resolution and one finer resolution experiments have 7, 3, and 15 layers, respectively. The distribution of these layers is illustrated in Fig. 5.10.

Salinity snapshots from these 4 experiments are compared at 9° and 8°W (see Fig. 5.11).

Table 5.3: The same as Table 5.1 for experiments with increasing resolution and interpolated topography.

horizontal resolution ($^\circ$)	0.08	0.16	0.32
strait width (grid nums/km)	4/28.8	2/28.8	1/28.8
sill depth (m)	210	210	210
volume transport ($10^6 \text{ m}^3 \text{ s}^{-1}$)	-0.78 ± 0.013	-0.76 ± 0.022	-0.75 ± 0.058
salinity transport ($10^3 \text{ m}^3 \text{ s}^{-1}$)	-1.54 ± 0.036	-1.50 ± 0.054	-1.43 ± 0.132

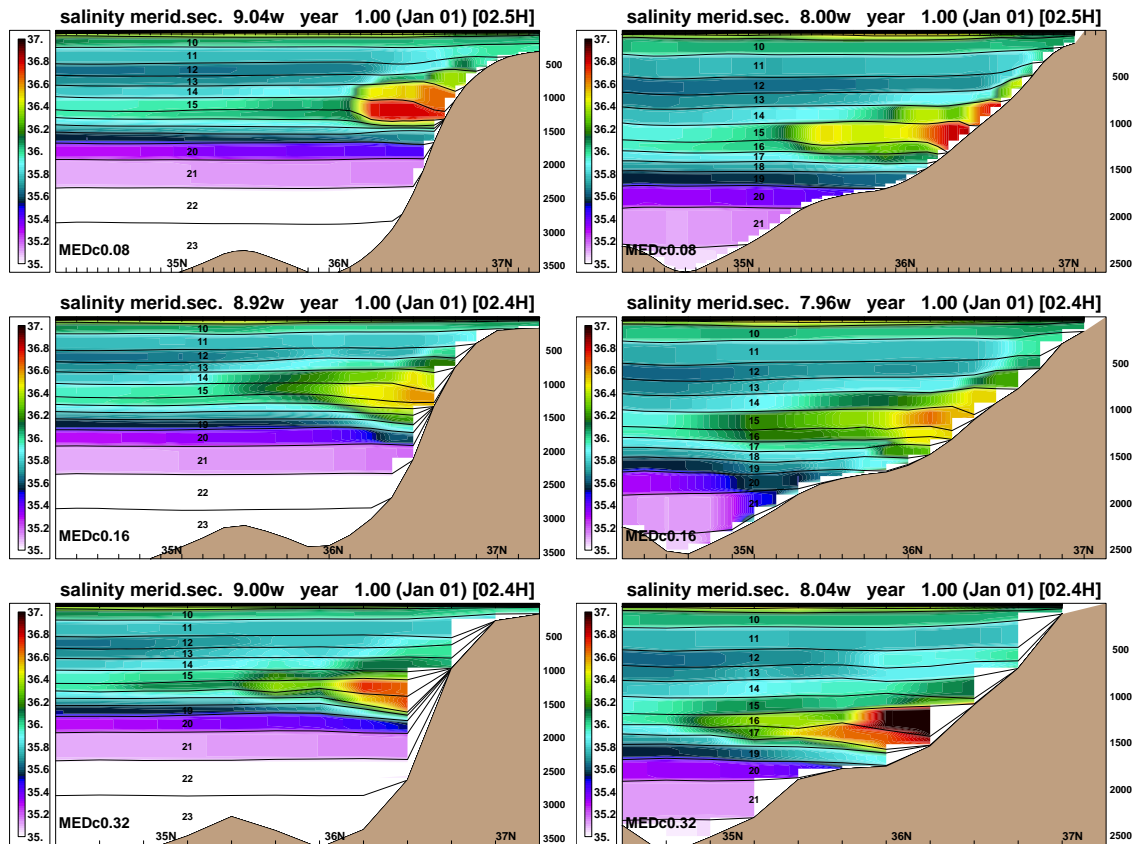


Figure 5.8: The same as Fig. 5.6 but for experiments with increasing horizontal resolutions and interpolated topography.

The two high-resolution configurations (13 and 15 layers) lead to very similar results. The simulated MOW in experiment with 7 layers between outflow source and product water descends deeper and mixes with the fresh water underneath the salinity maximum located between 1000 and 1500 m. Experiment with 4 layers gives the worst result. A significant part of the simulated MOW descends to the very bottom, and the entire water mass below 1000 m is affected by the presence of the MOW. Therefore, the entrainment parameterization is greatly affected by the vertical resolution. This is not surprising, since the vertical resolution is a key factor that influences the model's skill to resolve the shear Richardson number Ri . The parameterization requires about 10 layers between outflow and product water.

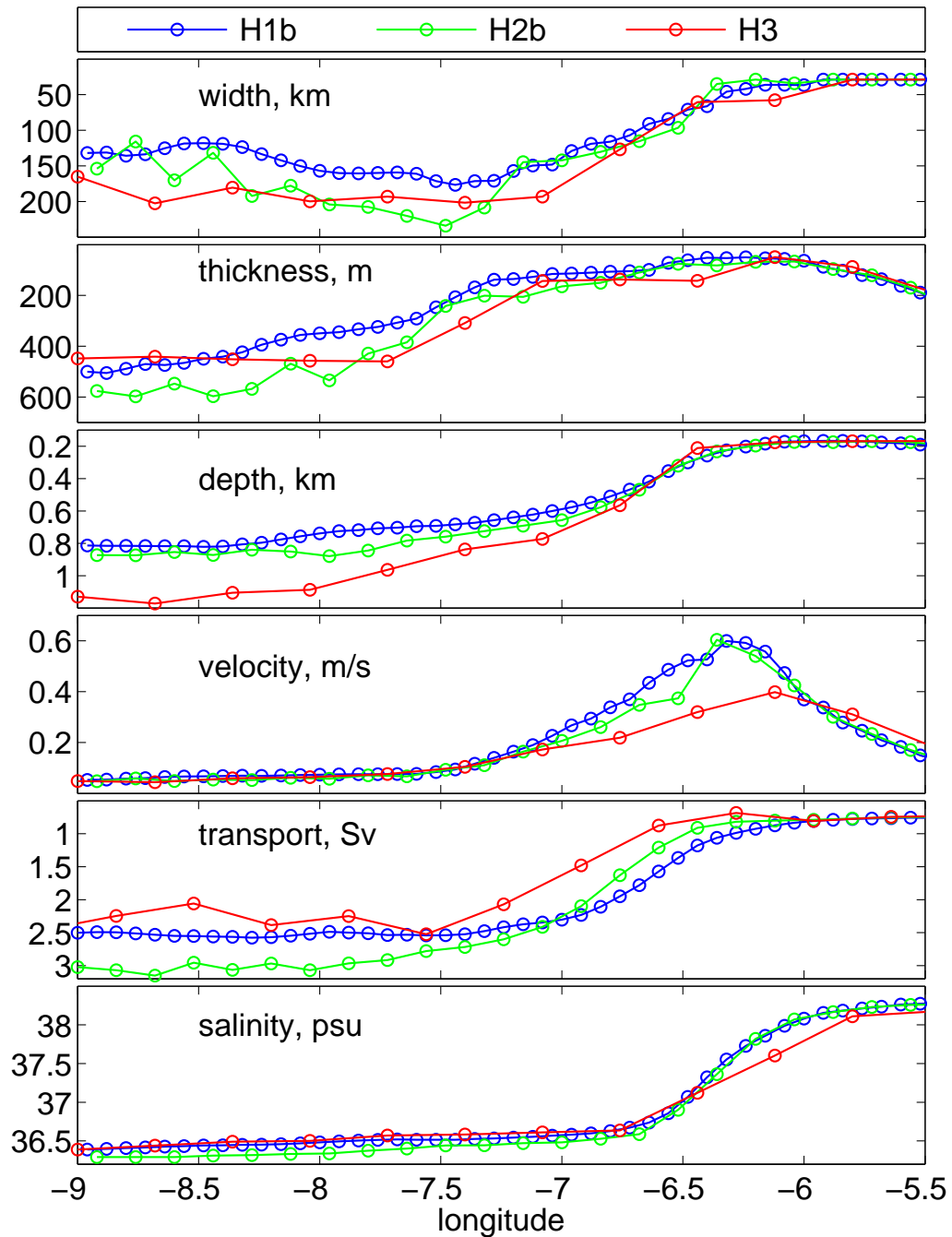


Figure 5.9: The same as Fig. 5.4 But for experiments with increasing horizontal resolutions and interpolated topography.

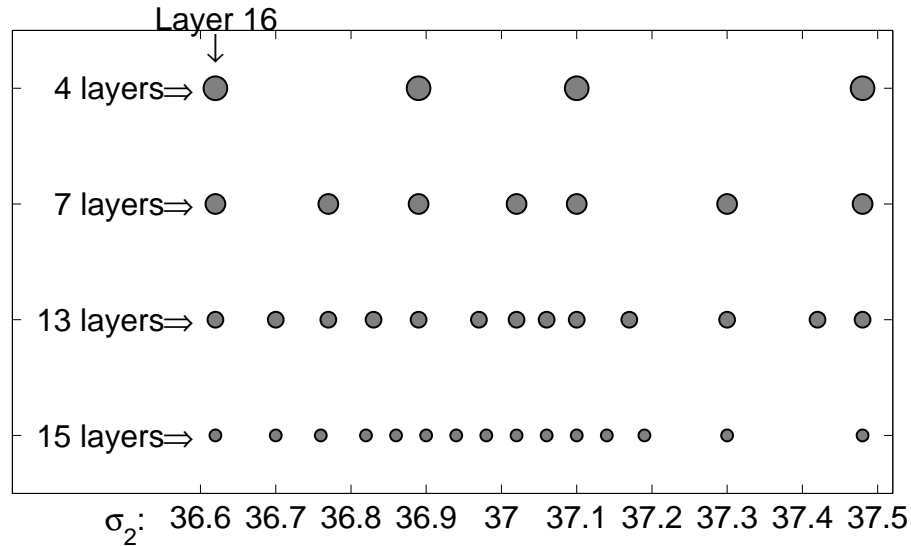


Figure 5.10: Number and distribution of the target densities ($\hat{\sigma}_2$) between 36.62 and 37.48 kg m^{-3} in 4 configurations. 13-layer is the reference experiment.

5.5 Summary and discussion

Motivated by the fact that current regional, basin-scale, and climate models have very different resolutions, the sensitivity of the performance of the entrainment parameterization to the model resolution has been investigated. The studies of the sensitivity to horizontal resolution emphasize the importance of the topography representation. Because outflows are bottom-trapped plumes that flow across isobaths, they directly ‘feel’ the variance of the topography. In a set of experiments with increasing resolution and step-like topography, the higher resolution simulations show significantly deeper and denser Mediterranean outflow water, as well as spurious ‘noise’ due to the discontinuous variation of model topography. The details of the simulated MOW also differ between experiments with and without high-resolution topographic detail, suggesting that these detail play an important role in the outflow simulations.

In addition to the implications by the topography representation, the performance of the entrainment parameterization varies under different horizontal resolutions, i.e., higher

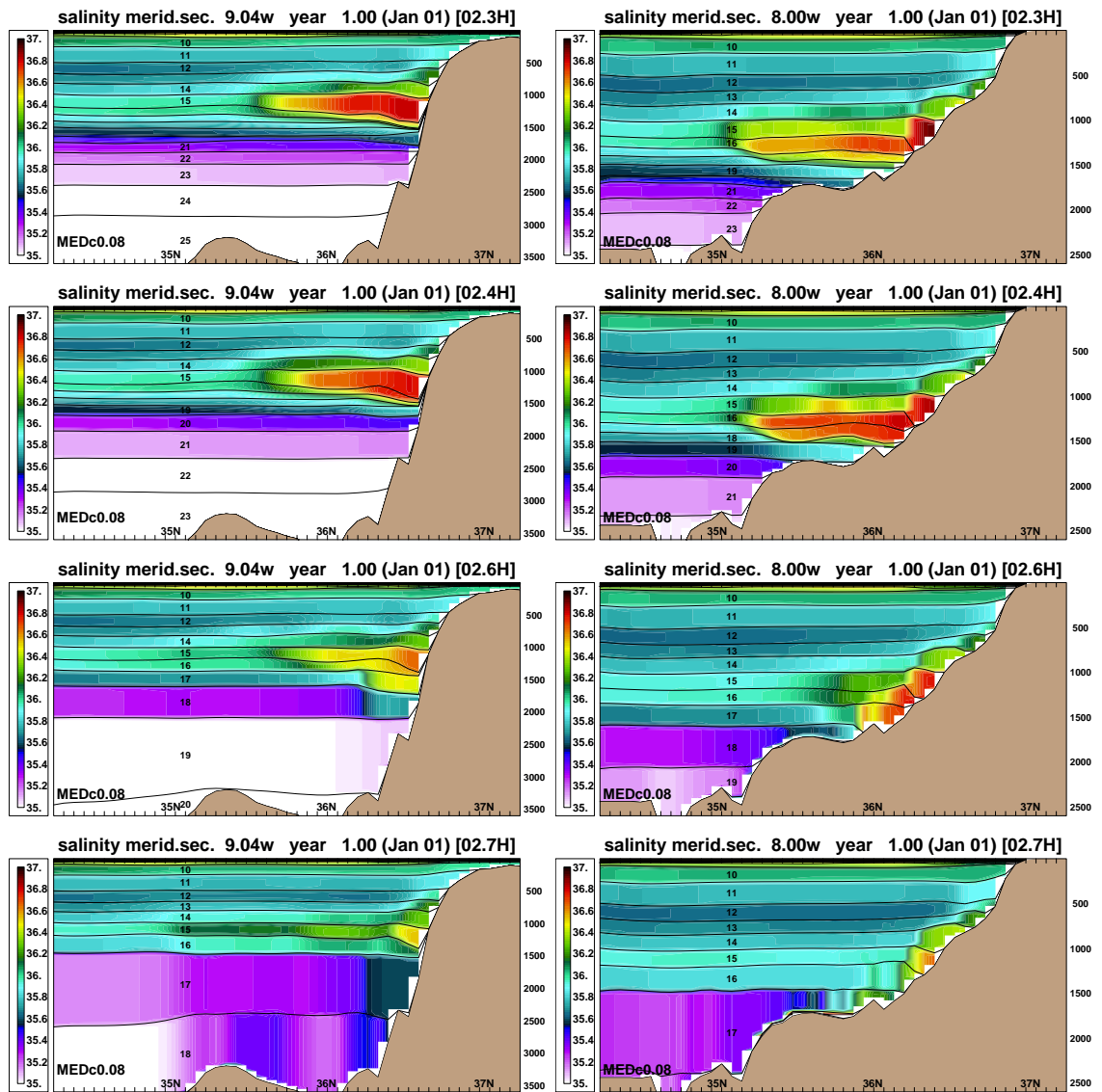


Figure 5.11: Snapshots of the salinity distribution at sections 9° (left panels) and 8° W (right panels) with different vertical resolutions. From top to bottom are experiments with 15, 13, 7, and 4 layers between the outflow source and product water.

resolution simulations tend to show slightly stronger entrainment than the lower resolution cases. This is expected because the flow is weaker in the lower resolution simulations. However, the sensitivity from the 0.08° , 0.16° , and 0.32° simulations is ‘acceptable’. Simulations with these 3 resolutions reproduce MOW that has water properties and equilibrium depths fairly consistent with the observations.

The impact of vertical resolution has also been briefly investigated. Two high-resolution experiments, with 13 and 15 layers between the outflow source and product water, show highly similar results, suggesting that the simulations are ‘robust’ as an adequate resolution is achieved. However, two low-resolution experiments show consecutively deeper intrusion of the Mediterranean outflow water, indicating the entrainment is weaker. In particular, the simulated MOW descends to the bottom when there is only 4 layers between the outflow source and product water.

Chapter 6

An evaluation of the marginal sea boundary condition

With the entrainment process parameterized, an outflow plume can be explicitly resolved in OGCMs such as HYCOM. The aim of this chapter is to evaluate an alternative approach to the explicit representation, the so-called marginal sea boundary condition (hereafter MSBC; Price and Yang, 1998). In current climate models, the horizontal resolution is typically one order of magnitude lower than that desirable for an explicit representation of outflows such as the Mediterranean or the Faroe Bank Channel. On the other hand, since the outflow water mass transformation process takes place within roughly one grid cell of a climate model, it seems appropriate from an oceanic perspective to parameterize rather than to explicitly model the outflow process. The development of MSBC is motivated by this concept of outflow parameterization. It couples a hydraulic control model of marginal sea-deep ocean exchange and a model of a rotating, entraining density current, and is capable of simulating variations in the outflow product water associated with changes in outflow source or the ambient ocean. The implementation of the MSBC in climate models

is underway at NCAR and at GFDL.

It is, however, still unclear if the MSBC is predicting realistic variations in outflow product waters. In particular, the MSBC states that the water properties of the outflow product water will be insensitive to the outflow source water change, but sensitive to the ambient ocean water change, and that the volume transport of the outflow product water is sensitive to change both in the source and ambient waters. The success of the regional HYCOM simulation discussed herein in reproducing the observed Mediterranean outflow provides an excellent setting to “evaluate” whether such statements are realistic, that is, how the predictions of the MSBC compares to the output of a series of regional HYCOM simulations with specified variations in the source and ambient waters.

6.1 Experiment configurations

Typical temperature T , salinity S , and density ρ profiles of the Mediterranean Sea and the Gulf of Cádiz are illustrated in Fig. 6.1. Dynamically the important quantity is the density contrast between the two basins, which has a maximum of $\sim 2.0 \text{ kg m}^{-3}$ at a depth comparable to the sill depth of the Strait of Gibraltar. Thus $\Delta\rho = 2.0 \text{ kg m}^{-3}$ is taken as the reference density contrast. Two sets of HYCOM experiments are designed. Each set has one reference experiment, the same as in chapter 4, and four sensitivity experiments with water property variations:

- **Outflow source water change:** T , S , and ρ fields in the Gulf of Cádiz are the same as in the reference experiment. In the Mediterranean Sea, T is the same as in the reference experiment, while ρ is shifted by a constant value ($\pm 10\%$ and $\pm 20\%$ of $\Delta\rho$), and S is then calculated from ρ and T (Fig. 6.2a).

- **Ambient ocean water change:** T, S, and ρ fields in the Mediterranean Sea are the same as in the reference experiment. In the Gulf of Cádiz, T is the same as in the reference experiment, while ρ is shifted by a constant value ($\pm 10\%$ and $\pm 20\%$ of $\Delta\rho$), and S is then calculated from ρ and T (Fig. 6.2b).

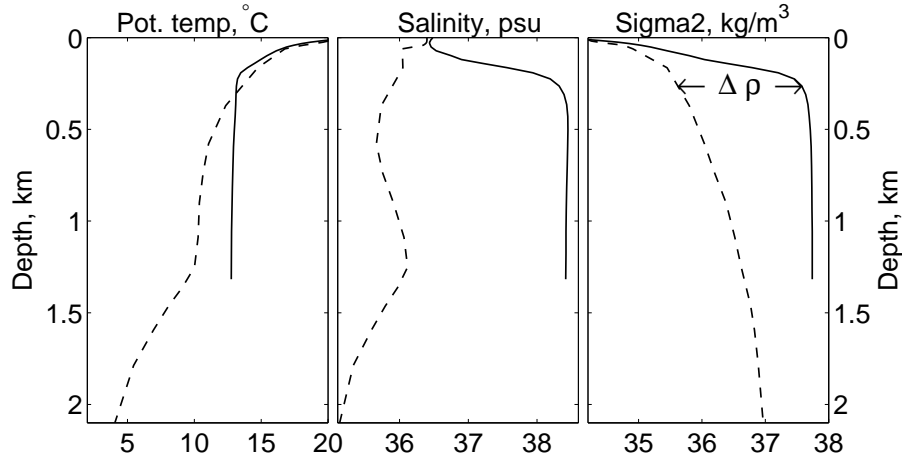


Figure 6.1: Typical temperature, salinity, and density profiles in the Mediterranean Sea (solid lines) and in the Gulf of Cádiz (dash lines). The $\Delta\rho = 2.0 \text{ kg m}^{-3}$ at 250 m marks the reference density contrast between two basins.

The MSBC simplifies the entire outflow water mass transformation processes into a side-wall boundary condition with two components (see Fig. 6.3). The first converts the surface inflow water into an outflow source water (by the conservations of mass, heat, and salt, and a hydraulic model of density-driven exchange). The second component then transforms the outflow source water into the final outflow product water. Dynamically one critical parameter is the temperature, salinity profiles of the ambient ocean (see Fig. 6.1). It describes the properties of the surface inflow water, provides properties of the entrained water, and therefore influence the outflow product water and the equilibrium depth. The other parameters are listed in Table 6.1, among them the important parameters are the heat/salt fluxes and the depth on which the entrainment takes place. We should point out here that the outflow source water in the regional model is prescribed (by using climatological data and some

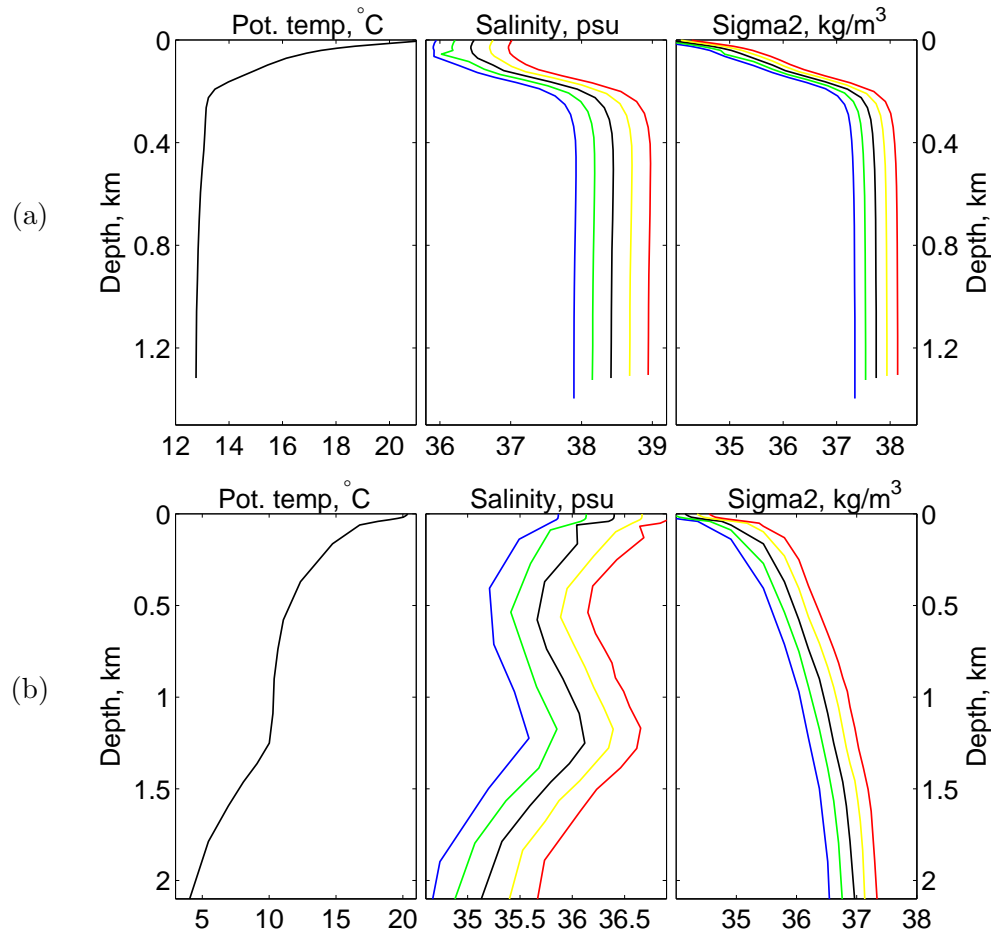


Figure 6.2: (a) the temperature, salinity, and density profiles in the Mediterranean Sea in the experiments with outflow source water change; (b) the temperature, salinity, and density profiles in the Gulf of Cádiz in the experiments with ambient ocean water change.

constant, somewhat arbitrary variance), while in MSBC it is generated by specifying the heat/salt fluxes. Varying fluxes is therefore applied in MSBC to have comparable outflow source water to that of the regional model. We also ‘tuned’ the MSBC by using a different entrainment depth, which improves the temperature comparison in particular.

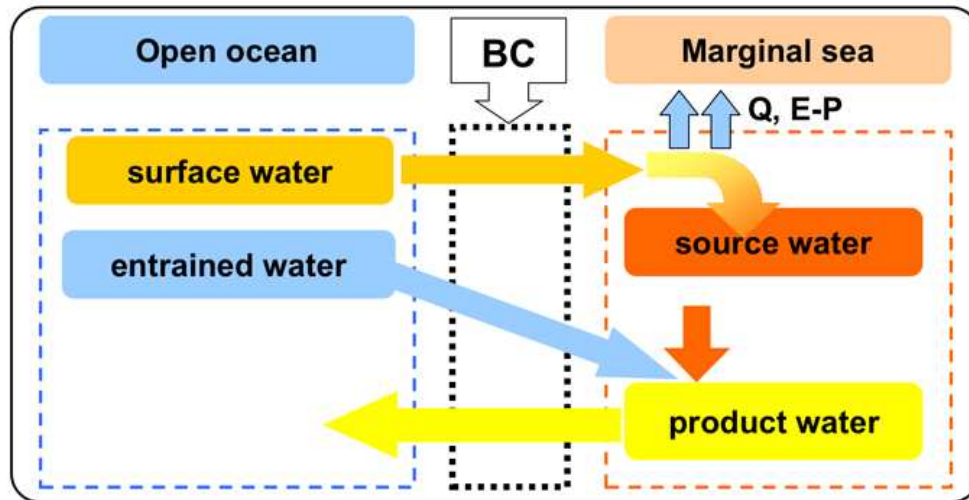


Figure 6.3: A schematic of the two components of the marginal sea boundary condition. One (a model of marginal sea-deep ocean exchange) converts the surface inflow water into an outflow source water, and the other (a model of a rotating, entraining gravity current) transforms the outflow source water into final outflow water which feeds back into deep ocean.

Table 6.1: Some external parameters of the MSBC for the Mediterranean outflow: ϕ , W , and d_s are the latitude (in $^\circ$), width (in km), and sill depth (in m) of the Strait of Gibraltar. A , Q , and $E-P$ are the area (in 10^6 km^2) of the Mediterranean Sea, heat flux (in W m^{-2} , negative indicates heat loss from the marginal sea), and evaporation minus precipitation (in m yr^{-1} , positive indicates excess evaporation). α is the slope of the continental slope. d_e is the depth (in m) on which entrainment takes place. “-” means the value is the same as in Price and Yang (1998).

	ϕ	W	d_s	A	Q	$E-P$	α	d_e
Price and Yang (1998)	36	20	300	2.5	0	0.7	0.012	400
Here	-	-	-	-	6.0 ~ 7.6	0.35 ~ 0.75	-	600

6.2 Results

6.2.1 Outflow source water change

Snapshots of salinity distributions at one meridional section in the Gulf of Cádiz are shown in Fig. 6.4. The increase of outflow source water salinity and density leads to a larger amount of Mediterranean outflow water in the gulf, with a higher value of salinity maximum. The simulated outflow water also equilibrates into slightly denser isopycnic layers at greater depth.

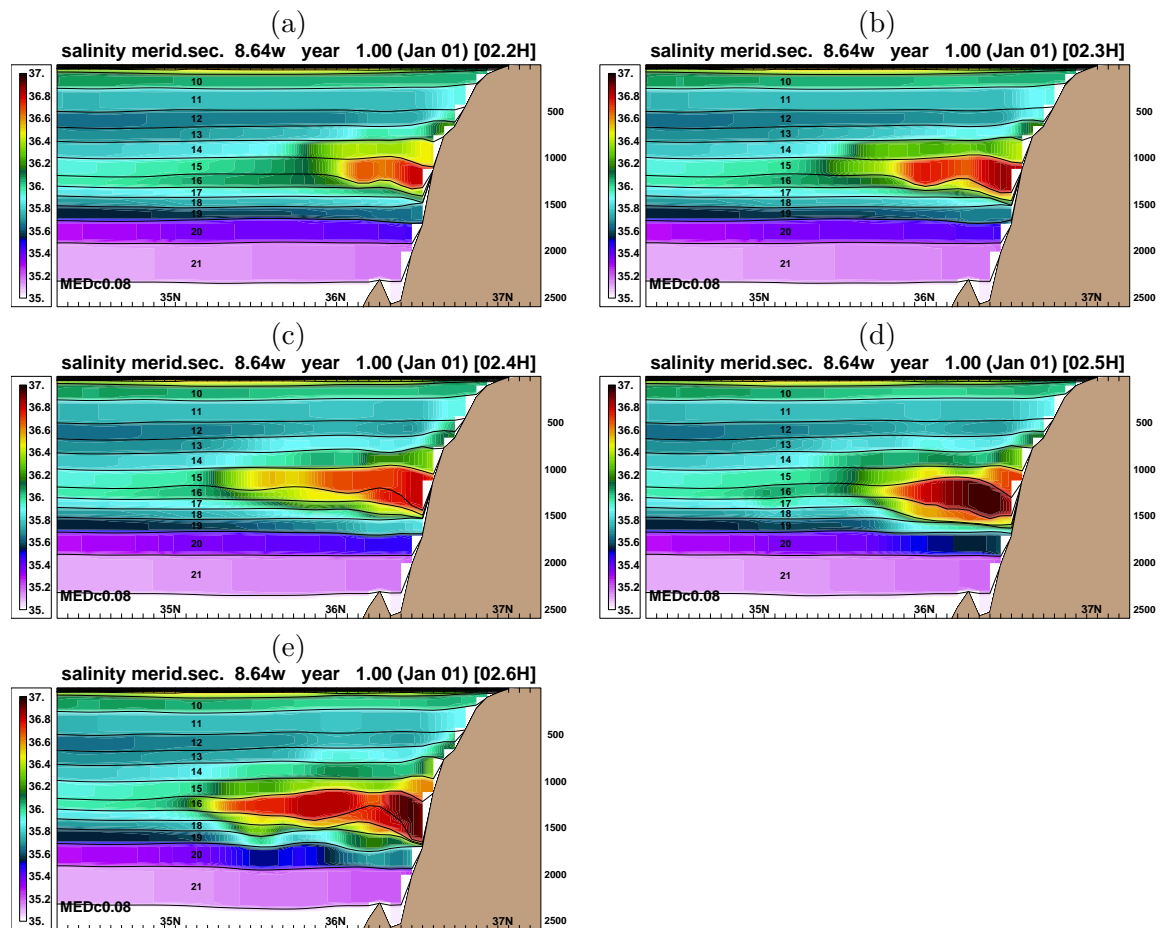


Figure 6.4: Snapshots of salinity distribution at 8.6°W . Panels (a) to (e) are the experiments in which the density of outflow source water is shifted by -20% , -10% , 0% , $+10\%$, and $+20\%$ of the $\Delta\rho$, respectively.

To quantify the evolution of the simulated MOW in the Gulf of Cádiz, we define the MOW as in Chapter 4 water mass below the NACW with salinity $S \geq \max(S_c, S_0 + \Delta S)$, in which S_0 is the initial mean salinity profile in the Gulf and ΔS and S_c are constants of 0.05 psu and 36.0 psu, respectively. Based on this definition, the volume transport Q , salinity \bar{S} , temperature \bar{T} , and depth \bar{D} of the outflow plume are calculated with

$$Q(x, t) = \int_0^W \int_{z_1}^{z_0} u \, dz \, dy; \quad (6.1)$$

$$\bar{T}(x, t) = A^{-1} \int_0^W \int_{z_1}^{z_0} T \, dz \, dy; \quad (6.2)$$

$$\bar{S}(x, t) = A^{-1} \int_0^W \int_{z_1}^{z_0} S \, dz \, dy; \quad (6.3)$$

$$\bar{D}(x, t) = 0.5 \int_0^W (z_1 + z_0) \, dy; \quad (6.4)$$

where z_0 and z_1 are the upper and lower interface of the MOW plume, W and A are the meridional span and the area of the cross section of the outflow plume. The results are shown as a function of longitude in Fig. 6.5. The increase in the outflow source water density leads to a slightly larger volume transport at the strait, to significantly more entrainment, and therefore to a greater volume transport of outflow product water. The resulting variations in temperature, salinity, and depth of the product water are not significant. It is worth mentioning that the increase in temperature east of 6.5° results from the entrainment of ambient water warmer than the source water.

A comparison of HYCOM and MSBC with outflow source water change is presented in Fig. 6.6, in which the lines are from MSBC and the five circles are HYCOM experiments and the results are plotted as a function of outflow source salinity. For HYCOM, the quantities are averaged over $9^\circ \sim 8^\circ\text{W}$ and $6^\circ \sim 5.5^\circ\text{W}$ to obtain the product and source water information, respectively. The error bars of the transport, S , and T represent the standard

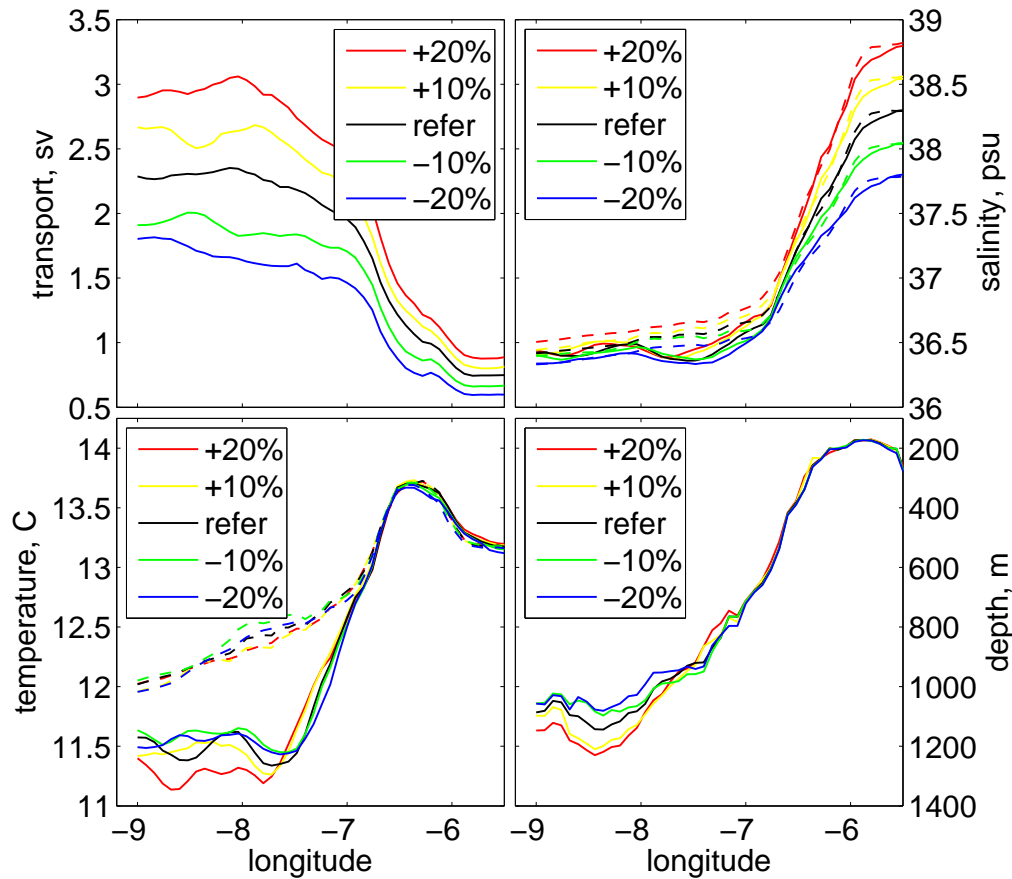


Figure 6.5: Results of HYCOM experiments with outflow source water change. The evolution of mean volume transport, salinity, temperature, and depth of the Mediterranean outflow in the Gulf of Cádiz.

deviations, while the error bar of depth marks the mean upper and lower boundary of the outflow plume. Various inputs are required for MSBC to generate the outflow source and product water. Those fixed parameters (i.e., those associated with the area of the Mediterranean Sea, the location and geometry of the strait of the Gibraltar, and slope of continental slope) are set identical to those as in Price and Yang (1998). The T/S profiles in the Gulf of Cádiz from the model, very similar to the profiles of Price and Yang (1998), are supplied as the ambient ocean water profile which leaves the heat and salt fluxes over the Mediterranean Sea the only parameters determining the outflow source water properties. Variable fluxes (an E-P of $0.35 \sim 0.75 \text{ m year}^{-1}$ and a heat flux of $6.0 \sim 7.6 \text{ W m}^{-2}$) are

therefore specified in order to have comparable outflow source water between the regional model and MSBC. Therefore, what is important is the product water, in which the MSBC produces quite similar variations to those in HYCOM. One noticeable difference is that the MSBC compared to HYCOM exhibits stronger variation in entrainment, and weaker variation in salinity.

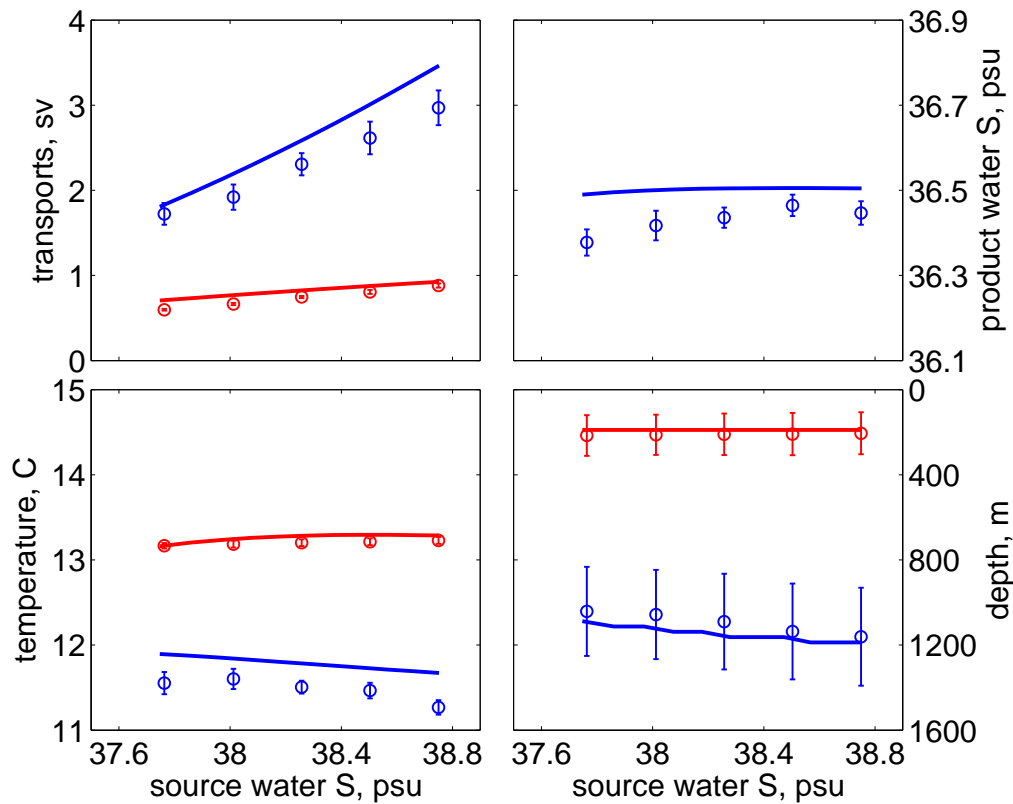


Figure 6.6: MSBC versus HYCOM with outflow source water change. Lines are from MSBC and circles are the HYCOM results. Error bars represent the standard deviation for transport, salinity and temperature, and the upper and lower interface of outflow plume for depth. The red color represents the outflow source water and blue the product water.

6.2.2 Ambient ocean water change

Salinity distribution from HYCOM experiments with ambient ocean water changes are shown in Fig. 6.7. Compared to Fig. 6.4, the salinity of the outflow product water in the gulf varies much more significantly. The magnitude of the variation (~ 1 psu) is nearly the

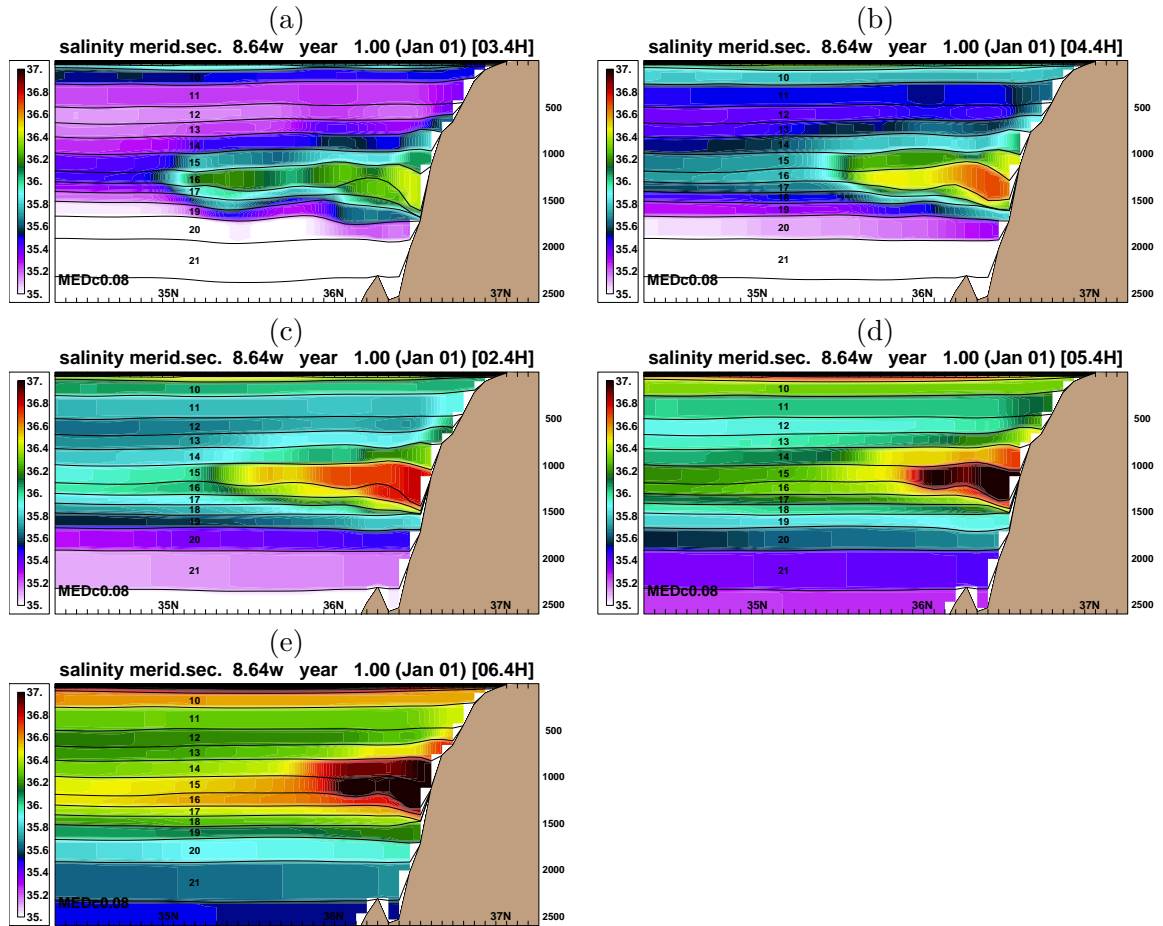


Figure 6.7: The same as Fig. 6.4 but for experiments with ambient ocean water change.

same as that of the ambient water change. As a result, the simulated MOW equilibrates at greater density but shallower depth.

To be consistent with the varying ambient ocean water profiles, the constant S_c is shifted by -0.53 , -0.265 , 0.265 , and 0.53 psu in defining the MOW in the 4 sensitivity experiments. The HYCOM simulations with ambient water changes are presented in Fig. 6.8. The increase of salinity and density in the ambient ocean water reduces the density contrast between outflow and ambient water, and a slightly smaller volume transport of outflow source water is produced. The weaker density contrast also leads to significantly less entrainment and hence a smaller transport of outflow product water. The five experiments begins with

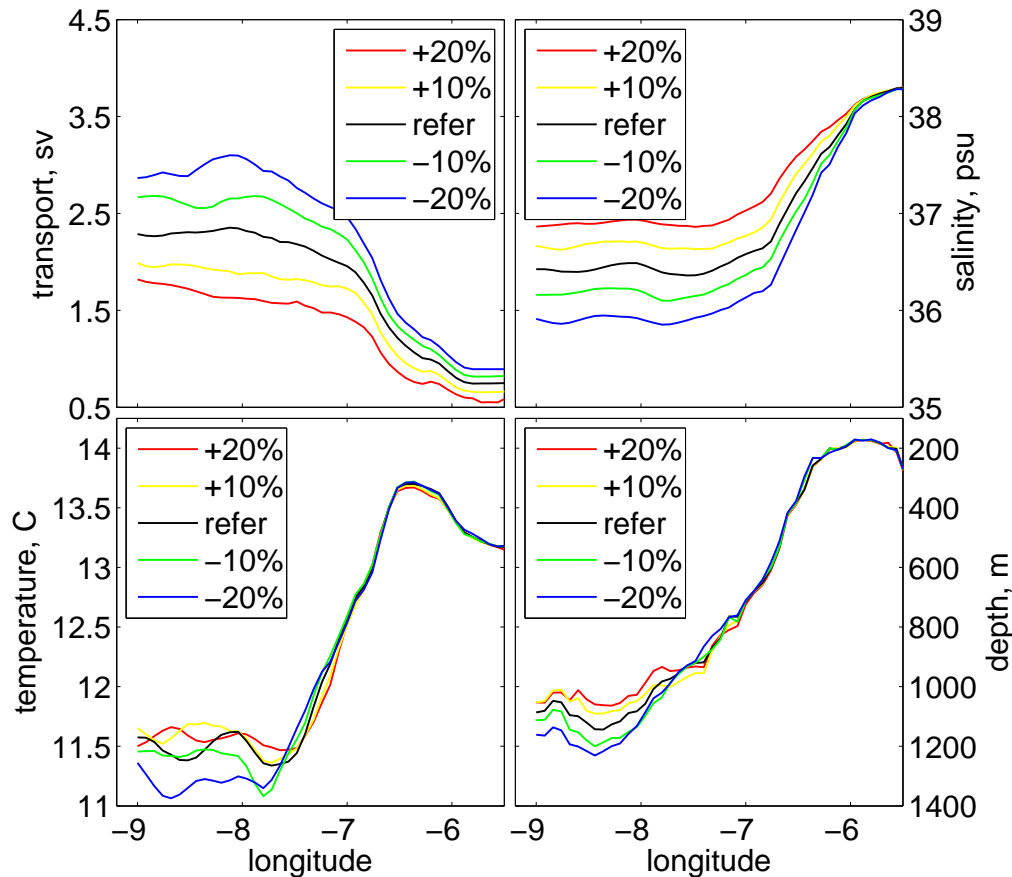


Figure 6.8: The Same as Fig. 6.5 but for experiments with ambient ocean water change.

identical salinity in the outflow source water, and end up with very different salinity in the product water. This is exactly the opposite results to experiment with source water change. The variances in temperature and depth also appear more significant than those associated with outflow source water change.

Finally, the comparison between HYCOM and MSBC with variations in ambient ocean water is summarized in Fig. 6.9, in which everything is the same as in Fig. 6.6 except that the X-axis is the variance in the density profile. Similarly, the same values of heat fluxes and E-P as in section 6.2.1 are used in MSBC. The comparison shows similar trends in the outflow product water. The increase of density in the ambient water reduces the density contrast between outflow and the ambient, which leads to weaker entrainment and smaller

volume transport of outflow product water. Weaker entrainment means less dilution to the outflow, and since the outflow begins with the same source, the salinity of the outflow product water varies more significantly than the source water change scenario. Although the trends agree quite well between HYCOM simulations and MSBC, the same amount of change in ambient water leads to a larger variation in entrainment, and stronger variations in temperature and equilibrium depth in HYCOM than in MSBC.

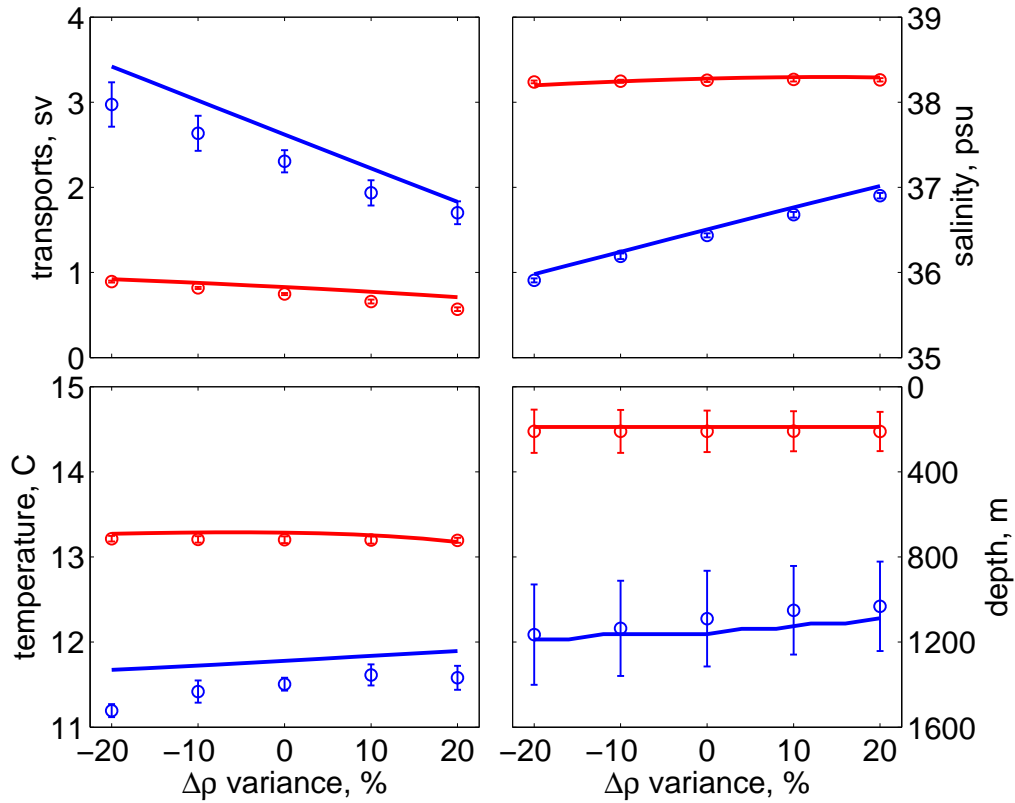


Figure 6.9: MSBC versus HYCOM with ambient ocean water change. Lines are from MSBC and circles are the HYCOM results; Error bars represent the standard deviation for transport, salinity and temperature, and the thickness of outflow plume for depth. The red and blue color represent the outflow source water and product water.

To highlight the different sensitivity of the outflow product water variation to the changes in outflow source water and ambient ocean water, we define four non-dimensional quantities, $d\ln(Q_p)/d\ln(\Delta\rho)$, $d\ln(\bar{S}_p)/d\ln(\Delta\rho)$, $d\ln(\bar{T}_p)/d\ln(\Delta\rho)$, and $d\ln(\bar{D}_p)/d\ln(\Delta\rho)$,

Table 6.2: The ratio of normalized variations of the outflow product water to that of the density contrast. Q_p , \bar{S}_p , \bar{T}_p , and \bar{D}_p are the volume transport, salinity, temperature, and equilibrium depth of the outflow product water.

	$\frac{d \ln(Q_p)}{d \ln(\Delta \rho)}$	$\frac{d \ln(\bar{S}_p)}{d \ln(\Delta \rho)}$	$\frac{d \ln(\bar{T}_p)}{d \ln(\Delta \rho)}$	$\frac{d \ln(\bar{D}_p)}{d \ln(\Delta \rho)}$	
HYCOM	1.352	0.005	-0.062	0.272	source water change
MSBC	1.599	0.001	-0.053	0.215	
HYCOM	1.376	-0.068	-0.084	0.304	ambient water change
MSBC	1.516	-0.071	-0.047	0.215	

where $\Delta \rho$ is the density contrast between outflow source and ambient, and Q_p , \bar{S}_p , \bar{T}_p , and \bar{D}_p are the volume transport, salinity, temperature, and equilibrium depth of the outflow product water. These quantities can be interpreted as the variation (normalized by its reference number) induced by the variation of density contrast. The values are summarized in Table 6.2. The most pronounced result is that the volume transport is equally sensitive to $\Delta \rho$ variation through changes in outflow source water or ambient water. The outflow salinity is at least one order more sensitive to changing ambient water than to changing outflow source water for the reason laid out above. Overall, the MSBC reproduces quantitatively the variations of the Mediterranean outflow water quite similar to that in the regional model.

6.3 Summary and discussion

In light of the growing interest in representing outflow process in low-resolution climate models, a simple parameterization has been developed by Price and Yang (1998). The parameterization, termed MSBC, collapses all the water mass transformation processes of the outflow into a sidewall boundary condition. The MSBC interestingly predicts that 1) variations of outflow source water should lead to a significant change in the strength of the entrainment and hence in the volume transport of the product water, while the water

properties of the product water are insensitive to the corresponding change in the source water. 2) Variations of ambient ocean water lead to significant changes in volume transport and water properties of the outflow product water.

To evaluate these predictions, two sets of regional simulations have been conducted using HYCOM with a horizontal resolution of 0.08° . The comparison of HYCOM and MSBC suggests that, while the MSBC does not resolve any detailed aspects of the outflow plume, it produces realistic variations of outflow product water associated with changes in both the outflow source water and ambient ocean water. Therefore, the MSBC appears as an attractive approach to representing outflow in very coarse resolution climate models.

The reason why the outflow product water properties are more sensitive to changes in the ambient ocean water than in the outflow source water is due to the variations of entrainment. When the Mediterranean outflow source water becomes saltier and denser, the density contrast is increased, which leads to more entrainment. Both factors result in more dilution, which works as a negative feed-back to cancel the variation in outflow source water. On the other hand, when the ambient ocean water becomes saltier and denser, the reduced density contrast results in less entrainment, or less dilution, which directly affects the water properties since the outflow begins with the same source.

Chapter 7

Conclusions

Motivated by the fact that the dense water outflows from high latitude and marginal seas play an important role in the large scale ocean circulation and therefore in Earth's climate, the primary objective of the present work is to investigate the representation of outflows in an oceanic general circulation model (OGCM). This investigation was carried out within the framework of the hybrid coordinate ocean model (HYCOM). The challenge of outflow representations in OGCMs lies not only in the high computational cost of resolving the small topographic details associated with outflow but also in the difficulty of accurately prescribing the entrainment process, which ultimately determines the volume transport and water properties of the final outflow product water. The research is therefore focused on the parameterization of entrainment and mixing process. First, two different diapycnal mixing parameterizations in HYCOM are compared using idealized configurations. A new algebraic entrainment parameterization is then derived for HYCOM in Chapter 3, based on a comparison with simulations of a high-resolution, nonhydrostatic model. The application of this parameterization in a realistic regional simulation of the Mediterranean outflow, and the sensitivity to model resolution, are investigated and discussed in Chapters 4 and 5. An

alternative approach of outflow representation for climate models is explored in Chapter 6. The principal results are reviewed in this concluding section, and their significance both to ocean modeling and to the understanding of outflow in large-scale ocean is discussed.

Different approaches are used to implement diapycnal mixing in HYCOM, when the model is configured in a hybrid or in a purely isopycnic coordinate system. In hybrid coordinates, the diapycnal mixing modifies the vertical density profile, while in isopycnic coordinates, it modifies the thickness of specific isopycnals. One-dimensional diffusion experiments with constant diffusivities suggest that these different approaches lead to similar results and that both are consistent with analytical solutions.

Using an idealized ‘dam-break’ configuration, the physics and performance of two mixing parameterizations (KPP and TP) in representing the shear-induced entrainment mixing in outflow are compared. Large differences are found. TP produces much stronger entrainment than KPP because of a much higher value of effective diffusivity. This result agrees with those of Chang et al. (2005), who conclude that KPP produces entrainment which is too weak while TP is the opposite, and that both parameterizations need to be changed significantly in order for them to match the simulations of a high-resolution, nonhydrostatic model. The weak entrainment in KPP is primarily due to a hard limit of K_{max} in the interior mixing that is inappropriate for outflow entrainment. A constant value of K_{max} also does not allow the strength of the mixing to vary with the corresponding forcing. The excessive mixing in TP is mainly results from the inconsistency between the layer Richardson number Ri_k in HYCOM and the bulk Richardson number Ri_B in a one-layer, stream tube concept of outflow plume. The layer Ri_k effectively becomes a shear Richardson number since the isopycnic coordinate model has high vertical resolution in the pycnocline between the outflow and ambient water.

Based on the work of Turner (1986) and Hallberg (2000), a new algebraic parameterization is developed for HYCOM. It casts the entrainment velocity as a function of the layer Richardson number Ri_k times the velocity difference across layers, ΔU . This formulation is consistent with Buckingham's Pi-Theorem (e.g. Kundu, 1990) which implies that constants in a physical law should be dimensionless, and with the physical property of stratified flows that the interfacial shear is the dominant energy source for turbulence mixing. In order to determine the Ri -dependent function, we compare the simulated gravity current flowing over a constant bottom slope in the relatively low-resolution, hydrostatic model HYCOM to that in the high-resolution, nonhydrostatic spectral element model Nek5000. A simple linear function, $E = 0.20 \times (1 - Ri/0.25)$, is found to reproduce the entrainment, salt flux, Richardson number, velocity profiles, and plume propagation speed from Nek5000 quite well. The parameterization, though radically simple, is consistent with the fundamental theoretical and laboratory results from stably-stratified shear flows that the shear-induced turbulence grows (decays) in the regime of $Ri < 0.25$ ($Ri > 0.25$).

To evaluate the performance of the entrainment parameterization in simulations of realistic outflows, a regional HYCOM simulation of the Mediterranean outflow with a horizontal resolution of 0.08° is conducted, and the numerical results are compared with field data obtained in the Gulf of Cádiz Expedition (1988). The simulation reproduces the observed MOW in the Gulf quite well, including the evolution of temperature, salinity, and velocity profiles, the steering and spreading of the outflow plume as it descends along the continental slope, the transition of plume behavior from a bottom-trapped density current to a wall-bounced undercurrent, and, most importantly, the localization of entrainment immediately west of the strait where the outflow water experiences a significant modification both in

volume transport and in water properties. This localization of the entrainment is associated with the descent of the outflow. It has also been observed in the outflow plume of the Denmark Strait (e.g. Girton and Sanford, 2003), and appears in stream tube models as a consequence of a momentum balance between buoyancy force and bottom and entrainment stresses (Price and Baringer, 1994).

Regional, basin-scale, and climate models are typically run at different horizontal resolutions. Without question the representation of topography plays an important role in ocean modeling in general, and especially in simulating outflows. This is so because the outflows are bottom-trapped plumes that flow across the isobaths. The entrainment prescribed by the same parameterization also varies in configurations with different resolution. Coarse resolution simulations tend to have weaker entrainment than the high resolution ones. This is mainly because the flows are weaker, therefore the shear and Ri is less well-resolved as the resolution decreases. Not surprisingly, the vertical resolution is more critical, and the entrainment parameterization does not work properly in configurations with very coarse vertical resolution.

A general conclusion arising from these idealized and realistic HYCOM simulations is that HYCOM can simulate observed outflow plumes well given sufficient resolution and a realistic parameterization of the entrainment. The lack of horizontal resolution, however, make this explicit approach of outflow representation a real challenge for climate models. An alternative solution is to simplify the entire water mass transformation processes of outflow into the marginal sea boundary condition (MSBC). Two sets of sensitivity experiments aimed at climate variation scenarios are carried out, and the results are used to evaluate the performance of MSBC. It is shown that, although MSBC does not resolve the details of the outflow plume in contrast to the regional HYCOM simulation, it reproduces comparable

results in terms of variations in product water of the Mediterranean outflow associated the source and ambient water property changes. In particular, variations of the ambient ocean water properties have a greater impact on the outflow product water properties than variations of the outflow source water.

Bibliography

Bibliography

- Ambar, I., 1983. A shallow core of Mediterranean Water off Western Portugal. *Deep Sea Res.* 30, 677–680.
- Ambar, I., Howe, M. R., 1979a. Observations of the Mediterranean outflow. I. Mixing in the Mediterranean outflow. *Deep Sea Res.* 26A, 535–554.
- Ambar, I., Howe, M. R., 1979b. Observations of the Mediterranean outflow. II. The deep circulation in the vicinity of the Gulf of Cadiz. *Deep Sea Res.* 26A, 555–568.
- Ambar, I., Serra, N., Brogueira, M. J., Cabeçadas, G., Abrantes, F., Freitas, P., Gonçalves, C., Gonzalez, N., 2002. Physical, chemical and sedimentological aspects of the Mediterranean outflow off Iberia. *Deep Sea Res. II* 49, 4163–4177.
- Baringer, M. O., 1993. Mixing and dynamics of the Mediterranean outflow. Whoi-93-52, 244 pp, Woods Hole Oceanographic Institution/ Massachusetts Institute of Technology, Cambridge, MA, available from Woods Hole Oceanographic Institute, Woods Hole, MA 02543.
- Baringer, M. O., Price, J. F., 1997a. Mixing and spreading of the Mediterranean outflow. *J. Phys. Oceanogr.* 27, 1654–1677.
- Baringer, M. O., Price, J. F., 1997b. Momentum and energy balance of the Mediterranean outflow. *J. Phys. Oceanogr.* 27, 1678–1692.
- Beckmann, A., Haidvogel, D. B., 1993. Numerical simulation of flow around a tall isolated seamount. Part I: Problem formulation and model accuracy. *J. Phys. Oceanogr.* 23, 1736–1753.
- Bleck, R., 1978. Finite difference equations in generalized vertical coordinates. Part I: Total energy conservation. *Contrib. Atmos. Phys.* 51, 360–372.
- Bleck, R., 2002. An oceanic general circulation model framed in hybrid isopycnic-Cartesian coordinates. *Ocean Modelling* 37, 55–88.
- Bleck, R., Benjamin, S., 1993. Regional weather prediction with a model combining terrain-following and isentropic coordinates. Part I: Model description. *Mon. Wea. Rev.* 121, 1770–1785.
- Bleck, R., Boudra, D. B., 1981. Initial testing of a numerical ocean circulation model using a hybrid (quasi-isopycnic) vertical coordinate. *J. Phys. Oceanogr.* 11, 755–770.

- Bleck, R., Rooth, C., Hu, D., Smith, L., 1992. Salinity-driven thermocline transients in a wind- and thermohaline-forced isopycnic coordinate model of the North Atlantic. *J. Phys. Oceanogr.* 22, 1486–1505.
- Bleck, R., Smith, L., 1990. A wind-driven isopycnic coordinate model of the north and equatorial Atlantic Ocean. 1. Model development and supporting experiments. *J. Geophys. Res.* 95C, 3273–3285.
- Bower, A., Serra, N., Ambar, I., 2002a. Structure of the Mediterranean undercurrent and Mediterranean water spreading around the southwestern Iberian Peninsula. *J. Geophys. Res.* 107 (C10).
- Bower, A. S., Armi, L., Ambar, I., 1997a. Lagrangian observations of meddy formation during a Mediterranean Undercurrent seeding experiment. *J. Phys. Oceanogr.* 27, 2545–2575.
- Bower, A. S., Cann, B. L., Rossby, T., Zenk, W., Gould, J., Speer, K., Richardson, P. L., Prater, M. D., Zhang, H.-M., 2002b. Directly measured mid-depth circulation in the northeastern North Atlantic Ocean. *Nature* 419, 603–607.
- Bower, A. S., Pallant, J., Chandler, C. L., 1997b. A Mediterranean Undercurrent Seeding Experiment (AMUSE): Part I: Program description and hydrographic measurements. Tech. rep., Woods Hole Oceanographic Institution, Woods Hole, Massachusetts.
- Britter, R. E., Linden, P. F., 1980. The motion of the front of a gravity current traveling down an incline. *J. Fluid Mech.* 99, 531–543.
- Bryden, H. L., Candela, J. C., Kinder, T. H., 1994. Exchange through the Strait of Gibraltar. *Progr. Oceanogr.* 33, 201–248.
- Candela, J., 2001. Mediterranean water and global circulation. In: Siedler, G., Church, J., Gould, J. (Eds.), *Ocean Circulation and Climate*. Academic Press, New York, pp. 419–429.
- Chang, Y., Xu, X., Özgökmen, T., Chassignet, E. P., Peters, H., Fischer, P. F., 2005. Comparison of gravity current mixing parameterizations and calibration using a high-resolution 3D nonhydrostatic spectral element model. *Ocean Modelling* 10, 342–368.
- Chassignet, E. P., Arango, H., Dietrich, D., Ezer, T., Ghil, M., Haidvogel, D. B., Ma, C.-C., Mehra, A., Paiva, A. M., Sirkes, Z., 2000. DAMEE-NAB: The base experiments. *Dynamics of the Atmosphere and Oceans* 32, 155–184.
- Chassignet, E. P., Smith, L. T., Halliwell, G. R., Bleck, R., 2003. North Atlantic simulations with the hybrid coordinate ocean model (HYCOM): impact of the vertical coordinate choice, reference pressure, and thermobaricity. *J. Phys. Oceanogr.* 33, 2504–2526.
- Chérubin, L., Carton, X., Paillet, J., Morel, Y., Serpette, A., 2000. Instability of the Mediterranean water undercurrents southwest of Portugal: effects of baroclinicity and of topography. *Oceanologica Acta* 23(5), 551–573.

- Chu, P. C., Fan, C., 1997. Sixth-order difference scheme for sigma coordinate ocean models. *J. Phys. Oceanogr.* 27, 2064–2071.
- Curry, R. G., McCartney, M. S., Joyce, T. M., 1998. Oceanic transport of subpolar climate signals to mid-depth subtropical waters. *Nature* 391, 575–577.
- Daniault, N., Maze, J. P., Arhan, M., 1994. Circulation and mixing of Mediterranean water west of the Iberian Peninsula. *Deep Sea Res.* 41, 1685–1714.
- DYNAMO Group, 1997. DYNAMO, Dynamics of North Atlantic Models: simulation and assimilation with high resolution models. Tech. rep., Inst. Für Meereskunde and Christian-Albrechts Universität, Kiel, Germany.
- Ellison, T. H., Turner, J. S., 1959. Turbulent entrainment in stratified flows. *J. Fluid Mech.* 6, 423–448.
- Fischer, P. F., 1997. An overlapping Schwarz method for spectral element solution of the incompressible Navier-Stokes equations. *J. of Comp. Phys.* 133, 84–101.
- Fischer, P. F., Miller, N. I., Tufo, H. M., 2000. An overlapping Schwarz method for spectral element simulation of three-dimensional incompressible flows. In: Björstad, P., Luskin, M. (Eds.), *Parallel Solution of Partial Differential Equations*. Springer-Verlag, pp. 159–181.
- Fischer, P. F., Mullen, J. S., 2001. Filter-based stabilization of spectral element methods. *Comptes rendus de l'Académie des sciences Paris*, t. 332, -Série I - Analyse numérique, 265–270.
- Gawarkiewicz, G., Chapman, D. C., 1995. A numerical study of dense water formation and transport on a shallow sloping continental shelf. *J. Geophys. Res.* 100, 4489–4507.
- Girton, J. B., Sanford, T. B., 2003. Descent and modification of the overflow plume in the Denmark Strait. *J. Phys. Oceanogr.* 33, 1351–1363.
- Girton, J. B., Sanford, T. B., Käse, R. H., 2001. Synoptic sections of the Denmark Strait Overflow. *Geophys. Res. Lett.* 28, 1619–1622.
- Gordon, A., Zambianchi, E., Orsi, A., Visbeck, M., Giulivi, C., III, T. W., Spezie, G., 2004. Energetic plumes over the western Ross Sea continental slope. *Geophys. Res. Lett.* 31, L21302.
- Gregg, M. C., Peters, H., Wesson, J. C., Oakey, N. S., Shay, T. S., 1985. Intensive measurements of turbulence and shear in the equatorial undercurrent. *Nature* 318, 140–144.
- Griffies, S. M., Pacanowski, R. C., Hallberg, R. W., 2000. Spurious diapycnal mixing associated with advection in a z-coordinate ocean model. *Mon. Weather Rev.* 128, 538–564.
- Hallberg, R., 2000. Time integration of diapycnal diffusion and Richardson number dependent mixing in isopycnal coordinate ocean models. *Mon. Weath. Rev.* 128, 1402–1419.

- Halliwel, G. R., 2004. Evaluation of vertical coordinate and vertical mixing algorithms in the HYbrid-Coordinate Ocean Model (HYCOM). *Ocean modeling* 7, 285–322.
- Haney, R., 1991. On the pressure-gradient force over step topography in sigma coordinate ocean models. *J. Phys. Oceanogr.* 21, 610–619.
- Hopkins, T. S., 1978. Physical processes in the Mediterranean basins. In: Kjerve, B. (Ed.), *Estuarine Transport Processes*. University of South Carolina Press, pp. 269–310.
- Hunt, H. D., Wooding, C. M., Chandler, C. L., Bower, A. S., 1998. A Mediterranean Undercurrent Seeding Experiment (AMUSE): Part II: RAFOS float data report May 1993 - March 1995. Tech. rep., Woods Hole Oceanographic Institution, Woods Hole, Massachusetts.
- Iorga, M. C., Lozier, M. S., 1999a. Signatures of the Mediterranean outflow from a North Atlantic climatology 1. salinity and density fields. *J. Geophys. Res.* 104, 25985–26009.
- Iorga, M. C., Lozier, M. S., 1999b. Signatures of the Mediterranean outflow from a North Atlantic climatology 2. diagnostic velocity fields. *J. Geophys. Res.* 104, 26011–26029.
- Janjić, Z. I., 1977. Pressure gradient force and advection scheme used for forecasting with steep and small scale topography. *Contributions in Atmospheric Physics* 50, 186–199.
- Jiang, L., Garwood, R. W., 1995. A numerical study of three-dimensional bottom plumes on a southern ocean continental slope. *J. Geophys. Res.* 100, 18,471–18,488.
- Johnson, G. C., Sanford, R. G. L. T. B., 1994. Stress on the Mediterranean outflow plume. Part II: turbulent dissipation and shear measurement. *J. Phys. Oceanogr.* 24, 2084–2092.
- Johnson, G. C., Sanford, T. B., Baringer, M. O., 1994. Stress on the Mediterranean outflow plume. Part I: velocity and water property measurement. *J. Phys. Oceanogr.* 24, 2072–2083.
- Jungclauss, J. H., Backhaus, J. O., 1994. Application of a transient reduced gravity plume model to the Denmark Strait Overflow. *J. Geophys. Res.* 99, 12,375–12,396.
- Jungclauss, J. H., Mellor, G., 2000. A three-dimensional model study of the Mediterranean outflow. *J. Mar. Syst.* 24, 41–66.
- Käse, R. H., Girton, J. B., Sanford, T. B., 2003. Structure and variability of the Denmark Strait Overflow: Model and observations. *J. Geophys. Res.* 108 (C6).
- Käse, R. H., Oschlies, A., 2000. Flow through Denmark Strait. *J. Geophys. Res.* 105, 28,527–28,546.
- Kenyon, N. H., Belderson, R. H., 1973. Bed forms of the Mediterranean undercurrent observed with side-scan sonar. *Sediment. Geol.* 9, 77–99.
- Keulegan, G. H., 1958. The motion of saline fronts in still water. Tech. Rep. 5831, U.S. Nat. Bur. Stand.

- Killworth, P. D., 1977. Mixing on the Weddell Sea continental slope. *Deep Sea Res.* 24, 427–448.
- Krauss, W., Käse, R. H., 1998. Eddy formation in the Denmark Strait overflow. *J. Geophys. Res.* 103, 15,525–15,538.
- Kundu, P. K., 1990. *Fluid Mechanics*. Academic Press, Inc, San Diego, California.
- Lacombe, H., Richez, C., 1982. The regime of the strait of Gibraltar. In: Nihoul, J. C. J. (Ed.), *Hydrodynamics of Semi-Enclosed Seas*. Vol. 34. Elsevier Oceanography Series, pp. 13–73.
- Large, W. G., 1998. Modeling and parameterizing ocean planetary boundary layer. In: Chassignet, E., Verron, J. (Eds.), *Ocean Modelling and Parameterization*. Kluwer, pp. 45–80.
- Large, W. G., Danabasoglu, G., Doney, S. C., McWilliams, J. C., 1997. Sensitivity to surface forcing and boundary layer mixing in a global ocean model: annual-mean climatology. *J. Phys. Oceanogr.* 27, 2418–2447.
- Large, W. G., Gent, P. R., 1999. Validation of vertical mixing in an equatorial ocean model using large eddy simulations and observations. *J. Phys. Oceanogr.* 29, 449–464.
- Large, W. G., McWilliams, J. C., Doney, S. C., 1994. Ocean vertical mixing: a review and a model with a nonlocal boundary layer parameterization. *Rev. Geophys.* 32, 363–403.
- Lazier, J. R. N., 1973. The renewal of Labrador Sea Water. *Deep Sea Res.* 20, 341–353.
- Lee, A., Ellett, E., 1965. On the contribution of overflow water from the Norwegian Sea to the hydrographic structure of the North Atlantic Ocean. *Deep Sea Res.* 12, 129–142.
- Levitus, S., Boyer, T., 1994. *World Ocean Atlas 1994 Volume 4: Temperature*. NOAA Atlas NESDIS 4. U.S. Dep. of Commerce, Washington, D.C.
- Madelain, F., 1970. Influence de la topographie du fond sur l'écoulement Méditerranée entre le Détroit de Gibraltar et le Cap Saint-Vincent. *Cahiers Oceanographiques* 22, 43–61.
- Marshall, J., Schott, F., 1999. Open-ocean convection: Observation, theory, and models. *Rev. Geophys.* 37, 1–64.
- McCartney, M. S., Mauritzen, C., 2001. On the origin of the warm inflow to the Nordic Seas. *Prog. Oceanogr.* 51, 125–214.
- McDowell, S. E., Rossby, H. T., 1978. Mediterranean Water: An intense mesoscale eddy off the Bahamas. *Science* 202, 1085–1087.
- Mellor, G. L., Ezer, T., Oey, L.-Y., 1994. The pressure gradient conundrum of sigma coordinate ocean models. *Journal of Atmospheric and Oceanic Technology* 11, 1126–1134.

- Mellor, G. L., Ezer, T., Oey, L.-Y., 1998. Sigma coordinate pressure gradient errors and the seamount problem. *Journal of Atmospheric and Oceanic Technology* 15, 1122–1131.
- Mellor, G. L., Yamada, 1982. Development of a turbulence closure model for geophysical fluid problems. *Rev. Geophys. Space Phys.* 20, 851–875.
- Mesinger, F., 1982. On the convergence and error problems of the calculation of the pressure gradient force in sigma coordinate models. *Geophysical and Astrophysical Fluid Dynamics* 19, 105–117.
- Miles, J. W., 1961. On the stability of heterogeneous shear flows. *J. Fluid Mech.* 10, 496–508.
- Molinari, R. L., Fine, R. A., Wilson, W. D., Curry, R. G., Abell, J., McCartney, M. S., 1998. The arrival of recently formed Labrador Sea Water in the deep western boundary current at 26.5°N. *Geophys. Res. Lett.* 25, 2249–2252.
- Narimousa, S., Fernando, H. J. S., 1987. On the sheared density interface of an entraining stratified fluid. *J. Fluid. Mech.* 174, 1–22.
- Ochoa, J., Bray, N. A., 1991. Water mass exchange in the Gulf of Cadiz. *Deep Sea Res.* 38, suppl. 1, S465–S503.
- Özgökmen, T. M., Chassignet, E., 2002. Dynamics of two-dimensional turbulent bottom gravity currents. *J. Phys. Oceanogr.* 32, 1460–1478.
- Özgökmen, T. M., Fischer, P., Duan, J., Iliescu, T., 2004a. Entrainment in bottom gravity currents over complex topography from three-dimensional nonhydrostatic simulations. *Geophys. Res. Lett.* 31.
- Özgökmen, T. M., Fischer, P., Johns, W. E., 2005. Product water mass formation by turbulent density currents from a high-order nonhydrostatic spectral element model. *Ocean Modelling* 12, 237–267.
- Özgökmen, T. M., Fischer, P. F., Duan, J., Iliescu, T., 2004b. Three-dimensional turbulent bottom density currents from a high-order nonhydrostatic spectral element model. *J. Phys. Oceanogr.* 34 (9), 2006–2026.
- Pacanowski, R. C., Philander, S. G. H., 1981. Parameterization of vertical mixing in numerical models of the tropical oceans. *J. Phys. Oceanogr.* 11, 1443–1451.
- Papadakis, M. P., Chassignet, E. P., Hallberg, R. W., 2003. Numerical simulations of the Mediterranean Sea outflow: Impact of the entrainment parameterization in an isopycnic coordinate model. *Ocean Modeling* 5, 325–356.
- Peters, H., Gregg, M. C., Toole, J. M., 1988. On the parameterization of equatorial turbulence. *J. Geophys. Res.* 93, 1199–1218.
- Peters, H., Johns, W. E., 2005. Mixing and entrainment in the Red Sea outflow plume. Part II: turbulence characteristics. *J. Phys. Oceanogr.* 35, 584–600.

- Peters, H., Johns, W. E., Bower, A. S., Fratantoni, D. M., 2005. Mixing and entrainment in the Red Sea outflow plume. Part I: plume structure. *J. Phys. Oceanogr.* 35, 569–583.
- Pickart, R. S., Spall, M. A., Ribergaard, M. H., Moore, G. W. K., Milliff, R. F., 2003a. Deep convection in the Irminger Sea forced by the Greenland tip jet. *Nature* 424, 152–156.
- Pickart, R. S., Straneo, F., Moore, G. W. K., 2003b. Is Labrador Sea Water formed in the Irminger Basin. *Deep Sea Res.* 50, 23–52.
- Price, J. F., 2004. A process study of the Faroe Bank Channel overflow. *Geophys Res. Abstracts*, 6, 07788.
- Price, J. F., Baringer, M. O., 1994. Outflows and deep water production by marginal seas. *Prog. Oceanogr.* 33, 161–200.
- Price, J. F., Baringer, M. O., Lueck, R. G., Johnson, G. C., Ambar, I., Parrilla, G., Cantos, A., Kennelly, M. A., Sanford, T. B., 1993. Mediterranean outflows and dynamics. *Science* 259, 1277–1282.
- Price, J. F., Yang, J., 1998. Marginal sea overflows for climate simulations. In: Chassignet, E., Verron, J. (Eds.), *Ocean Modelling and Parameterization*. Kluwer, pp. 155–170.
- Reid, J. L., 1979. On the contribution of the Mediterranean Sea outflow to the Norwegian-Greenland Sea. *Deep Sea Res. Part A*, 26, 1199–1223.
- Reid, J. L., 1994. On the total geostrophic circulation of the North Atlantic Ocean. *Prog. Oceanogr.* 33, 1–99.
- Rhein, M., Fischer, J., Smethie, W. M., Wright, D. S., Wess, R. F., Mertens, C., Min, D. H., Fleischmann, U., Putzka, A., 2002. Labrador Sea Water: Pathways, CFC inventory and formation rates. *J. Phys. Oceanogr.* 32, 648–665.
- Rhein, M., Hinrichsen, H. H., 1993. Modification of Mediterranean Water in the Gulf of Cadiz, studied with hydrographic, nutrient and chlorofluoromethane data. *Deep Sea Res.* 40, 267–291.
- Rohr, J. J., Itsweire, E. C., Helland, K. N., Atta, C. V., 1988. Growth and decay of turbulence in stably stratified shear flow. *J. Fluid Mech.* 195, 77–111.
- Serra, N., Ambar, I., Käse, R. H., 2005. Observations and numerical modelling of the Mediterranean outflow splitting and eddy generation. *Deep Sea Res. II* 52, 383–408.
- Smith, P. C., 1975. A streamtube model for bottom boundary currents in the ocean. *Deep Sea Res.* 22, 853–873.
- Song, Y. T., Wright, D. G., 1998a. A general pressure gradient formulation for ocean models. Part I: scheme design and diagnostic analysis. *Monthly Weather Review* 126, 3213–3230.
- Song, Y. T., Wright, D. G., 1998b. A general pressure gradient formulation for ocean models. Part I: scheme design and diagnostic analysis. *Corrigendum. Monthly Weather Review* 128, 2608–2609.

- Song, Y. T., Wright, D. G., 1998c. A general pressure gradient formulation for ocean models. Part II: energy, momentum, and bottom torque consistency. *Monthly Weather Review* 126, 3231–3247.
- Spall, M. A., Price, J. F., 1998. Mesoscale variability in Denmark Strait: The PV overflow hypothesis. *J. Phys. Oceanogr.* 28, 1598–1623.
- Sy, A., Rhein, M., Lazier, J. R. N., Koltermann, K. P., Meincke, J., Putzka, A., Bersch, M., 1997. Surprisingly rapid spreading of newly formed intermediate waters across the North Atlantic Ocean. *Nature* 386, 675–679.
- Talley, L. D., McCartney, M. S., 1982. Distribution and circulation of Labrador Sea Water. *J. Phys. Oceanogr.* 12, 1189–1205.
- The Lab Sea Group, 1998. The Labrador Sea deep convection experiment. *Bulletin of the American Meteorological Society* 79, 2033–2058.
- Tufo, H. M., Fischer, P. F., 1999. Terascale spectral element algorithms and implementations. Gordon Bell prize submission. In: *Proc. of the ACM/IEEE SC99 Conf. on High Performance Networking and Computing*, CDROM. IEEE Computer Soc.
- Turner, J. S., 1986. The development of the entrainment assumption and its application to geophysical flows. *J. Fluid Mech.* 173, 431–471.
- Wang, D., Large, W. G., McWilliams, J. C., 1996. Diurnal cycling, eddy viscosity and horizontal rotation effects in equatorial ocean boundary layers. *J. Geophys. Res.* 101, 3649–3662.
- Wang, D., McWilliams, J. C., Large, W. G., 1998. Large eddy simulations of the diurnal cycle of deep equatorial turbulence. *J. Phys. Oceanogr.* 28, 129–148.
- Wesson, J. C., Gregg, M. C., 1994. Mixing at Camarinal Sill in the Strait of Gibraltar. *J. Geophys. Res.* 99, 9847–9878.
- Willebrand, J., Barnier, B., Böning, C., Dieterich, C., Killworth, P. D., Provost, C. L., Jia, Y., Molines, J., New, A. L., 2001. Circulation characteristics in three eddy-permitting models of the North Atlantic. *Prog. Oceanogr.* 48, 123–161.
- Xu, X., Chang, Y. S., Peters, H., Özgökmen, T. M., Chassignet, E. P., 2006. Parameterization of gravity current entrainment for ocean circulation models using a high-order 3D nonhydrostatic spectral element model. *Ocean Modelling* 14, 19–44.
- Zenk, W., 1970. On the temperature and salinity structure of the Mediterranean Water in the North Atlantic. *Deep Sea Res.* 17, 627–631.
- Zenk, W., 1975. On the Mediterranean Outflow west of Gibraltar. *Meteor Forschungs Ergebnisse A* 16, 23–34.
- Zenk, W., Armi, L., 1990. The complex spreading pattern of Mediterranean water off the Portuguese slope. *Deep Sea Res.* 37, 1805–2392.

VITA

Xiaobiao Xu was born in Wuyi, Zhejiang province of P. R. China on September 6, 1976. His parents are Shenan Xu and Shenghua Li. He received his early educations at the Guzhu elementary school, the Lingxiatang middle school, and the First high school of Wuyi. In September, 1994, he entered the Marine Environment College of the Ocean University of Qingdao, from which he received his B.S degree in July 1998. In the same year, he started his graduate study in the First Institute of Oceanography, also located in Qingdao, and he received a M.S degree in Physical Oceanography in July, 2001.

In August 2001 Xu was admitted to the Graduate School of the University of Miami, and he was granted a Ph.D in Meteorology and Physical oceanography in December 2006.

Permanent Address: 1 Xianxialing Road, Qingdao, Shandong, P. R. China, 266061